DIPLOMA THESIS

Calculation of Injector Characteristics Using A Commercial CFD Code

written at
The Institute of Thermal Turbomachines and Powerplants
Vienna University of Technology

under direction of
O.Univ.Prof. Dipl.-Ing. Dr.techn. H. HASELBACHER
and
Univ.Ass. Dipl.-Ing. F. WINGELHOFER

by
María RODRÍGUEZ FERNÁNDEZ
Nußdorferstraße 45/11
A-1090 Vienna

Vienna, 18th September 2001

Abstract

The main topic of this work is the calculation of injector characteristics with CFD codes.

For the calculation with CFD codes it is necessary to build up models. In this work two-dimensional models are used. The geometry of the two-dimensional injector is fixed by the basis given by *Schlag* [2]. *Schlag* divides the injector into three parts: nozzle, mixing duct and diffuser. The pressure drop or rise in each part is modelled appropriately by fluid dynamic equations. For fixed operation conditions, as the net pressure rise and the jet properties, all possible injector geometries are calculated. One of these geometries, the smallest one, is chosen for further investigations. The characteristic of this possible injector is calculated with the method proposed by *Schlag* and then by applying a commercial CFD code.

Modelling the geometry, two different wall shapes are investigated. One of them represents a constant diameter injector with a constant mixing duct height. The other one is an approximation of a constant pressure injector. A circle being tangent to the diffuser and keeping the same heights at the entrance of the nozzle and at the entrance of the mixing duct as those of the constant diameter injector is used. In both cases, the wall of the diffuser is a straight line.

As shown by *Hembold et al.* [9], the efficiency of the constant pressure injector is higher than that of the constant diameter injector.

The characteristics and the flow fields of both injector types are shown, discussed and compared.

Contents

Nomenclature

Latin characters

Symbol	Unit	Description
A	$[m^2]$	Area.
AR	[-]	Area ratio.
a	[-]	Width ratio.
$a_1, ..., a_m$	[-]	Essential dimensions.
B	[-]	Constant in the equation for the logaritmic wall law.
CS	$[m^2]$	Control Surface.
CV	$[m^3]$	Control Volume.
C_p	[-]	Static pressure recovery.
C_{p_i}	[-]	Ideal pressure recovery.
c	$[\frac{m}{s}]$	Speed of sound.
c_1, c_2	[-]	Constants in the transport equations of the $k - \varepsilon$ model.
c_μ	[-]	Proportionality constant.
c_p	$[\frac{J}{kg\,K}]$	Specific heat capacity at constant pressure.
$\overline{\overline{D}}$	[-]	Strain rate tensor.
d_H	[m]	Hydraulic diameter.
E	[J]	Energy.
Eu	[-]	*Euler* number.
e	[J]	Exergy.
F		Extensive property.
$\vec{F_S}$	[N]	Surface forces, shear forces.
$\vec{F_V}$	[N]	Volumetric forces.
$\vec{f_m}$	$[\frac{N}{kg}]$	Volumetric forces per mass unit.
g_i	$[\frac{m}{s^2}]$	Acceleration due to gravity.
H	[J]	Total enthalpy.
h	[m]	Separation between walls.
$\overline{\overline{I}}$	[-]	Identity tensor.
K	[-]	*Von Karman* constant.
k	$[\frac{m^2}{s^2}]$	Turbulent kinetic energy.
k_1, k_2	[-]	Proportionality factors.
L	[m]	Length.
$\underline{l}$	[m]	*Prandtl* mixing length.
M	[N m]	Total momentum.
Ma	[-]	*Mach* number.
m	[kg]	Mass.

$\overline{m}$	[-]	Dimensionless parameter for the time period T calculation.
$P_1, ..., P_n$	[-]	Physical quantities.
p	[Pa]	Pressure.
$\dot{Q}$	$[\frac{J}{s}]$	Heat flux.
Q_p	$[\frac{J}{m^3 s}]$	Heat flux due combustion or chemical reaction.
Q_r	$[\frac{J}{m^3 s}]$	Heat flux due to radiation.
Q	$[\frac{m^3}{m\,s}]$	Total discharge per unit width.
Q_1	$[\frac{m^3}{m\,s}]$	Discharge per unit width of the jet.
Q_2	$[\frac{m^3}{m\,s}]$	Discharge per unit width of the secondary flow.
q	$[\frac{J}{m^2 s}]$	Heat flux due to convection.
Re	[-]	Reynolds number.
T_o	[K]	Environmental temperature.
T_J^o	[K]	Total temperature of the jet.
T_v	[K]	Turbulent intensity.
t_J	[m]	Thickness of the jet pipe
$\overline{\overline{T}}$	$[\frac{kg}{m\,s^2}]$	Turbulent intensity tensor.
u	$[\frac{J}{kg}]$	Specific internal energy.
V_t	$[\frac{m}{s}]$	Turbulent velocity scale.
v	$[\frac{m}{s}]$	Velocity of the environment.
$\overline{v}_j$	$[\frac{m}{s}]$	Mean velocity.
$\overline{v}'_j$	$[\frac{m}{s}]$	Fluctuating velocity.
v_x^*	$[\frac{m}{s}]$	Shear stress velocity.
$\dot{W}$	$[\frac{J}{s}]$	Power.
W	[m]	Width.
y	[m]	Distance to the wall.
y^+	[-]	Dimensionless wall distance.

Greek characters

Symbol	Unit	Description
α_{ij}	[-]	Exponents of the essential dimensions.
χ	[-]	Specific heat ratio.
ρ	$[\frac{kg}{m^3}]$	Density.
Δp	[Pa]	Pressure rise.
ε	$[\frac{m^2}{s^3}]$	Turbulent disipation.
ϕ		Amount of F per mass unit.
λ_G	[-]	Roughness coefficient.
μ	[-]	Load coefficient.
μ_l	$[\frac{kg\,m}{s^2}]$	Dynamic viscosity.
μ_v	$[\frac{kg\,m}{s^2}]$	Proportionality factor.
μ_t	$[\frac{kg\,m}{s^2}]$	Dynamic turbulent viscosity.
ν_t	$[\frac{m^2}{s^2}]$	Kinetic turbulent viscosity.
Π	[-]	Dimensionless parameter.
σ_ε	[-]	Constant in the transport equations of the $k - \varepsilon$ model.
σ_k	[-]	Constant in the transport equations of the $k - \varepsilon$ model.
$\overline{\overline{\tau}}$	$[\frac{N}{m}]$	Surface forces tensor.

$\overline{\overline{\tau}}^{*}$	$[\frac{N}{m}]$	Stress tensor.
Θ	$[°]$	Angle of the diffuser.
θ	$[°]$	Semi-angle of the diffuser.
τ_w	$[\frac{N}{m}]$	Shear stress at the wall.

Subindices

Symbol	Description
A	Entrance of the nozzle.
A_o	Total magnitudes for the jet at a plane in the jet nozzle.
B_o	Total magnitudes for the secondary flow at the entrance of the mixing duct.
C_o	Total magnitudes for the mixture at a plane at the end of the diffuser.
E	Secondary flow at the entrance of the mixing duct.
F	End of the diffuser.
G	Suctioned gases.
J	Jet nozzle.
M	End of the mixing duct.
$diff$	Diffuser.
mix	Mixing duct.
$nozz$	Nozzle.

Chapter 1

Introduction

An injector, also known as *jet-ejector* or *jet pump*, describes a device in which a pumping effect is achieved using a motive fluid. It requires no mechanical drive and has no moving parts. This general sentence can be applied to every injector independently of the model or range of application.

The jet is the motive fluid and serves to create vacuum. The function will depend greatly on the design of the nozzle, the mixing duct and the diffuser, elements which the fluid pass through.

The flow section will change along the path. The pressure in the nozzle decreases and the velocity rises. Conversely the flow is retarded in the diffuser while its pressure increases to the discharge pressure at the outlet of the injector.

The beginning of the mixing duct has the lowest static pressure. At this point the suction flow coming from the environment enters into the mixing duct and is mixed with the motive fluid flowing with very high velocity. Part of the kinetic energy is transferred to the suction flow. Motive flow and suction flow pass together as a mixture through the diffuser, loosing velocity and gaining pressure.

In an injector, the static pressure energy of the motive flow which cannot be directly transferred is thus converted into kinetic energy. This kinetic energy can be released to the suction flow by momentum transfer while both flows mingle. The diffuser converts the kinetic energy of the mixture consisting in motive flow and suction flow back into static pressure energy.

1.1 Applications and Classification

The injectors are used to create vacuum, to compress gases, to convey liquids, to transport granular solids and to mix liquids or gases.

The motive fluid may be

- steam at pressure above atmosphere
- atmospheric steam
- vacuum steam
- compressed gas or air

1

- atmospheric air

- water and other available liquids.

The following table summarizes the terms of the injectors laid down according to the DIN standards 24290. When defining certain types of injectors, the standard terms for motive fluid and material delivered (gas, steam, liquid, solids) can be replaced by specific ones.

Suction medium		Motive medium Gas	Motive medium Steam	Motive medium Liquid
Gas	ventilator	Gas ventilator	Steam ventilator	Liquid ventilator
	compressor	Gas compressor	Steam compressor	Liquid compressor
	vacuum	Gas vacuum ejector	Steam vacuum ejector	Liquid ejector
Liquid		Gas liquid ejector	Steam liquid ejector	Liquid vacuum ejector
Solids		Gas solids ejector	Steam solids ejector	Liquid solids

Depending on both fluids, the following applications can be described:

- Steam, gas and water jet injectors are used for creating vacuum, conveying compressing and mixing of gases, liquids and solids.

- Steam jets and water ventilators are used in waste gas mixing nozzles.

- Steam jets are used as steam jet heaters.

- Water jet liquid, vacuum and solid injectors are used as gravelpumps.

- Evaporating units.

- Steam jet cooling systems are used for water cooling by partial evaporation.

- Surface condensers and direct contact condensers are used in process plants and steam turbines.

Chapter 2

Fluid Dynamics

2.1 Laminar Flow

When talking about fluids as a continuous environment, it should be beard in mind that there are four basic principles which have to be carried out. These are:

- **Mass conservation** which leads to the continuity equation.

- **The second law of Newton** which leads to the constant momentum equation.

- **The first principle of the thermodynamics** which leads to the constant energy equation.

- **The second principle of the thermodynamics**.

Apart from these main principles there are also secondary principles derivated from them, like the constant mechanic energy, which must be also obeyed.

All the equations can be expressed either in their integral (built-in) formulation when they are referred to a volume or in their differential formulation when the volume they are referred to tends to a point. In order to understand what this volume is like when this volume tends to a point there are some helpful definitions.

The principle listed above have the following ways of application:

1. All the activities of all and every one of the masses must be so that they obey the main and the secondary relevant principles.

2. All the activities of all and every one of the volumes must be so that they obey the main and the secondary relevant principles.

In the first case, the principles are applied to an amount of mass called *system*. A system can change shape, position and thermal condition, but it must have always the same amount of mass. For instance an element is treated like a system when it keeps the same mass although it changes its shape and volume, like in a closed piston.

The second way takes a spatially fixed and determined volume called *control volume*. The amount and the identity of the materia (mass) in the control volume can change along time, but the shape keeps constant. For instance a nozzle would be treated as a control volume.

2.1.1 *Reynolds* Transport Theorem

When the equations mentioned above are assigned to any body and it is desired to have them in terms of system or control volume, the *Reynolds* transport theorem will be applied.

For a given extensive property F (a property which depends on the amount of the substance), the *Reynolds* transport theorem tells that the temporary variation of this extensive property F in a system is equal to the substantial variation of F,

$$\left.\frac{dF}{dt}\right|_{system} = \frac{DF}{Dt}. \tag{2.1}$$

This gives two answers:

- How to pass from a system to a control volume.

- How to pass from the view of *Lagrange* to the view of *Euler*.

Calculation of the Substantial Variation

The substantial variation of the property F is calculated with the derivative of this property. The definition of derivative is given by
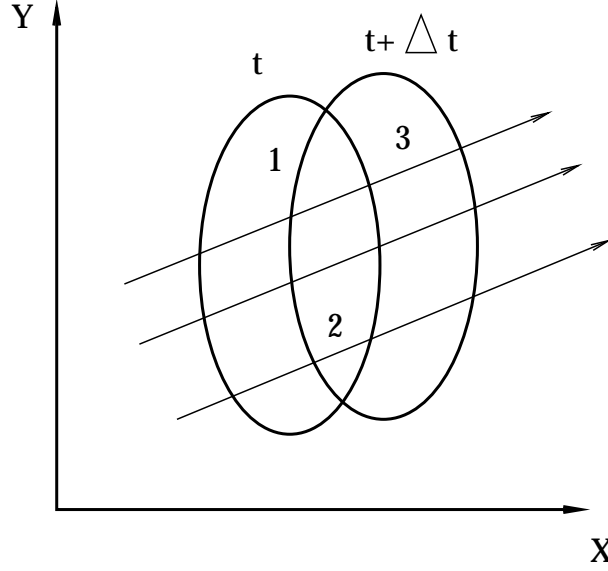
$$\frac{dF}{dt} = \lim_{\Delta t \to 0} \frac{F|_{t+\Delta t} - F|_t}{\Delta t}. \tag{2.2}$$

A control volume must be fixed first. The control volume will be coincident with the system at the instant t

$$F|_t = F_{CV}|_t \tag{2.3}$$

and for the instant $t + \Delta t$ it will be like in figure 2.10

$$F|_{t+\Delta t} = (F_{CV} - F_1 + F_3)|_{t+\Delta t}. \tag{2.4}$$

Figure 2.1: *Reynolds* transport theorem

Calling ϕ the distribution per mass unit of the property F, F can be expressed as

$$F = \int_m \phi \, dm = \int_V \phi \rho \, dV.$$ (2.5)

Introducing equation 2.3, 2.4 and 2.5 in equation 2.2 the derivative becomes

$$\frac{dF}{dt} = \lim_{\Delta t \to 0} \frac{\int_{CV} \phi\rho \, dV|_{t+\Delta t} - \int_{V1} \phi\rho \, dV|_{t+\Delta t} + \int_{V3} \phi\rho \, dV|_{t+\Delta t} - \int_{CV} \phi\rho \, dV|_t}{\Delta t}.$$ (2.6)

Designating $\vec{dA}$ as area vector, $\vec{dl}$ as stream line direction vector and solving the whole limit by parts, it is obtained

$$\lim_{\Delta t \to 0} \frac{\int_{V1} \phi\rho \, dV|_{t+\Delta t}}{\Delta t} = \lim_{\Delta t \to 0} \frac{\int_1 \rho\phi \, dA \, dl \cos\theta}{\Delta t} = \int_{S1} \rho\phi \left(\vec{v}\vec{n}\right) \, dA,$$ (2.7)

$$\lim_{\Delta t \to 0} \frac{\int_{V3} \phi\rho \, dV|_{t+\Delta t}}{\Delta t} = \lim_{\Delta t \to 0} \frac{\int_3 \rho\phi \, dA \, dl \cos\theta}{\Delta t} = \int_{S3} \rho\phi \left(\vec{v}\vec{n}\right) \, dA,$$ (2.8)

$$\lim_{\Delta t \to 0} \frac{\int_{CV} \phi\rho \, dV|_{t+\Delta t} - \int_{CV} \phi\rho \, dV|_t}{\Delta t} = \frac{\partial \int_{CV} \rho\phi \, dV}{\partial t}.$$ (2.9)

With equation 2.7, 2.8 and 2.9 the derivative becomes

$$\left.\frac{dF}{dt}\right|_{system} = \frac{\partial}{\partial t} \int_{CV} \rho\phi \, dV + \int_{CS} \rho\phi \left(\vec{v}\vec{n}\right) \, dA = \frac{DF}{Dt}.$$ (2.10)

In equation 2.10 ρdV is a mass element contained in the control volume, $\int_{CV} \rho\phi \, dV$ is the total amount of the property F contained in the control volume and $\int_{CS} \rho\phi \left(\vec{v}\vec{n}\right) \, dA$ is the flow of the property F through the area dA.

Remarks

- The velocity $\vec{v}$ is measured with regard to the surface of the control volume.

- The change along the time of the property F inside the control volume must be evaluated by a fixed observer inside the control volume.

2.1.2 Mass Conservation Equation or Continuity Equation

If the extensive property F is equal to the mass m,

$$m = \int_m \phi \, dm, \tag{2.11}$$

the value of ϕ must be

$$\phi = 1. \tag{2.12}$$

Applying the definition of a *system*

$$\left. \frac{dm}{dt} \right|_{system} = 0 \tag{2.13}$$

to equation 2.10, it is obtained

$$\left. \frac{dm}{dt} \right|_{system} = \frac{\partial}{\partial t} \int_{CV} \rho \, dV + \int_{CS} \rho \left(\vec{v}\vec{n} \right) \, dA = 0, \tag{2.14}$$

which is known as the **Mass Conservation Equation**.

In case of air, it is more interesting to study the fluid in a point. To do so, the differential form of the equation is used. To obtain the differential form of the equation it is necessary to apply the *Gauss* theorem

$$\oint_A \vec{\phi} \, \vec{n} \, dA = \int_V \nabla \phi \, dV \tag{2.15}$$

to equation 2.14, obtaining then

$$\frac{\partial}{\partial t} \int_{CV} \rho \, dV + \int_{CV} \nabla \left(\rho \vec{v} \right) \, dV = 0. \tag{2.16}$$

Changing the order of derivative and integration in the first term of equation 2.16 the integrand can be transformed to

$$\frac{\partial}{\partial t} \rho dV = \frac{\partial \rho}{\partial t} dV + \frac{\partial \left(dV \right)}{\partial t} \rho. \tag{2.17}$$

As the control volume does not change in time by definition, the second term on the right hand side of equation 2.17 is

$$\frac{\partial \left(dV \right)}{\partial t} \rho = 0. \tag{2.18}$$

Introducing equation 2.17 and 2.18 in equation 2.16, equation 2.16 becomes

$$\int_{CV} \left[\frac{\partial}{\partial t} \rho + \nabla \left(\rho \vec{v} \right) \right] dV = 0. \tag{2.19}$$

Because equation 2.19 is valid for any control volume, it is also valid for any stream line:

$$\frac{\partial}{\partial t} \rho + \nabla \left(\rho \vec{v} \right) = 0. \tag{2.20}$$

Using subscripts notation, equation 2.20 can be written as

$$\frac{\partial}{\partial t} \rho + \frac{\partial}{\partial x_j} \left(\rho \, v_j \right) = 0. \tag{2.21}$$

If the total derivative is defined as

$$\frac{D}{Dt} = \frac{\partial}{\partial t} + \vec{v} \nabla, \tag{2.22}$$

equation 2.20 can be written as

$$\frac{D\rho}{Dt} + \rho \nabla \vec{v} = 0. \tag{2.23}$$

2.1.3 Constant Momentum Equations

The second law of *Newton* says that

$$\vec{a} \, dm = d\vec{F}_V + d\vec{F}_S, \tag{2.24}$$

where dF_V are volumetric forces and dF_S are surface forces applied on the element dm.

On the basis of velocity equation 2.24 can be written as

$$\frac{d\vec{v}}{dt} dm = d\vec{F}_V + d\vec{F}_S. \tag{2.25}$$

The term dm can be expressed as

$$dm = \rho \, dV, \tag{2.26}$$

the volumetric forces applied on any element of mass can be defined as

$$d\vec{F}_V = \vec{f_m} \, dm = \rho \, \vec{f_m} \, dV \tag{2.27}$$

and the surface forces applied on the surface of that element can be written as

$$d\vec{F}_S = \overline{\overline{\tau}}\vec{n}\,dS, \tag{2.28}$$

where the tensor $\overline{\overline{\tau}}$ expresses all the forces that appear on the surfaces of the fluid element. The tensor can be split up in

$$\overline{\overline{\tau}} = \left(-p + \left(\mu_v - \frac{2}{3}\right)\mu_l \nabla \vec{v}\right)\overline{\overline{I}} + 2\mu_l \overline{\overline{D}} \tag{2.29}$$

where p is the pressure working on the element, μ_l is the viscosity of the fluid, μ_v is a proportionality factor, $\overline{\overline{I}}$ is the identity tensor and $\overline{\overline{D}}$ is the strain rate tensor. Defining each one of these elements, the identity tensor is

$$\overline{\overline{I}} = \begin{bmatrix} 1 & 0 & 0 \\ 0 & 1 & 0 \\ 0 & 0 & 1 \end{bmatrix}, \tag{2.30}$$

the proportionality factor is

$$\mu_v = \frac{\tau_{11} + \tau_{22} + \tau_{33} + 3\,p}{\nabla \vec{v}}, \tag{2.31}$$

and the strain rate tensor is

$$\overline{\overline{D}} = \begin{bmatrix} \frac{\partial v_x}{\partial x} & \frac{1}{2}\left(\frac{\partial v_x}{\partial y} + \frac{\partial v_y}{\partial x}\right) & \frac{1}{2}\left(\frac{\partial v_x}{\partial z} + \frac{\partial v_z}{\partial x}\right) \\ \frac{1}{2}\left(\frac{\partial v_x}{\partial y} + \frac{\partial v_y}{\partial x}\right) & \frac{\partial v_y}{\partial y} & \frac{1}{2}\left(\frac{\partial v_y}{\partial z} + \frac{\partial v_z}{\partial y}\right) \\ \frac{1}{2}\left(\frac{\partial v_x}{\partial z} + \frac{\partial v_z}{\partial x}\right) & \frac{1}{2}\left(\frac{\partial v_y}{\partial z} + \frac{\partial v_z}{\partial y}\right) & \frac{\partial v_z}{\partial z} \end{bmatrix}. \tag{2.32}$$

Once each of the force elements that are involved in the equation 2.24 has been defined, equation 2.24 can be integrated over any volume

$$\int_V \rho \frac{d\vec{v}}{dt}\,dV = \int_V \rho \vec{f}_m\,dV + \int_S \left(\overline{\overline{\tau}}\vec{n}\right)\,dS. \tag{2.33}$$

If the distribution per mass unit ϕ is set to v the property F becomes

$$F = \int_V \rho \vec{v}\,dV = \int_V \vec{v}\,dm. \tag{2.34}$$

The left hand side of equation 2.33 can be expressed as

$$\left.\frac{dF}{dt}\right|_{system} = \frac{d}{dt}\int_V \vec{v}\,dm = \int_V dm\frac{d\vec{v}}{dt} = \int_V \rho\frac{d\vec{v}}{dt}dV = \int_V \rho\vec{f}_m\,dV + \int_S \left(\overline{\overline{\tau}}\,\vec{n}\right)\,dS. \tag{2.35}$$

Applying the *Reynolds* transport theorem to equation 2.35 the **Constant Momentum Equations** are obtained finally

$$\left.\frac{dF}{dt}\right|_{system} = \frac{\partial F_V}{\partial t} + \int_S \rho\vec{v}\left(\vec{v}\,\vec{n}\right)\,dS = \int_{CV} \rho\vec{f}_m\,dV + \int_{CS} \left(\overline{\overline{\tau}}\,\vec{n}\right)\,dS \Rightarrow$$

$$\frac{\partial}{\partial t}\int_{CV} \rho\vec{v}\,dV + \int_{CS} \rho\vec{v}\left(\vec{v}\,\vec{n}\right)\,dS = \int_{CV} \rho\vec{f}_m\,dV + \int_{CS} \left(\overline{\overline{\tau}}\,\vec{n}\right)\,dS \tag{2.36}$$

where

- $\frac{\partial}{\partial t} \int_{CV} \rho \vec{v} \, dV$ is the temporary variation of the momentum inside the control volume,

- $\int_{CS} \rho \vec{v} \, (\vec{v} \, \vec{n}) \, dS$ is the convective transport through the control surface,

- $\int_{CV} \rho \vec{f_m} \, dV$ is referred to the mass forces in the control volume and

- $\int_{CS} (\overline{\overline{\tau}} \, \vec{n}) \, dS$ is referred to the surface forces on the control volume.

If the differential formulation is of interest, again the *Gauss* theorem, equation 2.15, is applied to the surface terms like

$$\int_{CS} \rho \vec{v} \, (\vec{v} \, \vec{n}) \, dS = \int_{CV} \nabla \rho \vec{v} \, \vec{v} \, dV \tag{2.37}$$

and

$$\int_{CS} (\overline{\overline{\tau}} \, \vec{n}) \, dS = \int_{CV} \nabla \overline{\overline{\tau}} \, dV, \tag{2.38}$$

resulting then in the differential formulation for the **Constant Momentum Equations**

$$\frac{\partial}{\partial t} \rho \vec{v} + \nabla \rho \vec{v} \, \vec{v} = \rho \vec{f_m} + \nabla \overline{\overline{\tau}}. \tag{2.39}$$

2.1.4   Equations of *Navier-Stokes*

Equation 2.39 can also be written with suscripts

$$\frac{\partial}{\partial t} \rho v_i + \frac{\partial \, (\rho v_i) \, v_j}{\partial x_j} = \rho f_{m_i} + \frac{\partial \tau_{j,i}}{\partial x_j}. \tag{2.40}$$

Inserting equation 2.29 in equation 2.40, the *Navier-Stokes* equations for a laminar flow are obtained

$$\frac{\partial}{\partial t} \rho v_i + \frac{\partial}{\partial x_j} \, (\rho v_i) \, v_j = \rho f_{m_i} - \frac{\partial p}{\partial x_i} - \frac{2}{3} \mu_l \frac{\partial}{\partial x_i} \left(\frac{\partial v_j}{\partial x_j} \right) + \mu_l \frac{\partial}{\partial x_j} \left(\frac{\partial v_i}{\partial x_j} + \frac{\partial v_j}{\partial x_i} \right). \tag{2.41}$$

In equation 2.41 the *Stokes* hypothesis

$$\frac{2}{3} \mu_l - \mu_v = 0$$

and the assumption of constant viscosity μ_l are used.

2.1.5   Constant Energy Equation

According to the first principal of thermodynamics changes of the energy dE are done by the work of external forces $\dot{W} \, dt$ and by the heat supply $\dot{Q} \, dt$:

$$\frac{dE}{dt} = \dot{W} + \dot{Q}. \tag{2.42}$$

The variation of the energy E can be expressed by

$$\frac{dE}{dt} = \frac{d}{dt} \int_V \rho \left(u + \frac{1}{2} v^2 \right) dV, \tag{2.43}$$

where u is the internal specific energy of the fluid and v the velocity of the fluid.

The external forces $\dot{W}$ operating on the fluid volume are

$$\dot{W} = \vec{F} \vec{v} = \int_V \rho \vec{f_m} \vec{v} \, dV + \int_S \left(\overline{\overline{\tau}} \, \vec{n} \right) \vec{v} \, dS, \tag{2.44}$$

and the heat flux $\dot{Q}$ is equal to

$$\dot{Q} = \int_S \vec{q} \, \vec{n} \, dS + \int_V \left(Q_p + Q_r \right) dV, \tag{2.45}$$

where $- \int_S \vec{q} \, \vec{n} \, dS$ is the heat flux by conduction through the surfaces of the fluid volume and $\int_V \left(Q_p + Q_r \right) dV$ is the heat flux originated in combustion, chemical reaction or in radiation.

Inserting equations 2.43, 2.44 and 2.45 equation 2.42 becomes

$$\frac{d}{dt} \int_V \rho \left(u + \frac{1}{2} v^2 \right) dV \bigg|_{system} = \int_V \rho \vec{f_m} \vec{v} \, dV + \int_S \left(\overline{\overline{\tau}} \, \vec{n} \right) \vec{v} \, dS + \dot{Q}. \tag{2.46}$$

Applying the *Reynolds* transport theorem 2.10 the integral expression for the **Constant Energy Equation** is obtained.

$$\frac{\partial}{\partial t} \int_{CV} \rho \left(u + \frac{1}{2} v^2 \right) dV + \int_{CS} \rho \left(u + \frac{1}{2} v^2 \right) (\vec{v} \vec{n}) \, dS =$$

$$\int_{CV} \rho \vec{f_m} \vec{v} \, dV + \int_{CS} \left(\overline{\overline{\tau}} \, \vec{n} \right) \vec{v} \, dS - \int_{CS} \vec{q} \, \vec{n} \, dS + \int_{CV} \left(Q_p + Q_r \right) dV. \tag{2.47}$$

Defining the total enthalpy H as

$$H = u + \frac{1}{2} v^2 + \frac{p}{\rho}, \tag{2.48}$$

equation 2.47 can be written as

$$\frac{\partial}{\partial t} \int_{CV} \rho H \, dV + \int_{CS} \rho H \left(\vec{v} \, \vec{n} \right) dS =$$

$$\int_{CV} \frac{\partial p}{\partial t} \, dV + \int_{CV} \rho \vec{f_m} \vec{v} \, dV + \int_{CS} \left(\overline{\overline{\tau^*}} \, \vec{n} \right) \vec{v} \, dS - \int_{CS} \vec{q} \, \vec{n} \, dS + \int_{CV} \left(Q_p + Q_r \right) dV, \tag{2.49}$$

where

$$\overline{\overline{\tau^*}} = \overline{\overline{\tau}} + p \overline{\overline{I}} \tag{2.50}$$

is the stress tensor and $\overline{\overline{I}}$ the identity tensor.

The differential form is obtained applying *Gauss* theorem on equation 2.49

$$\frac{\partial}{\partial t} \left(\rho H \right) + \frac{\partial}{\partial x_j} \left(\rho \, v_j \, H \right) = \frac{\partial p}{\partial t} + \rho \, f_i \, v_i - \frac{\partial}{\partial x_j} \left(v_i \, \tau_{i,j}^* \right) - \frac{\partial q_j}{\partial x_j} + Q_p + Q_r \tag{2.51}$$

or in symbolic notation

$$\frac{\partial}{\partial t} \left(\rho H \right) + \nabla \left(\rho H \vec{v} \right) = \frac{\partial p}{\partial t} + \rho \vec{f_m} \vec{v} + \nabla \left(\overline{\overline{\tau^*}} \, \vec{v} \right) - \nabla \vec{q} + Q_p + Q_r. \tag{2.52}$$

2.2   Turbulent Flow

Having a fluid running with a high enough *Reynolds* number makes the movement of this fluid very sensitive to any disturbance and makes also these disturbances get amplified very fast. The flow becomes very irregular taking an uncertain character. Such a flow is called a *turbulent flow* which is featured by very high both spatial and temporary fluctuations of the physical quantities.

For *permanent turbulent flows*, whose mean physical quantities do not change in time, the instantaneaous quantity ϕ can be split in a mean part $\overline{\phi}$ and a fluctuating one ϕ':

$$\phi(x, y, z, t) = \overline{\phi}(x, y, z) + \phi'(x, y, z, t).$$

2.2.1   *Reynolds* **Averaged** *Navier-Stokes* **Equations**

When these splitted turbulent quantities are introduced in the differential form of the constant momentum equations, equation 2.39, or what is the same, in the *Navier-Stokes* equations 2.41 an additional term $\nabla \overline{\overline{T}}$ appears.

The tensor $\overline{\overline{T}}$ is known as *Reynolds stress tensor* and is defined by

$$\overline{\overline{T}} = \begin{bmatrix} -\rho \overline{v_x'^2} & -\rho \overline{v_x' v_y'} & -\rho \overline{v_x' v_z'} \\ -\rho \overline{v_y' v_x'} & -\rho \overline{v_y'^2} & -\rho \overline{v_y' v_z'} \\ -\rho \overline{v_z' v_x'} & -\rho \overline{v_z' v_y'} & -\rho \overline{v_z'^2} \end{bmatrix} \tag{2.53}$$

The *Reynolds* averaged *Navier-Stokes* equation for the mean flow have the following form for an incompressible fluid:

$$\frac{\partial}{\partial t} \rho \overline{v}_i + \frac{\partial}{\partial x_j} \left(\rho \overline{v}_i \right) \overline{v}_j =$$

$$= \rho f_{m_i} - \frac{\partial p}{\partial x_i} - \frac{2}{3} \mu_l \frac{\partial}{\partial x_i} \left(\frac{\partial \overline{v}_j}{\partial x_j} \right) + \mu \frac{\partial}{\partial x_j} \left(\frac{\partial \overline{v}_i}{\partial x_j} + \frac{\partial \overline{v}_j}{\partial x_i} \right) - \rho \frac{\partial}{\partial x_j} \overline{v_i' v_j'}. \tag{2.54}$$

The *Reynolds* stress tensor $\overline{\overline{T}}$ is normally 100 to 1000 times bigger than the laminar shear stress tensor $\overline{\overline{\tau}}$ in free flow.

2.2.2   **Mixing Length Theory by** *Prandtl*

The mixing length theory tries to give an analytical expression for the *Reynolds* stress tensor. For a fluid in two-dimensional and permanent turbulent flow *Boussinesq* established the hypothesis that the *Reynolds* stresses can be expressed in analogy to the laminar shear stresses,

$$T_{x,y} = \mu_t \frac{\partial \overline{v}_x}{\partial y} \tag{2.55}$$

where μ_t was defined as the dynamic turbulent viscosity which is equal to

$$\mu_t = \rho \nu_t. \tag{2.56}$$

ν_t is the kinematic turbulent viscosity or eddy viscosity which depends on the local, normally unknown conditions of the flow. *Prandtl* was able to substitute the turbulent kinetic viscosity by a magnitude that he called mixing length.

Observing only the mean flow, the velocity of a particle depends on the coordinates, but not on the time:

$$\Delta \overline{v}_{x_1} = \overline{v}_x(y + l) - \overline{v}_x(y),$$

$$\Delta \overline{v}_{x_2} = \overline{v}_x(y) - \overline{v}_x(y - l).$$

Developing the expressions for $\Delta \overline{v}_{x_1}$

$$\Delta \overline{v}_{x_1} = \left[\overline{v}_x(y) + \left. \frac{d\overline{v}_x}{dy} \right|_y dy \right] - \overline{v}_x(y) \tag{2.57}$$

and for $\Delta \overline{v}_{x_2}$

$$\Delta \overline{v}_{x_2} = \overline{v}_x(y) - \left[\overline{v}_x(y) - \left. \frac{d\overline{v}_x}{dy} \right|_y dy \right] \tag{2.58}$$

the difference in velocity $\Delta \overline{v}_{x_1}$ and $\Delta \overline{v}_{x_2}$ can be espressed by

$$\Delta \overline{v}_{x_1} = l \left. \frac{d\overline{v}_x}{dy} \right|_y \tag{2.59}$$

and

$$\Delta \overline{v}_{x_2} = l \left. \frac{d\overline{v}_x}{dy} \right|_y . \tag{2.60}$$

The velocity fluctuation is assumed as the average value of these deviations, expressed as

$$\left| \overline{v}'_x \right| = \overline{|v'_x|} = \frac{1}{2} (|\Delta \overline{v}_{x_1}| + |\Delta \overline{v}_{x_2}|) = l \left| \left. \frac{d\overline{v}_x}{dy} \right|_y \right| . \tag{2.61}$$

In this two-dimensional sample the main velocity in the cross direction is approximately zero $\overline{v}_y \approx 0$ and the fluctuations in both directions are set to be proportional

$$\left| \overline{v}'_x \right| \propto \left| \overline{v}'_y \right| = k_1 \left| \overline{v}'_x \right| = k_1 \, l \left| \left. \frac{d\overline{v}_x}{dy} \right|_y \right| . \tag{2.62}$$

The *Reynolds* stresses $T_{x,y}$ can be espressed by

$$T_{x,y} = -\rho \overline{v'_x v'_y} = -\rho \, k_2 \left| \overline{v'_x} \right| \left| \overline{v'_y} \right| = -\rho \, k_1 \, k_2 \, l^2 \left(\frac{d\overline{v}_x}{dy} \right)^2 =$$

$$= -\rho \, \underline{l}^2 \left(\frac{d\overline{v}_x}{dy} \right)^2 = -\rho \, \underline{l}^2 \left| \frac{dv_x}{dy} \right| \frac{d\overline{v}_x}{dy}. \tag{2.63}$$

Equation 2.63 is the statement of **Mixing Length Theory**, where $\underline{l}$ is the *Prandtl* mixing length.

With this theory the unknown turbulent viscosity μ_t has been replaced by the also unknown mixing length $\underline{l}$. This mixing length is undetermined in free turbulence anad has to be modelled appropriately.

2.2.3 $k - \varepsilon$ **Turbulence Model**

The $k - \varepsilon$ turbulence model uses the eddy viscosity assumption to relate the *Reynolds* stresses to the mean flow variables. This model was first derived for incompressible flows, in which density fluctuations can be ignored. Doing a *Favre* averaging on the *Navier-Stokes* equations the formally identical equations are obtained for the turbulent mean flow. Thus, in practice, this model is also used for compressible flows.

The turbulent viscosity μ_t is modelled as the product of a turbulent velocity scale V_t and a turbulent length scale $\underline{l}$ as proposed by *Prandtl-Kolmogorov*. Introducing a proportionality factor c_μ the turbulent viscosity μ_t can be expressed by

$$\mu_t = \rho c_\mu \underline{l} V_t. \tag{2.64}$$

In this model the turbulent velocity scale V_t is determined as

$$V_t = \sqrt{k} \tag{2.65}$$

where k is the turbulent kinetic energy, determined by the solution of a semi-empirical transport equation taken from the CFX manuals [1] as

$$\frac{\partial \rho k}{\partial t} + \frac{\partial}{\partial x_j} (\rho \, v_j \, k) - \frac{\partial}{\partial x_j} \left[\left(\mu_l + \frac{\mu_t}{\sigma_k} \right) \frac{\partial k}{\partial x_j} \right] = P - \rho \, \varepsilon. \tag{2.66}$$

σ_k is a constant with a value of $\sigma_k = 1.0$ and ε is the turbulent dissipation rate of k also given by a semi-empirical transport equation written as

$$\frac{\partial \rho \varepsilon}{\partial t} + \frac{\partial}{\partial x_j} (\rho \, v_j \, \varepsilon) - \frac{\partial}{\partial x_j} \left[\left(\mu_l + \frac{\mu_t}{\sigma_\varepsilon} \right) \frac{\partial \varepsilon}{\partial x_j} \right] = c_1 \, \frac{\varepsilon}{k} \, P - c_2 \, \rho \, \frac{\varepsilon^2}{k} \tag{2.67}$$

where $c_1 = 1,44$, $c_2 = 1,92$ and $\sigma_\varepsilon = 1,22$.

In both cases the shear production P is

$$P = (\mu_l + \mu_t) \frac{\partial v_j}{\partial x_j} \left(\frac{\partial v_i}{\partial x_j} + \frac{\partial v_j}{\partial x_i} \right) - \frac{2}{3} \frac{\partial v_j}{x_j} \left[(\mu_l + \mu_t) \frac{\partial v_j}{\partial x_j} + \rho \, k \right]. \tag{2.68}$$

In the $k - \varepsilon$ model the length scale is assumed as a dissipation length scale. For isotropic turbulent dissipation scales *Kolmogorov* determined

$$\underline{l} = \frac{k^{\frac{2}{3}}}{\varepsilon}. \tag{2.69}$$

Inserting equation 2.65 and 2.69 in equation 2.64, the eddy viscosity μ_t is calculated by

$$\mu_t = \rho c_\mu \frac{k^2}{\varepsilon}, \tag{2.70}$$

where the proportionality factor c_μ takes the value of $c_\mu = 0,09$.

2.2.4 Universal Formulation of the Velocity Distribution in the Vicinity of a Wall.

In a free turbulent flow the turbulent stresses are in general much larger than the viscosity stresses. Close to a wall this is not valid. In this region the viscosity stresses have nearly the same magnitude as the turbulent stresses.

When moving in a region very close to a wall, $y \to 0$, with y the distance from the wall, the shape of the duct will not be relevant for the calculations.

The parameters which have influence on the character of the flow are ρ, μ_l, τ_w, and y. The width of the wall h does not appear as it does not have influence on the local flow. Using dimensionless analysis the velocity v_x depends on

$$v_x = f\left(\rho, \mu, \tau_w, y\right)$$

where τ_w is the shear stress at the wall.

Applying the Π-theorem, two dimensionless parameters are obtained,

$$\Pi_1 = \frac{v_x}{v_x^*}$$

and

$$\Pi_2 = \frac{\rho\, y\, v_x^*}{\mu_l}$$

where

$$v_x^* = \sqrt{\frac{\tau_w}{\rho}} \tag{2.71}$$

is known as the shear stress velocity and Π_2 is normally called dimensionless wall distance y^+.

With both dimensionless parameters the distribution of the velocities in the wall region can be expressed by

$$\frac{v_x}{v_x^*} = f\left(\frac{\rho\, y\, v_x^*}{\mu_l}\right) = f(y^+). \tag{2.72}$$

Equation 2.72 is often called **Universal Wall Law**.
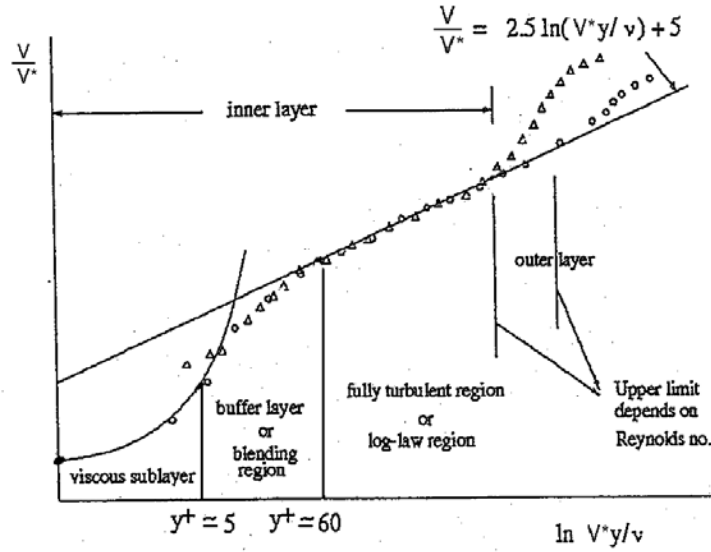
Figure 2.2: Universal Wall Law [13].

In the viscous sublayer (figure 2.2) where the viscosity predominates the value of the shear stress at the wall can be calculated by the viscosity stress

$$\tau_w = \tau_{x,y} = \mu_l \frac{\partial v_x}{\partial y}. \tag{2.73}$$

A linear function for the velocity distribution is obtained

$$\frac{v_x}{v_x^*} = \frac{\rho \, y \, v_x^*}{\mu_l} = y^+ \tag{2.74}$$

also called *Prandtl's wall law*.

In the fully turbulent region (figure 2.2) the shear stress can be approximated by the turbulent stress

$$\tau_w = \tau_{x,y} = -\rho \overline{v_x' \, v_y'}. \tag{2.75}$$

Using the *Bousinesq* approximation

$$\tau_w = -\rho \, \underline{l}^2 \left(\frac{dv_x}{dy} \right)^2, \tag{2.76}$$

with $\underline{l} = f(y, \rho, \tau_w)$ and applying the Π-theorem, the mixing length $\underline{l}$ can be expressed by

$$\underline{l} = K \, y \tag{2.77}$$

with a universal constant K called *Von Karman* constant.

A logarithmic distribution for the velocity distribution

$$\frac{v_x}{v_x^*} = 2,5 \, ln \frac{\rho \, y \, v_x^*}{\mu} + B \tag{2.78}$$

15

is obtained which is also known as the *logarithmic wall law*.

The value of B has been obtained experimentally and is equal to 5 for a smooth wall.

For the buffer layer there is not any theoretical expression for the velocity distribution, it is an undetermined region.

2.3 Dimensional Analysis

The application of the Π-theorem has been mentioned before. This theorem, also called *Buckingham´s* theorem, gives the answer to the question of how many dimensionless parameters can be formed with the physical quantities involved in a problem and how to obtain these parameters.

A group of physical quantities is a dimensionless parameter when the multiplication of the dimensions of those physical quantities gives the unit as a result. With this definition it is provided that the introduction of dimensional homogeneity is also valid for the dimensionless parameters. The dimensional homogeneity establishes that any equation derived analytically and representing a physical phenomenon must be satisfied in any dimensional system.

By the dimensional analysis, a phenomenon can be formulated as a relation between groups of dimensionless parameters. The main advantages of the dimensionless parameters are

- a considerable smaller number of experiments is required to establish a relation between physical quantities,

- simplification of the problem and

- the possibility of doing experiments on scaled models.

2.3.1   Π-Theorem

When in a physical problem a relation between n physical quantities P_1,P_2,...,P_n exists,

$$f(P_1, ..., P_n) = 0$$

these quantities P_1,P_2,...,P_n can be expressed on the basis of m essential dimensions, taking the following form

$$P_i = P_i \, a_1^{\alpha_{i1}} \, a_2^{\alpha_{i2}} ... a_m^{\alpha_{im}},$$

where a_1,a_2,..,a_m are the essential dimensions and α_{ij} are the exponents of those dimensions.

The Π-theorem proofs that the maximum number of dimensionless parameters that can be formed with the n physical quantities is $n - p$, where p is the rank of the array α_{ij}. The relation

$$f(P_1, ..., P_n) = 0$$

is then equivalent to the relation

$$f(\Pi_1, ..., \Pi_{n-p}) = 0$$

where the parameters $\Pi_1, ..., \Pi_{n-p}$ are the dimensionless parameters that can be formed with the quantities P_1,P_2,...,P_n.

When

$$det \, |\alpha_{ij}| \neq 0$$

with $i, j \leq p$, there exist p independent quantities $P_1, P_2, ..., P_p$ and $n - p$ dependent quantities $P_{p+1}, P_{p+2}, ..., P_n$ that can be expressed by the independent ones as

$$P_{p+i} = \Pi_i \, P_1^{x_{i1}} \, P_2^{x_{i2}} ... P_p^{x_{ip}}$$

with $i = 1, 2, .., n - p$.

The expression

$$P_{p+i} = P_{p+i} \, a_1^{\alpha_{p+i1}} \, a_2^{\alpha_{p+i2}} ... a_m^{\alpha_{p+im}}$$

can be transform to

$$\alpha_{p+i,j} = \alpha_{1j} \, x_{i1} + \alpha_{2j} \, x_{i2} + ... + \alpha_{pj} \, x_{ip}$$

which is a system of m equations with p unknown quantities that can be solved as a normal equation system to obtain the exponents x_{ij}.

2.3.2   Main Dimensionless Parameters

The main physical quantities in the model are the pressure rise Δp, the velocity of the jet v_J, the density of the suctioned gases ρ_G, a characteristic length d_H, the mass flow of the jet $\dot{M}_J$ and the mass flow of the suctioned gases $\dot{M}_G$. For the problem of the injector it is of interest to obtain a relationship between the pressure rise Δp and the mass flow of the suctioned gasses. These relationships are done in order to generalize the results for different operating points or geometries as well as for checking the compressibility of the fluid and the ratio between the inertia forces and the viscosity forces.

With this duties the *Euler* number Eu

$$Eu = \frac{\Delta p}{\frac{1}{2}\rho_G v_J^2}, \tag{2.79}$$

the load coefficient μ

$$\mu = \frac{\dot{M}_G}{\dot{M}_J}, \tag{2.80}$$

the *Mach* number Ma

$$Ma = \frac{v}{c} \tag{2.81}$$

with the speed of the sound

$$c = \sqrt{\chi R T}$$

and the *Reynolds* number Re

$$Re = \frac{\rho v d_H}{\mu} \tag{2.82}$$

with d_H as the hydraulic diameter of the duct are calculated.

Chapter 3

Injector

3.1 Elements of an Injector

There are three main elements in an injector:

- the nozzle,
- the mixing duct and
- the diffuser.

So that, it would be useful to have a small description of each element.

3.1.1 Nozzle

The nozzle is the first element in the injector. Its main duty is to minimize the losses that could be caused by a sudden contraction of the fluid coming in the injector directly from the environment. Furthermore, it also accelerates this mass of induced gases before they reach the mixing duct. This can be managed by a gradual contraction of the section where the gases are running through, avoiding detachments or stalls in the stream.

Two kind of losses appear in a nozzle:

- friction losses and
- detachment losses.

In a long nozzle with a small contraction angle, no detachment is ensured, but the friction losses will be increased, so that, an optimal angle should be used to minimize the sum of both losses. This angle lies between 20^0 and 40^0.

The angle used for the injector nozzle is much smaller than the data given above. This can be justified by the fact that the main target here is avoiding unstable regimes and that the nozzle is short enough to neglect the losses. These losses can be calculated by

$$\Delta p = \zeta_2 \, \frac{\rho \, w_2^2}{2}. \tag{3.1}$$

Equation 3.1 is taken from [4] for angles smaller than 20^0, where w_2 is the velocity at the end of the nozzle and ζ_2 is a coefficient calculated by figure 3.1.
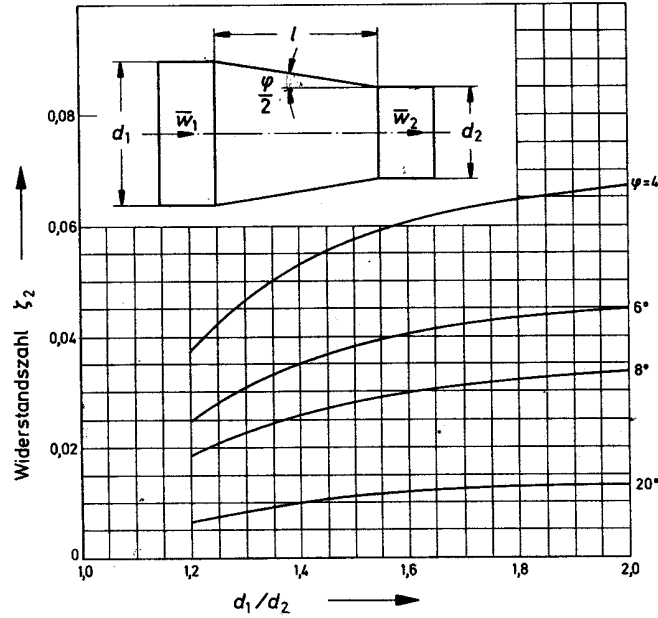
Figure 3.1: Coefficient ζ_2 [4].

3.1.2 Mixing Duct

Succeeding the nozzle, the suctioned fluid is pumped into the mixing duct. Once there, it will mix with the mass flow of the jet. Both circumstances lead to a situation of non-developed flow. The length of the region with this kind of flow regime can be calculated by

$$l_{na} = C_a \, Re \, d_H \approx (50...100) \, d_H, \tag{3.2}$$

where Re is the *Reynolds* number, d_H is the hydraulic diameter and C_a is a constant which values are by *Boussinesq*

$$C_a = 0,06...0,065$$

or by *Schiller*

$$C_a = 0,029.$$

Non-developed flow means that in the calculation of the losses the coefficients of the *Nikuradse* diagram cannot be used, but a loss coefficient according to *Brauer* [11] hast to be used. This coefficient takes the value of $\lambda_G = 0,025$.

The efficiency in the mixing pipe is not easy to calculate, so that the value given by *Schlag* [2] $\eta_{mix} = 0,9$ will be assumed as valid.

3.1.3   Diffuser

The diffuser is placed after the mixing duct. Its target is increasing the pressure of the mass flow which goes out from the mixing duct by converting the largest possible portion of dynamic pressure into static pressure.

The exit flow conditions and performance level of the diffuser are related to the presence of flow separation or stall. The maximum effectiveness is attained with a total angle between the diverging walls of approximately 7°.

To calculate the efficiency of this element η_{diff}, equation 3.3 given in [15] is used

$$\eta_{diff} = \frac{C_p}{C_{p_i}}, \tag{3.3}$$

where C_p is the static pressure recovery and C_{p_i} is the ideal static pressure recovery for one-dimensional flow which can be determinated by

$$C_{p_i} = 1 - \frac{1}{AR^2} \tag{3.4}$$

with $AR = \frac{Width\,at\,the\,end\,of\,the\,diffuser}{Width\,at\,the\,beginning\,of\,the\,diffuser}$ as area ration of the diffuser.

In order to obtain all these values, some parameters must be fixed first. Figure 3.2 is used to obtain a value for the ratio $\frac{length\,of\,the\,diffuser}{width\,at\,the\,entrance}$. With an angle equal to 8°, a value of 5 is chosen for this ratio, which ensures the flow field is in a region where there is no appreciable stall.

With the fixed length and the fixed angle is possible to calculate the area ratio AR and with the area ratio AR the ideal static pressure recovery C_{p_i}. The value obtained for the area ratio is

$$AR = \frac{W_1 + 2L\tan\theta}{W_1} = 1 + 2\frac{L}{W_1}\tan\frac{\Theta}{2} = 1,699.$$
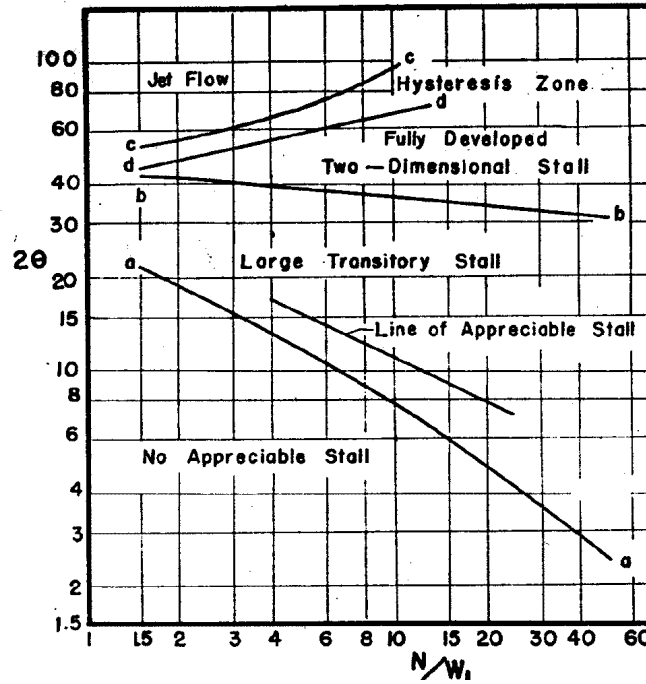
Figure 3.2: Flow regimes in straight-wall, two dimensional diffusers [15].

The static pressure recovery can be calculated with figure 3.3. As the factor $\frac{2\delta_1^*}{W_1}$ is unknown, an intermediate value $\frac{2\delta_1^*}{W_1} = 0,015$ was chosen. With $\frac{2\delta_1^*}{W_1} = 0,015$ the static pressure recovery becomes

$$C_p = 0,57.$$
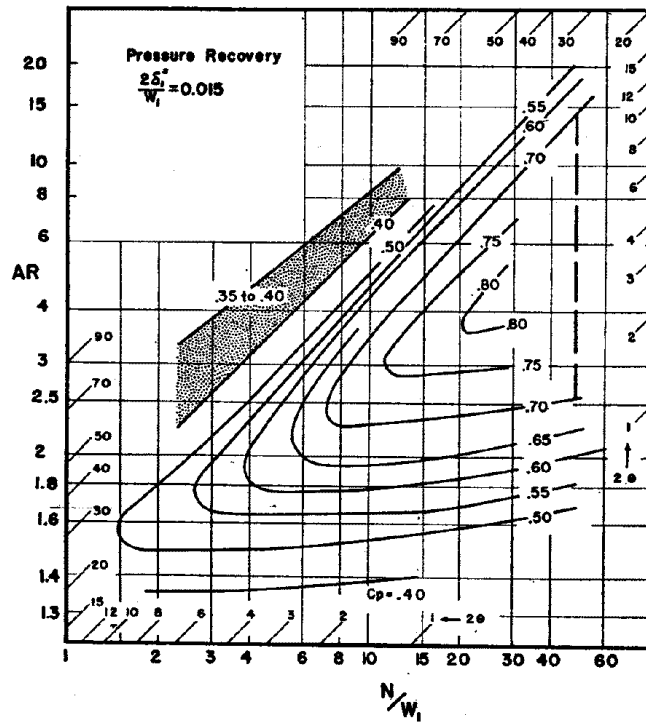
Figure 3.3: Static pressure recovery [15].

With these data the efficiency of the diffuser is $\eta_{diff} = 0,9$.

3.2 Confined Jet

3.2.1 Plane Jet

The jet makes the job of suctioning gases from the environment and coming over the pressure at the end of the injector.

The flow of a confined jet discharging into the same fluid can be separated in four different regions:

1. The first one is known as the development region and consists of two potential flow zones with different velocities separated by a shear layer. These regions are the potential core of the jet and the mass of suctioned gases. The shear layer increases with the distance from the nozzle, erasing the potential core of the jet. The disappearance of the potential core indicates the end of this region. There is also another shear layer at the walls of the duct.

2. In the second region, the shear zone extends from the center line to the outer uniform flow, which can be considered as a potential flow. This region ends when the potential flow has disappeared.

3. The third region is entirely a region of shear flow. Recirculation of the flow is possible here.

4. Finally, at the end of the third region the flow can degenerate in a fully developed flow when the duct is long enough.

Considering a plane jet coming from a nozzle of semi-height $\frac{W_J}{2}$ with a uniform velocity, discharging symmetrically in a plane duct of semi-height $\frac{W_M}{2}$, the equations of motion are the balance of momentum in the injector´s axial direction X

$$v_x \frac{\partial v_x}{\partial x} + v_y \frac{\partial v_x}{\partial y} = -\frac{1}{\rho}\frac{dp}{dx} + \frac{1}{\rho}\frac{\partial \tau}{\partial y} \tag{3.5}$$

and the continuity equation

$$\frac{\partial v_x}{\partial x} + \frac{\partial v_y}{\partial y} = 0. \tag{3.6}$$

Integrating 3.6 it is obtained that the discharge Q per unit width is constant along the injector axis. Neglecting the shear stress in equation 3.5, the balance of momentum can be reduced to

$$\frac{d}{dx} \int_0^{\frac{W_M}{2}} \left(p + \rho v_x^2 \right) dy = 0, \tag{3.7}$$

which states that the pressure plus momentum is also constant along the injector axis.

3.2.2   Study of the Principal Flow Regimes

Subtracting the jet´s discharge per unit width Q_1 from the injector´s total discharge per unit width Q, the secondary stream´s discharge per unit width Q_2 is obtained

$$Q_2 = Q - Q_1 \tag{3.8}$$

The secondary stream´s discharge per unit width Q_2 can be used for a study of the principal flow regimes:

- At an appreciably high Q_2 the jet expands symmetrically in the duct.

- If Q_2 decreases, recirculating regions appear on both sides of the injector axis.

- If Q_2 decreases further, the eddies grow in size and are unequal in spatial extension. At still lower discharges, these eddies start to oscillate. The oscillation of the jet reaches a maximum value when the entire nozzle discharge flows back into the supply duct of the secondary stream. When this occurs, the load coefficient μ becomes negative. The load coefficient is defined as

$$\mu = \frac{\dot{M}_G}{\dot{M}_J}$$

where $\dot{M}_G$ is the mass flow of the secondary stream or the suctioned gases, and $\dot{M}_J$ is the mass flow of the jet. This parameter will be used later on.
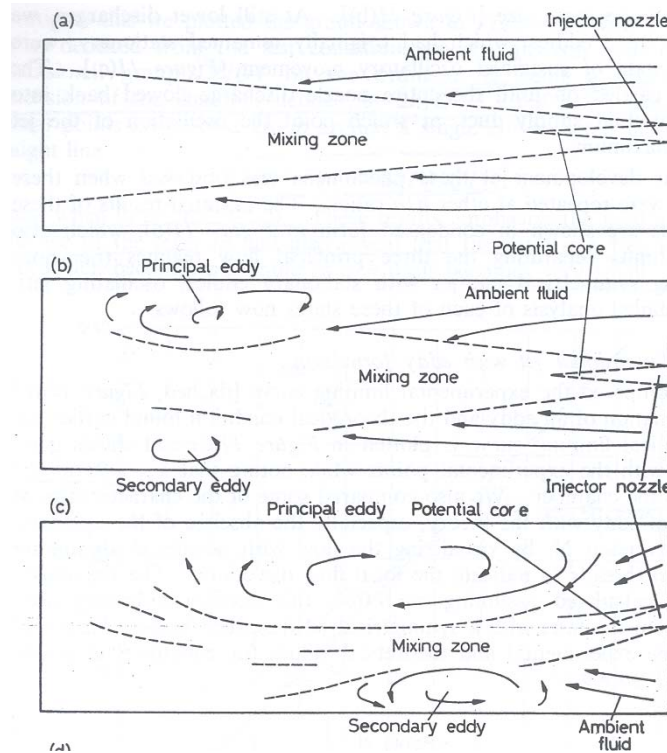
Figure 3.4: Two-dimensional jet (a) without and (b) with eddy formation. (c) Oscillating two-dimensional jet instantaneous view [8].

Figure 3.4 gives an idea of the nature of the flow field. Figure 3.5 shows the flow characteristics with the paameter $\frac{Q}{Q_1}$ and $\frac{W_M}{W_J}$.
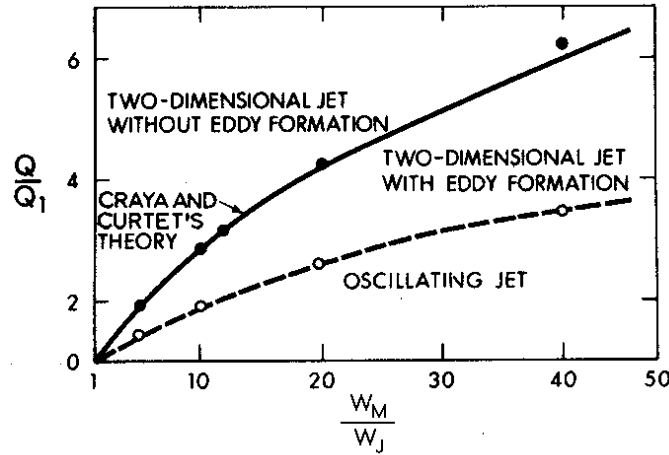
Figure 3.5: Flow characteristics of plane confined jets [3].

In order to study the flow with oscillating jets, it is useful to define a dimensionless characteristic parameter $\overline{m}$

$$\overline{m} = \frac{M}{\rho}\frac{W_M}{Q^2},\qquad(3.9)$$

where M is the pressure plus momentum in the axial direction.

In case of oscillating jets, variations upstream and downstream of the recirculating regions is a function only of the parameter $\overline{m}$. The oscillation period T occurring at various primary and secondary discharge ratios can be calculatedfor $\overline{m} > 2$ according to *Curtet* [8] by

$$\frac{\overline{h}^2}{QT} = 0,02\sqrt{\overline{m}} - 0,029,\qquad(3.10)$$

where

$$\overline{h} = \frac{\frac{W_M}{2}}{0,5 + 1,65\frac{W_J}{W_M}}.\qquad(3.11)$$

$\overline{h}$ approaches W_M when the ratio $\frac{W_J}{W_M}$ becomes very small.

Chapter 4

Injector Geometry

4.1 Model by *Schlag* [2]

4.1.1 Pressure Variation in a Gas-Gas Injector

Schlag divides the gas-gas injector for his model in three main parts: the nozzle, the mixing duct and the diffuser. With this model of injector, he considers that the mean pressure along an injector axis changes by the following facts:

- The pressure drop in the nozzle Δp_{nozz} due to the acceleration of the suctioned gases.

- The pressure rise in the mixing duct Δp_{mix} due to the mixing out of the jet and suctioned gases.

- The pressure loss caused by the wall roughness in the mixing duct $\Delta p_{r,mix}$.

- The pressure rise in the diffuser Δp_{diff} due to the deceleration of the flow.

The model of *Schlag* neglects the pressure loss by wall friction in the nozzle as well as in the diffuser and considers constant density for all the fluid mass, so that, all the calculations are made according to this suppositions.

In the nozzle the suctioned gases raise their speed from a velocity v_A at the beginning up to a velocity v_E at the end of it. This velocity can be calculated with the continuity equation considering also the area of the jet duct A_J. This area can be calculated with the mass flow $\dot{M}_J$, the density ρ_J and the velocity v_J of the jet by

$$A_J = \frac{\dot{M}_J}{\rho_J v_J} \, . \tag{4.1}$$

Then the velocity of the suctioned gases at the end of the nozzle v_E is obtained by

$$v_E = \frac{\dot{M}_G}{\rho_G (A_M - A_J)} \tag{4.2}$$

where A_M is the area at the entrance of the mixing duct, A_J is the area of the jet, $\dot{M}_G$ stands for the mass flow and ρ_G for the density of the suctioned gases.

The pressure fall in the nozzle due to the acceleration of the suctioned gases is

$$\Delta p_{nozz} = \frac{\rho_G}{2}(v_A^2 - v_E^2) \, . \tag{4.3}$$

In order to calculate the pressure rise in the mixing duct, some quantities must be defined first. The mean velocity of the gases at the end of the mixing duct v_M can be calculated by

$$v_M = \frac{\dot{M}_J + \dot{M}_G}{\rho_G A_M} \, . \tag{4.4}$$

The efficiency of the mixing duct η_{mix} gives the part of momentum transmitted in the mixing duct.

The load coefficient μ is defined as

$$\mu = \frac{\dot{M}_G}{\dot{M}_J} \, . \tag{4.5}$$

The change in the pressure along the mixing duct due to the mixing of the jet and the suctioned gases is

$$\Delta p_{mix} = \dot{M}_J \frac{(v_J - v_M) + \mu(v_E - v_M)}{A_M} \eta_{mix} \, . \tag{4.6}$$

In the mixing duct, there are pressure losses due to the roughness of the walls. These are considered and can be expressed by

$$\Delta p_{r,mix} = -\lambda_G \frac{L_M}{2W_M} \frac{\rho_G}{2} v_E \, v_M. \tag{4.7}$$

The dynamic pressure $\frac{\rho_G}{2} v_E v_M$ is calculated with the geometrical medium between the velocity at the beginning and the velocity at the end of the mixing duct. First calculations would be made with the loss coefficient λ_G taken from the *Nikuradse* diagram, shown in figure 4.1. This λ_G is conditioned by the *Reynolds* number and the roughness of the wall. Bearing in mind that in these cases the behaviour of the flow field is neither turbulent nor laminar, the λ_G will be more influenced by one or another factor depending whether the flow profile is closer to a laminar flow or a turbulent one. If the flow is almost laminar, the coefficient depends mainly on the *Reynolds* number. If the flow is almost turbulent, it will be influenced also by the roughness of the wall. *Brauer* [11] took a value for $\lambda_G = 0,02$.
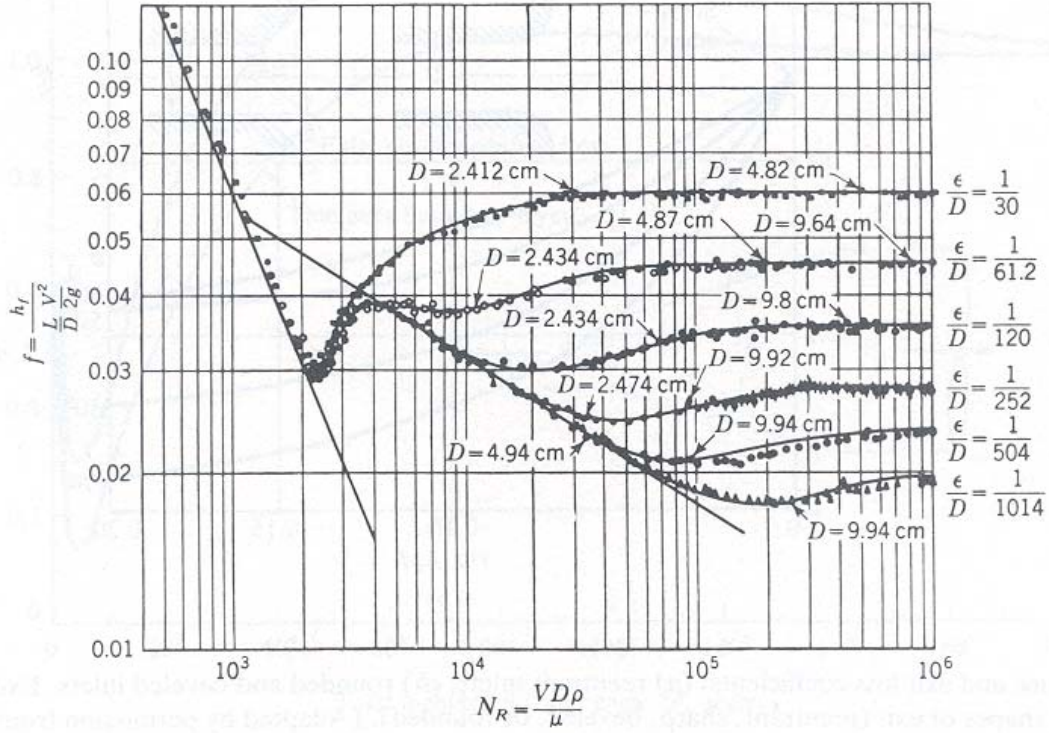
Figure 4.1: *Nikuradse* diagram [7].

When practical measurements are done in order to obtain the pressure drop in a real duct, the values obtained for the coefficient λ_G are larger than those obtained by interpolation of the *Nikuradse* lines because at the beginning of the mixing pipe the flow is not fully developed.

Schlag evaluates his measurements and obtained a value of $\lambda_G = 0,025$.

An optimal length of the mixing duct is obtained when the pressure at the end of the duct is a relative maximum.

In the diffuser the gases are decelerated from the velocity v_M to the velocity v_F producing as a consequence a the pressure rise Δp_{diff} expressed by

$$\Delta p_{diff} = \eta_{diff} \frac{\rho_G}{2} \left(v_M^2 - v_F^2 \right). \tag{4.8}$$

Compiling all what have been reckoned above, the variation in the pressure for a one phase gas-gas injector is equal to

$$\Delta p = \Delta p_{nozz} + \Delta p_{mix} + \Delta p_{r,mix} + \Delta p_{diff}. \tag{4.9}$$

4.2   Calculation of the Geometry

4.2.1   Requirements to the Injector

Using the model by *Schlag* a plane injector is designed for the following requirements:

27

- Gases with environmental conditions ($T_0 = 15°C$, $p_0 = 1\,bar$, $v_A = 0^m/_s$) are suctioned at a rate of $10^{kg}/_{m\,s}$ overcoming a pressure rise of $1000\,Pa$.

- The injector is driven by a jet with a velocity of $v_J = 200^m/s$ and a total temperature $T_J^0 = 30°C$. The load coefficient μ defined in equation 4.5 is desired to be $3,75$.

The following hypotheses are made for the fluid:

- The fluid is incompressible, so that ρ is constant.

- The fluid is assumed to be ideal with the following constant properties: $c_p = 1004,5\,^J/_{kg\,K}$ and $R = 287\,^J/_{kg\,K}$.

The dimensions of the injector are fixed by the following rules:

- The length of the mixing duct L_M is taken, according to *Schlag* [2], as 6 times the height of the entrance

$$\frac{L_M}{W_M} = 6. \tag{4.10}$$

- The diffuser angle is $2\theta = 8^o$ according to chapter 3.1.3.

- The length of the diffuser L_D, according to chapter 3.1.3, is 5 times the height of the mixing duct

$$\frac{L_D}{W_M} = 5. \tag{4.11}$$

- The length of the nozzle L_N is equal to the width at the entrance of the mixing duct W_M

$$\frac{L_N}{W_M} = 1. \tag{4.12}$$

- The thickness of the jet duct t_J is taken as $t_J = 2\,mm$.

And finally some constants are chosen for the thermodynamic models:

- The efficiency of the mixing duct is equal to $\eta_{mix} = 0,9$, according to *Schlag* [2].

- The coefficient $\lambda_G = 0,025$, according to *Schlag* [2].

- The efficiency of the diffuser is set to $\eta_{diff} = 0,9$, as explained in chapter 3.1.3

4.2.2 Calculation of Pressure Rise

Starting with the jet, the calculations have been done in the following way:

The temperature of the air at the end of the jet duct T_J is calculated by

$$T_J = T_J^0 - \frac{1}{2c_p}\, v_J^2.$$

The pressure at the end of the jet duct p_J is approximated as

$$p_J \approx 1\, bar.$$

So that, the density will be

$$\rho_J = \frac{p_J}{RT_J}. \tag{4.13}$$

The jet mass flow is also known due to the given load coefficient:

$$\dot{M}_J = \frac{\dot{M}_G}{\mu}. \tag{4.14}$$

The height of the jet W_J is calculated by

$$W_J = \frac{\dot{M}_J}{\rho_J\, v_J}. \tag{4.15}$$

Applying equations 4.13, 4.14, 4.15 to the practical case, the values of table 4.1 have been obtained for the jet.

Table 4.1: Parameters of the jet.

Temperature T_J	$283,24\,K$
Density ρ_J	$1,23\,{}^{kg}/_{m^3}$
Mass Flow M_J	$2,67\,{}^{kg}/_{s\,m}$
Width W_J	$10,84\,mm$

The pressure gain in the plane injector is calculated as follows:

The pressure in the nozzle will vary according to equation 4.3. With the consideration of $v_A = 0$ the pressure drop in the nozzle is

$$\Delta p_{nozz} = -\frac{\rho_G\, v_E^2}{2}. \tag{4.16}$$

Introducing a dimensionless factor a

$$a = \frac{W_M}{W_J} \tag{4.17}$$

and equation 4.5, equation 4.2 can be transformed to

$$v_E = \frac{\dot{M}_G}{\rho_G \left(W_M - W_J - 2t_J \right)} = \frac{\mu_G \, \dot{M}_J}{\rho_G \left[W_J(a-1) - 2t_J \right]}.$$

The pressure rise in the mixing duct is given by equation 4.6. Inserting the parameter a, the losses can be calculated as

$$\Delta p_{mix} = \dot{M}_J \, \frac{\left(v_J - v_M \right) - \mu \left(v_E - v_M \right)}{a \, W_J} \eta_{mix}$$

with

$$v_M = \frac{\dot{M}_J \left(\mu + 1 \right)}{\rho_G \, a \, W_J},$$

as the velocity at the end of the mixing duct.

The pressure rise along the diffuser is given by equation 4.8, but the velocity at the end of the diffuser is unknown yet. A relation between the velocity at the beginning and at the end of the diffuser must be found first. This can be done using the geometric parameters and the constant mass flow equation.

By geometry

$$W_F - W_M = 2 \, L_D \, \tan \theta.$$

By constant mass flow

$$W_M \, \rho_M \, v_M = W_F \, \rho_F \, v_F.$$

Taking ρ as constant, v_M as the velocity at the entrance of the diffuser and v_F as the velocity at the end of the diffuser, the ratio $\frac{v_F}{v_M}$ is given by

$$\frac{v_F}{v_M} = \frac{1}{1 + 2 \, \frac{L_D}{W_M} \, \tan \theta}. \tag{4.18}$$

Introducing equation 5.1 in equation 4.8 the pressure rise can be expressed by

$$\Delta p_{diff} = \eta_{diff} \, \frac{\rho_G}{2} \, v_M^2 \left[1 - \left(\frac{1}{1 + 2 \, \frac{L_D}{W_M} \, \tan \theta} \right)^2 \right]. \tag{4.19}$$

The losses in the mixing duct can be obtained using equation 4.7.

Once this has been done, the net pressure rise is calculated by summing up the pressure rises and drops in the elements according to equation 4.9.

Varying the ratio a, the points of figure 4.2 are obtained. This figure shows the pressure rise depending on this parameter.
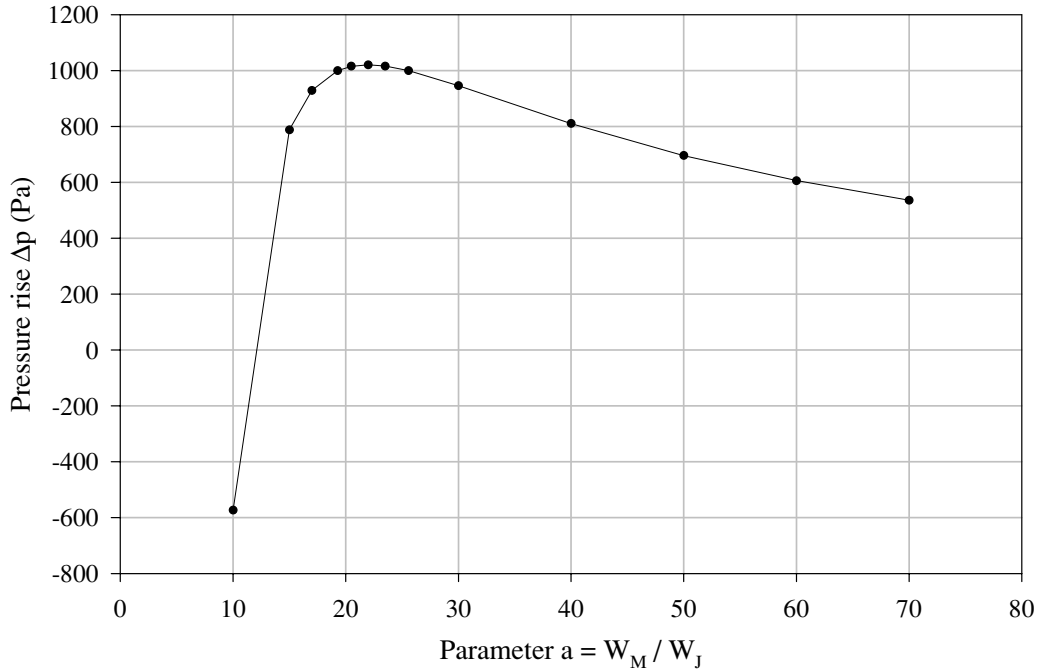
Figure 4.2: Net pressure rise in the injector for different values of the parameter a

Looking at the figure 4.2, there are two values of the parameter a that carry out the requirements established before. These values are shown in table 4.2.

Table 4.2: Values of the parameter a which carry out the requirements.

a_1	$19, 28$
a_2	$25, 58$

These two ratios give two possible injector geometries.

4.2.3   Calculation of the Geometry

Once these values have been obtained, it must be decided which geometry should be used. The one with the larger ratio $\frac{W_M}{W_J}$ or the one with the smaller. This will depend on the conditions of the problem and its requirements. In this case the smaller one is chosen, because it is required a small geometry with the capability to overcome the design pressure rise for a constant jet mass flow.

The characteristics for both possible injector geometries are shown in figure 4.3. It can be noticed that for the larger ratio of heights, small fluctuations in the load coefficient μ give almost no variation in the pressure rise, so that, the injector with this geometry can be used when the jet flow rate is not that constant as required and the pressure rise is desired to be nearly constant. For the small injector, a larger range of pressure rises can be overcome when changing the load coefficient.
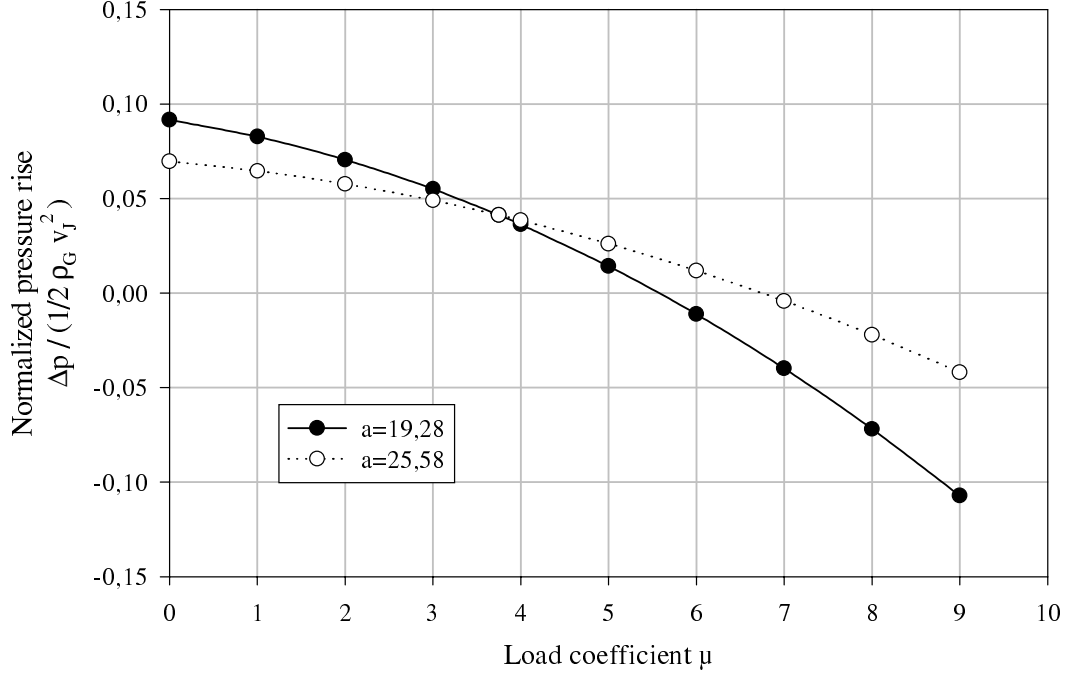
Figure 4.3: Characteristics for both possible injector geometries using the model by *Schlag*.

The model by *Schlag* uses only average values in different control planes. Thus, only the width of those control planes can be determined. The length of the nozzle, the mixing duct and the diffuser are determined by equations 4.10, 4.11 and 4.12. The shape of the walls is not necessary for the model by *Schlag*. The profile of the diffusor is chosen to be a straight line, and for the remaining elements, the nozzle and the mixing duct, two different profiles will be investigated.

1. The first shape consists of straight lines between the control planes.

2. The second shape is constructed by drawing a circle being tangent to the diffuser and passing through the calculated heights at the beginning of the nozzle and at the beginning of the mixing duct.

   The radius of the circle R_d can be calculated by

$$R_d = \frac{\frac{1}{2} L_M}{\sin \theta} \tag{4.20}$$

with θ as the half of the angle of the diffuser.

The nozzle width W_A is calculated for both geometries by

$$W_A = \frac{W_M}{2} + R_d \left(1 - \cos \alpha\right) - R_d \left(1 - \cos \theta\right) = \frac{W_M}{2} + R_d \left(\cos \theta - \cos \alpha\right) \tag{4.21}$$

with

$$\alpha = \arcsin \frac{\frac{1}{2} L_M + W_M}{R_d}. \tag{4.22}$$

Both geometries are plotted in figure 4.4 and 4.5.
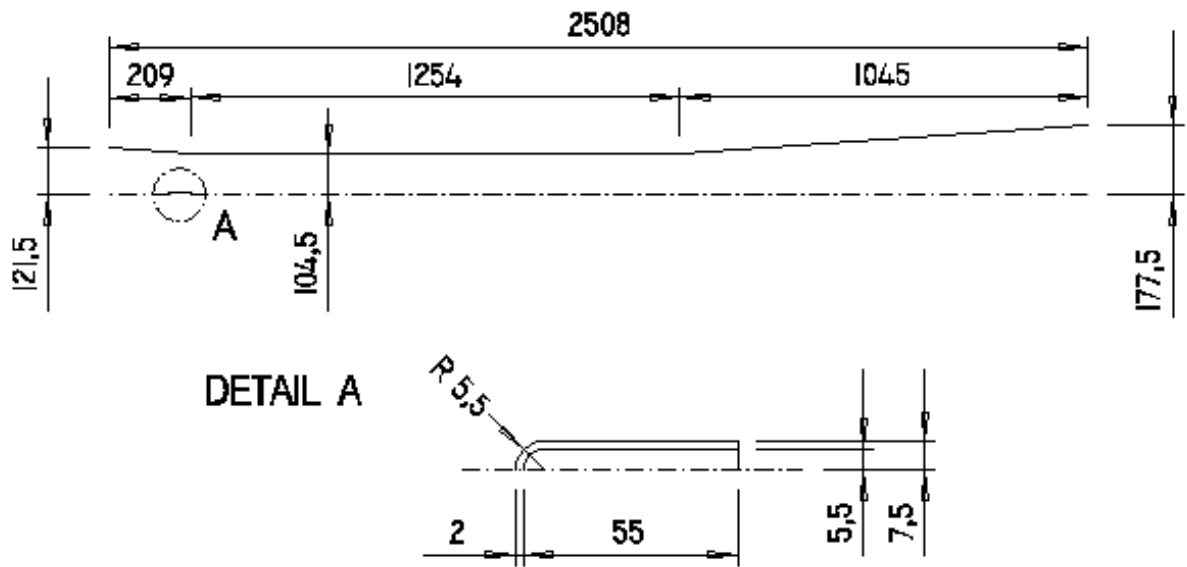
Figure 4.4: Half injector with constant width mixing duct.
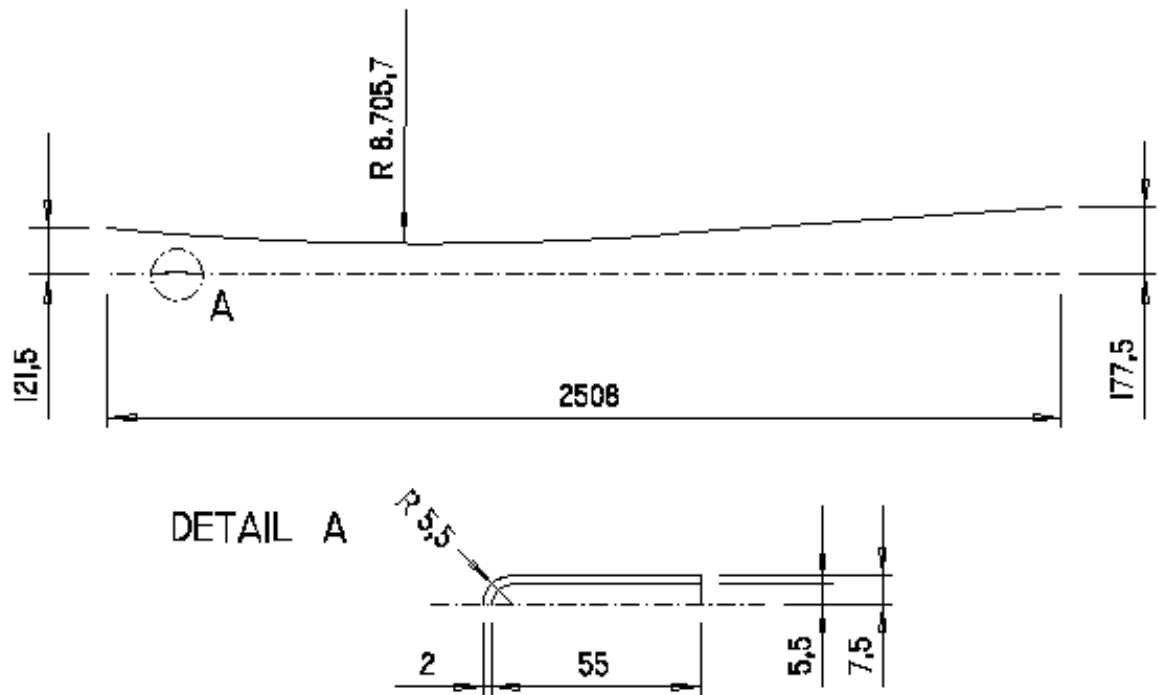
Figure 4.5: Half injector with a circle as wall shape.

Chapter 5

Model Used in CFD

Once the necessary values to draw the geometry are fixed, the injector can be modelled in a program which uses CFD codes. With this program the flow in different operating points will be analyzed. The results will be compared with the results obtained by the model of *Schlag*.

5.1 Building the Model

Before starting the calculations an appropriate model has to be chosen.

5.1.1 Half or Full Geometry

By the drawings of the injector, the injector can be considered as a symmetric object in order to simplify the calculations and make them faster. Considering only half of the injector makes the number of nodes smaller and, as a consequence, the time required for the calculations is shorter. But the property of symmetry can only be used successfully when the flow is symmetric, too. A non-symmetric flow field for instance, eddies of different sizes on both sides of the jet, cannot be modelled by the half geometry. The load coefficient is calculated with the results of the inlet flow through the boundaries of the model and changes for a non-symmetric flow depending on the use of a symmetric or a non-symmetric model.

5.1.2 Steady or Unsteady

As in the previous case, depending on the conditions of the problem, the flow field can change with time. This occurs when the conditions for a swinging jet are reached. In these cases, the steady state solution is not reliable physically.

If the example of the load coefficient is taken again, a similar situation to the one before appears. When the jet swings, the outlet flow through the boundaries changes with time. The instantaneous load coefficient calculated with the mass flow through the boundaries changes with time, too.

In cases of a transient flow, a proper time step width must be chosen in order to get useful results for every time step. Splitting up one jet period into twenty time steps ensures good enough results to get proper average values. Also the changing flow field is expected to be resolved well.

5.2   Boundaries and Turbulence

The boundary conditions are chosen in order to cause an adequate change of pressure from the beginning to the end of the injector. This change is done both for the design case and for different cases where the observation of jet reactions, output values for the flow or the display of any magnitude is interesting. To obtain correct output values the following steps must be beard in mind.

5.2.1   Inlet Boundaries

At the jet nozzle an inlet boundary is applied. At an inlet boundary the velocity components, the turbulent kinetic energy and the turbulent dissipation rate have to be specified. For a compressible calculation the temperature must be specified additionally. The pressure is extrapolated during the solution process from downstream flow data.

The turbulent kinetic energy, k, comes by the fluctuating values of the velocity, and it can be expressed by

$$k = \frac{1}{2}\left(\overline{v_x'^2} + \overline{v_y'^2} + \overline{v_z'^2}\right) = \frac{1}{2}\overline{v_i' v_i'}. \tag{5.1}$$

Assuming isotropic turbulence

$$\overline{v_x'^2} = \overline{v_y'^2} = \overline{v_z'^2}$$

equation 5.1 can be written as

$$k = \frac{3}{2}\overline{v'^2}. \tag{5.2}$$

Introducing in equation 5.2 the turbulent intensity T_v, defined as

$$T_v = \frac{\sqrt{\overline{v'^2}}}{v}, \tag{5.3}$$

the turbulent kinetic energy k can be expressed by

$$k = \frac{3}{2}(T_v\, v)^2. \tag{5.4}$$

The turbulent intensity T_v is chosen to be $0,035$.

According to equation 2.69, the turbulent dissipation rate ε can be specified by

$$\varepsilon = \frac{k^{\frac{3}{2}}}{\underline{l}}.$$

The dissipation length scale is set to be equal to the width of the jet nozzle

$$\underline{l} = W_J.$$

5.2.2 Pressure Boundaries

Pressure boundaries were used at the inlet and at the outlet of the flow domain because there was no information about the velocity distribution.

The "environmental" inlet models the envinronment. A total pressure boundary condition was specified to ensure a correct modeling of the environmental conditions. The total temperature was also specified for calculations with compressible fluid.

During the solution process the static pressure is extrapolated from downstream flow data and the velocity is calculated by the model of isentropic acceleration of the fluid. *Neumann* boundary conditions, i.e. zero normal gradients, are imposed on the velocity components and zero gradients on the turbulence quantities k and ε.

At the outlet of the flow domain a static pressure boundary condition was applied. *Neumann* boundary conditions are imposed on the velocity components, on the turbulence quantities k and ε, and also on the temperature for compressible calculations. The outlet of the flow domain was located round one diffuser length downstream of the end of the diffuser to ensure there is no local influence of the pressure boundary condition on the velocity components.

The diffuser and the outlet were connected by a so called tail pipe. Although additional losses by numerical dissipation and by mixing out of the flow were expected in the tail pipe, the obtained results how that these losses are low compared to the pressure rise of the injector.

5.2.3 Symmetry Boundaries

For the symmetric model of the injector a symmetry boundary condition was applyed at the axis of the injector. At a symmetric boundary condition, the *Neumann* boundary condition is imposed on all physical quatities.

5.2.4 Wall Boundaries

The no-slip condition was imposed for the velocity components on the walls. For compressible calculations the walls are set to be adiabatic. The high *Reynolds* number $k - \varepsilon$ turbulence model with wall functions was used to model the boundary layer.

The use of a wall function as implemented in the CFD-code demands a dimensionless wall distance y^+, calculated with the thickness of the first cell adjacent to the wall, in the range

$$30 \leq y^+ \leq 100.$$

Because of the complex geometry and because of the loacally high gradients of quantities, the mesh could be refined at least so far that all the dimensionless wall distances were in a range

$$15 \leq y^+ \leq 200.$$

Chapter 6

Results

6.1 Incompressible Fluid

6.1.1 Injector Characteristics by the Model of *Schlag*.

The model of *Schlag* is calculated with the assumption of incompressible fluid. The different widths of the injector planes such as that at the beginning or that at the end of the mixing pipe have been calculated with this condition. Once this has been done, the characteristic curve of the injector can be calculated. This curve shows the correlation between the pressure rise and the load coefficient.

The densities have been calculated according to the hypotheses made for the ambient temperature and for the total temperature of the jet. They are shown in table 6.1.

Table 6.1: Values used for the temperature and density.

Temperature of the jet T_J	$283,24\,K$
Density of the jet ρ_J	$1,23\,^{kg}/_{m^3}$
Temperature of the ambient T_a	$288,15\,K$
Density of the ambient ρ_G	$1,21\,^{kg}/_{m^3}$

Figure 6.1 shows the characteristic curve of the injector according to the model of *Schlag*. This curve shows the normalized pressure rises that the injector can come over for different load coefficients.

The characteristic curves of both injectors with different wall shapes are the same because the wall shape has no influence in this model, at least so far as the efficiency of the mixing duct does not change.
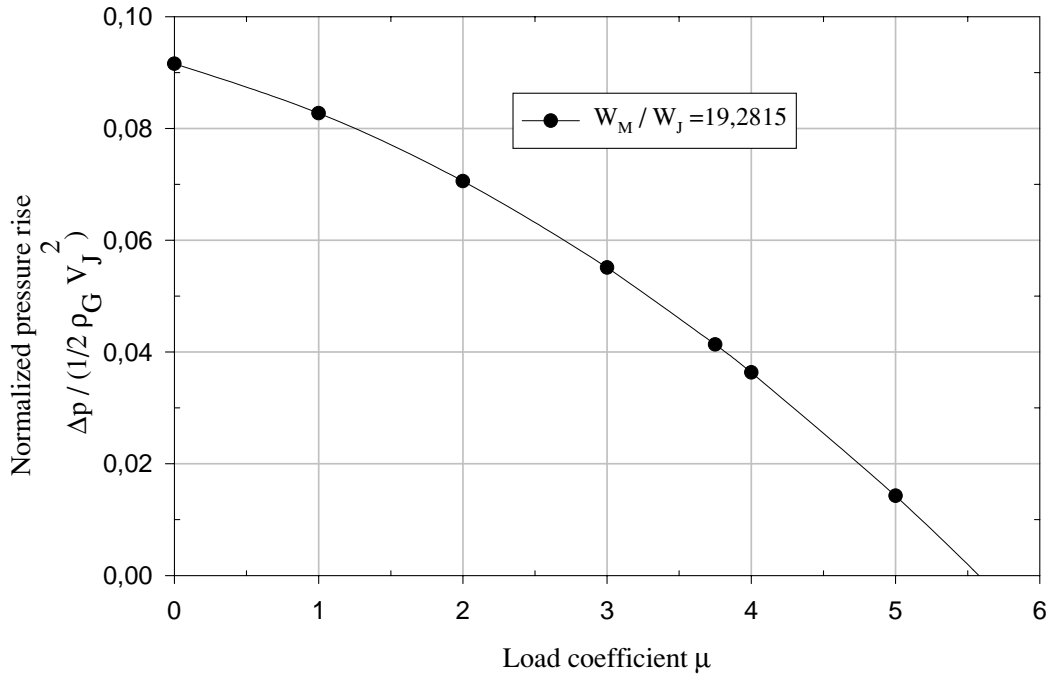
Figure 6.1: Characteristic curve of the injector by the model of *Schlag* for a constant jet mass flow.

In figure 6.1 there is no distinction between taking one half of the injector cutted by its symmetry plane or considering the whole injector. The reason of making no distinction is implicit in that model. This model only considers the ratio $\frac{W_M}{W_J}$ and different load coefficients to get the pressure rises at the end of the diffuser. *Schlag* does not take into account the generation of non-symmetrical flow or the swing of the jet when the pressure at the outlet is higher than in the design point. This model assumes the flow field as steady, even in operating points with a low load coefficient, where according to *Curtet* [8] the flow is transient.

6.1.2 Injector Characteristic by CFD Model

The CFD model will give an accurate visualization of the flow field inside the injector for different pressures at the end of the diffuser as well as the possibility of obtaining the load coefficient.

6.1.2.1 Injector with Straight Lines as a Wall Shape

In the straight lines geometry the mixing duct has a constant width. A constant width mixing duct makes the structure easier to build than any other feasible geometry. It will be shown that both the efficiency and the load coefficients are lower than for the geometry with a circle line as a wall shape. The decrease of the load coefficient for the same pressure at the end of the diffuser results also in the appearance of vortices and asymmetries at lower pressures.

Starting with half geometry calculations have been made for a pressure rise range from $\Delta p = 0\,Pa$ to $2500\,Pa$.

First the flow field of the design point was calculated and the results are analyzed.

The flow field is as expected for a confined jet. High gradients in the v_x velocity at the beginning of the mixing duct with a strong shear stress region and a progressive dissappearance of the jet at the same time as the shear stress region grows. The high gradients are present while the potential core of the jet exists. An interpolation of the v_x velocities and its flow field at the beginning of the mixing duct are shown in figures 6.2 and 6.3.
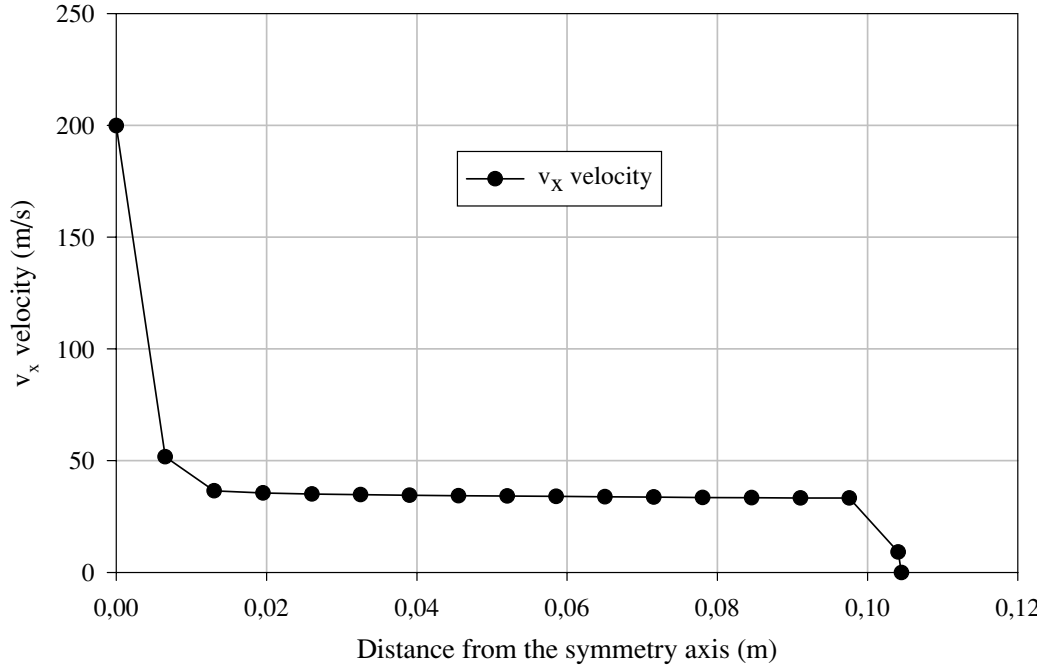
Figure 6.2: Interpolation of the values of v_x at the beginning of the mixing duct.

At the end of the mixing duct an enterly region of shear flow should be reached. Doing a graph with the interpolated values of the v_x velocity, it is found that the v_x is not constant. This means that the maximum pressure that can be reached in the mixing duct is not achieved as assumed in the theory by *Schlag* [2]. The profile of the v_x velocity is almost constant at the end of the diffuser. This means there will not be a rise in the pressure along the tail duct, as required for the CFD model in the chapter 5. Both velocity profiles are shown in figure 6.4.
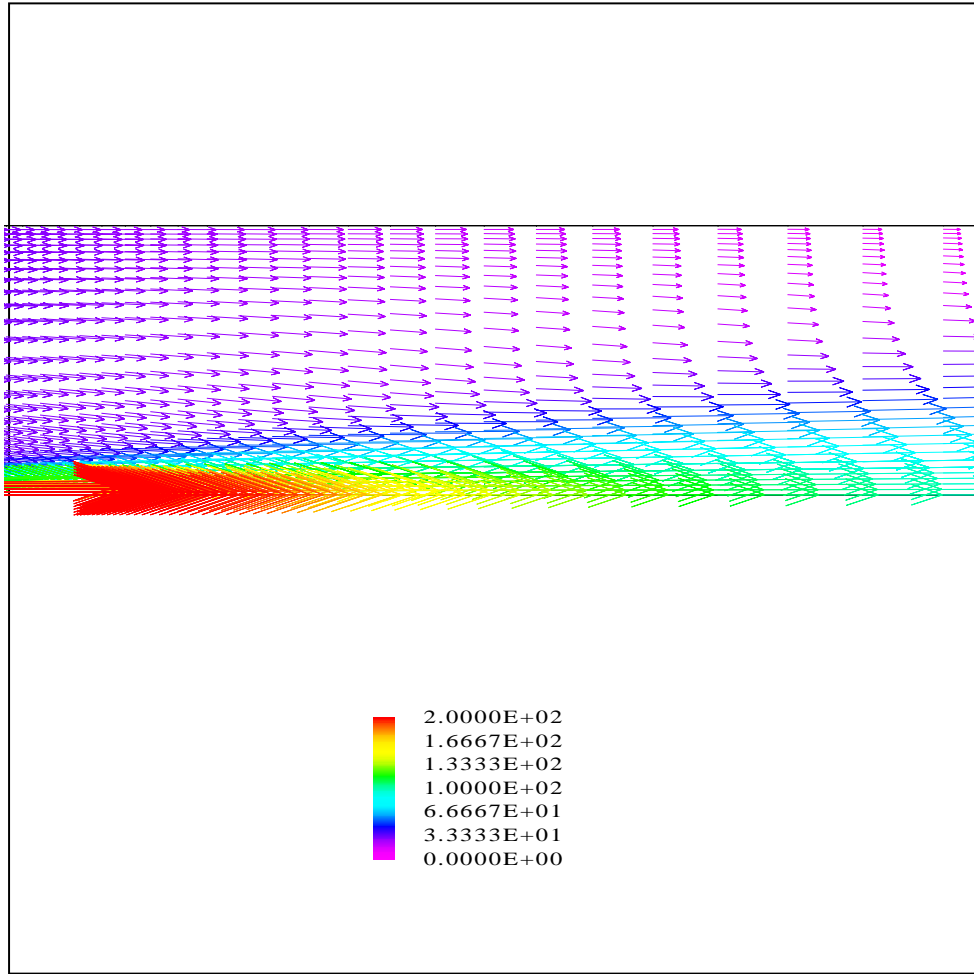
Figure 6.3: Velocity vector field at the beginning of the mixing duct, design point, colored with v_x velocity.
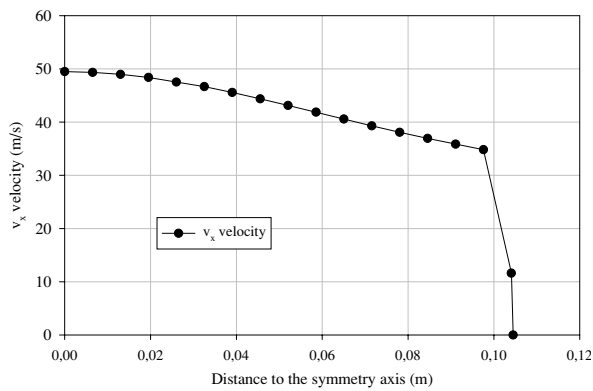
Interpolation of the v_x velocity at the end of the mixing duct.
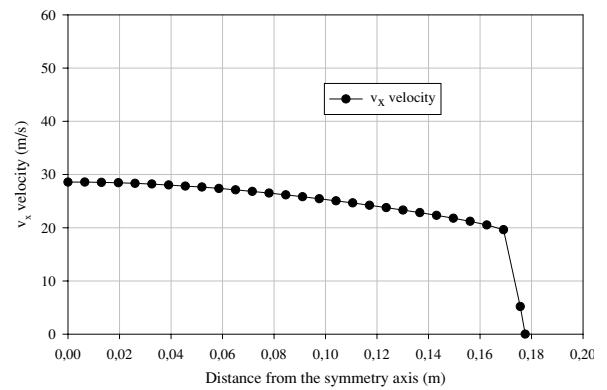
Interpolation of the v_x velocity at the end of the diffuser.

Figure 6.4: Interpolation for the v_x velocity in the injector at the end of the mixing duct and at the end of the diffuser at the design point for half geometry.

Furthermore, the load coefficient can be calculated. It is obtained $\mu = 3,05$, lower than expected by the model of *Schlag*. This result creates the necessity of checking the efficiency in the injector as a possible explanation for this lower value.

In the interval from $\Delta p = 0\,Pa$ to $2500\,Pa$, calculations have been made for the following points: $\Delta p = 0$, 550, 1000, 1500, 2000 and $2500\,Pa$. The load coefficients of table 6.2 were obtained by these calculations.

Table 6.2: Values of the load coefficient for the straight lines geometry cutted by the symmetry plane and incompressible fluid.

$\Delta p = 0$ Pa	$\mu = 4,168$
$\Delta p = 550$ Pa	$\mu = 3,583$
$\Delta p = 1000$ Pa	$\mu = 3,050$
$\Delta p = 1500$ Pa	$\mu = 2,248$
$\Delta p = 2000$ Pa	$\mu = 1,350$
$\Delta p = 2500$ Pa	$\mu = 0,212$

When modeling only a half of the geometry no problems are supposed to exist for the design point. However, for higher pressure rises, or what is the same, for lower load coefficients, there is the possibility that vortices are formed with unequal extension in size at both sides of the symmetry plane or even that the jet swings. If this phenomenon occurs, the results of the half geometry will not be reliable. To have an idea about when the vortices will appear figure 3.5 is used.

In this figure and for the value of $\frac{W_m}{W_J} = 19,2815$ it is found that the eddy formation starts at a value $\frac{Q}{Q_1} = 4$ and the oscillating jet starts at a value of $\frac{Q}{Q_1} = 2,5$. To express this ratio by the load coefficient the following development is done:

$$\frac{Q}{Q_1} = \frac{Q_1 + Q_2}{Q_1} = 1 + \frac{Q_2}{Q_1} = 1 + \mu. \tag{6.1}$$

So that, the formation of eddies starts for a $\mu = 3$ and the jet starts swinging at a $\mu = 1,5$.

In figure 6.5 the velocity vector flow field is shown for $\Delta p = 2500\,Pa$ and $\mu = 0,212$. The formation of eddies can be seen clearly in this figure. Because of using a symmetry plane in the injector axis no asymmetry of the flow field can appear. This is the reason why the whole geometry model must be used.
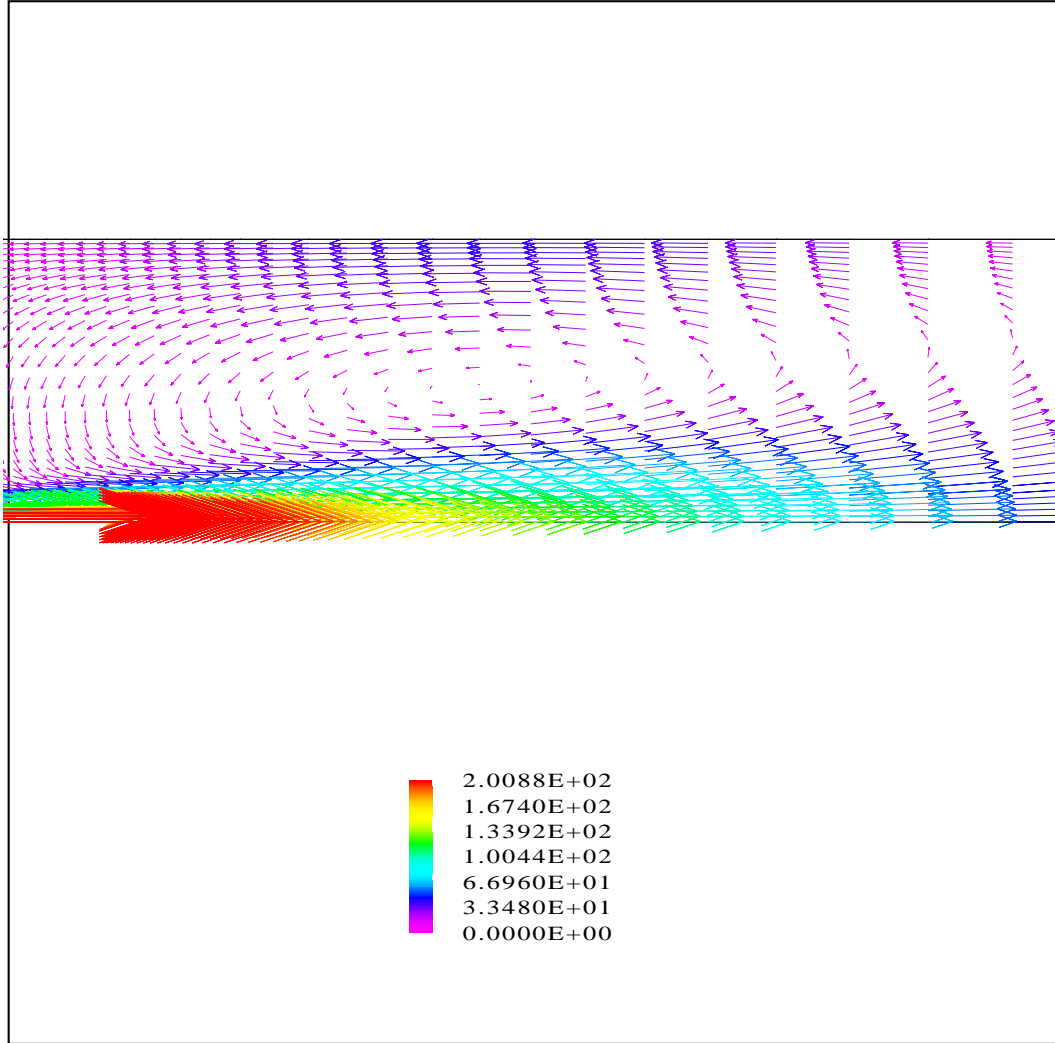
Figure 6.5: Eddy formation for half geometry, straight lines geometry, $\mu = 0,212$, colored with v_x velocity.

In the whole geometry model calculations were run for the design point pressure rise as well as for the pressure rises of $\Delta p = 0$, 550, 1500, 2000 und 2500 Pa. For these pressure rises, the obtained load coefficients are shown in table 6.3.

Table 6.3: Load coefficients for the straight lines geometry, whole geometry, incompressible fluid.

$\Delta p = 0\,Pa$	$\mu = 4,259$
$\Delta p = 550\,Pa$	$\mu = 3,719$
$\Delta p = 1000\,Pa$	$\mu = 3,106$
$\Delta p = 1500\,Pa$	$\mu = 2,348$
$\Delta p = 2000\,Pa$	$\mu = 1,350$
$\Delta p = 2500\,Pa$	$\mu = 0,286$

Again the load coefficient at the design point is lower than the one expected by the model of *Schlag*. For higher pressure rises the values obtained for the load coefficient μ are in the region of eddy formation and swinging jet.

Doing a comparison between the load coefficient of both geometries, the results seem to be the same, as shown in figure 6.6. However taking the pressure rise $\Delta p = 1500\,Pa$ with $\mu = 2,348$, the non-symmetrical flow field is shown in figure 6.7. In the upper part of the mixing duct a vortex can be seen clearly.
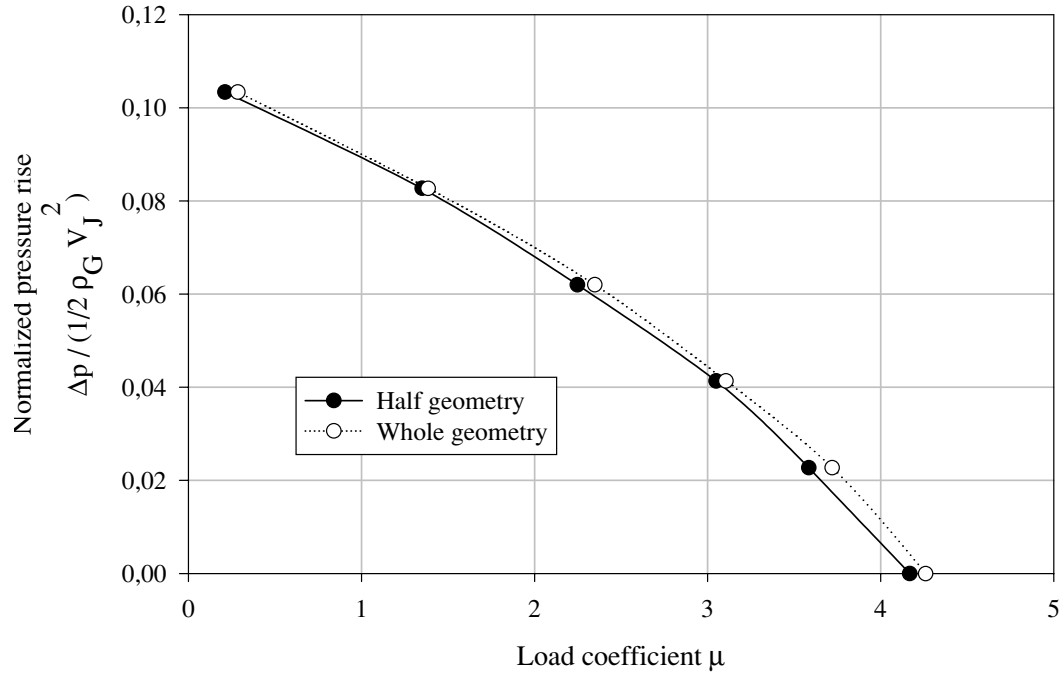
Figure 6.6: Comparison of load coefficients between half and whole geometry, straight lines, incompressible fluid.

Following the theory of *Curtet* [8] only asymmetries should appear but no oscillatory phenomenon for this load coefficient. A transient calculation has been made to check if the jet swings. Calculating the load coefficient for the last time steps, it can be concluded that this coefficient is constant as shown in figure 6.8.
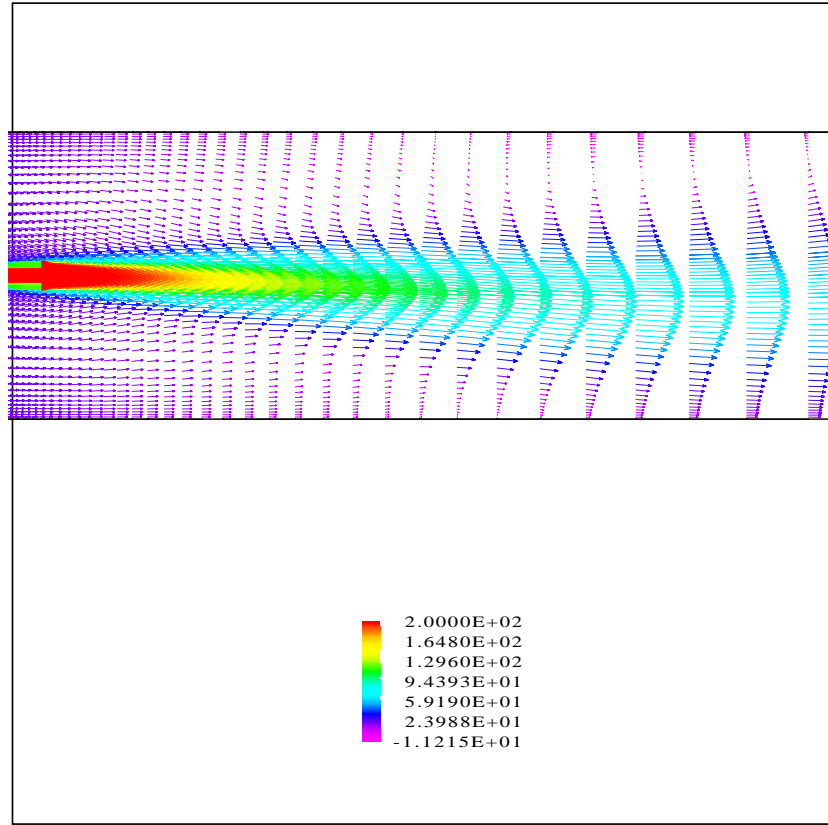
Figure 6.7: Non-symmetrical eddy formation for whole geometry with $\mu = 2,348$, incompressible fluid, colored with v_x velocity.
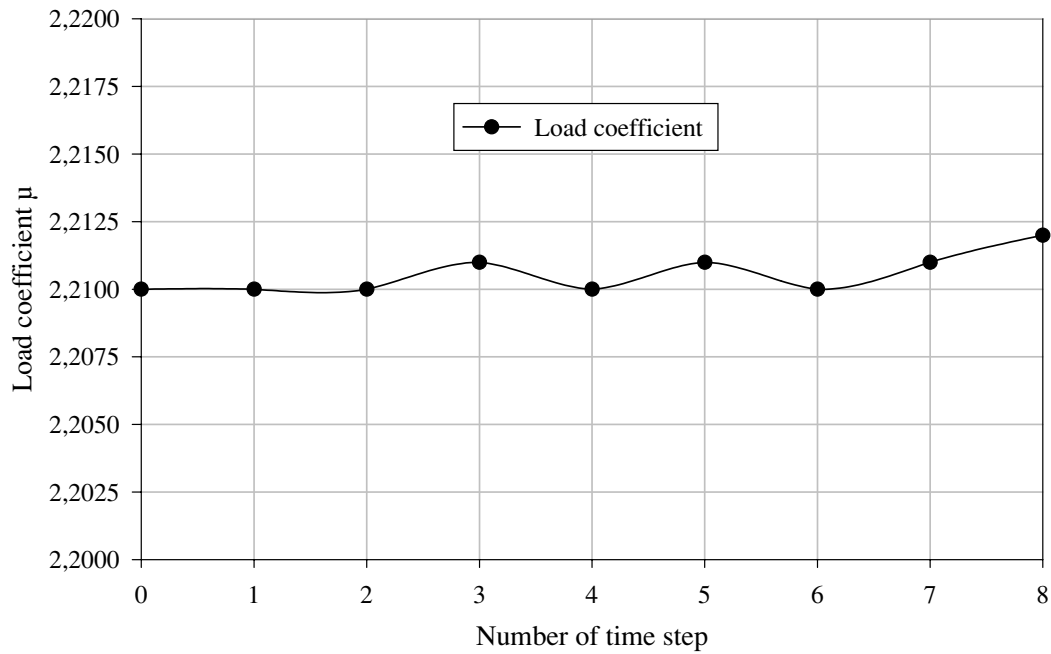
Figure 6.8: Instantaneous load coefficients, pressure rise $1500\,Pa$, incompressible fluid.

For a pressure rise $\Delta p = 2500\,Pa$ where the μ is low enough to have a swinging jet, the time period of the recirculating regions has been calculated with help of equations 3.9, 3.10 and 3.11.

The time period has a value of $T = 0,028\,s$ and is used in the transient calculation to obtain the periodical function of the load coefficient. An average value for the load coefficient can be calculated with these instantaneous values.

When doing a graph with the values of μ obtained in several time steps of the transient calculation for a pressure rise $\Delta p = 2500\,Pa$ the periodicity can be recognized in figure 6.9. The calculated time period is $0,0448\,s$, higher than the one given by *Curtet*.
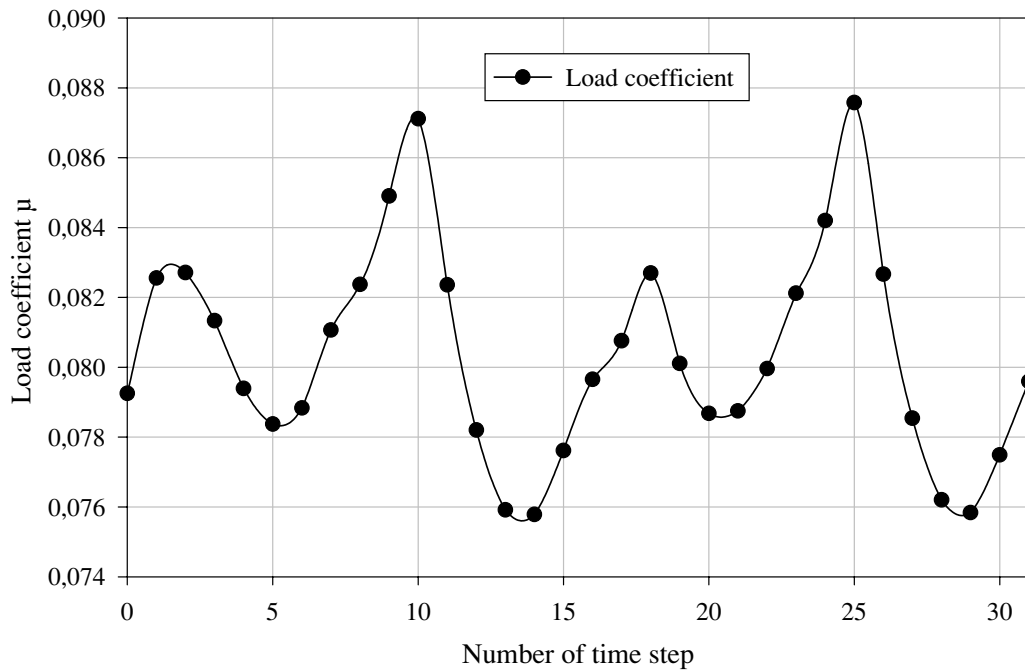
Figure 6.9: Variation of the load coefficient for $\Delta p = 2500\,Pa$, incompressible fluid.

The average value for the load coefficient of the swinging jet is in this case $\mu = 0,0804$.

It is also possible to show the instantaneous flow field along a time period. The changing flow field is shown in figures 6.10 to 6.15. It can be seen that there are time steps where the jet is bumping against the walls and time steps where the flow field is almost symmetric. The minimum and maximum discharges are reached in intermediate positions of the jet because of some transient effects in the movement of the fluid.
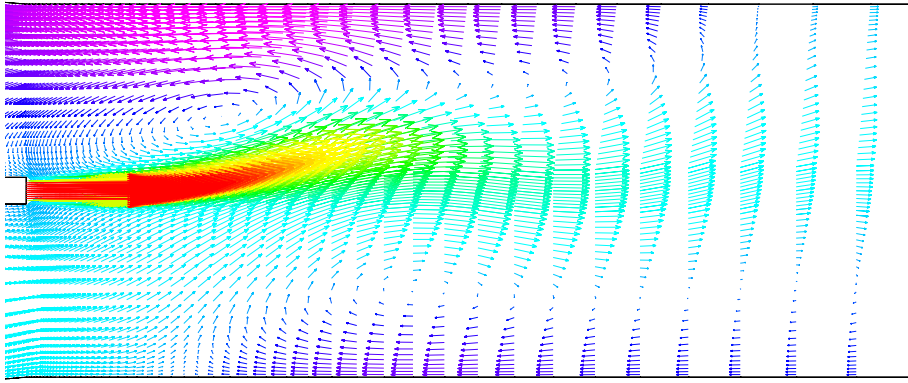
Figure 6.10: Velocity vector flow field in time step 10, incompressible fluid, colored with v_x velocity.
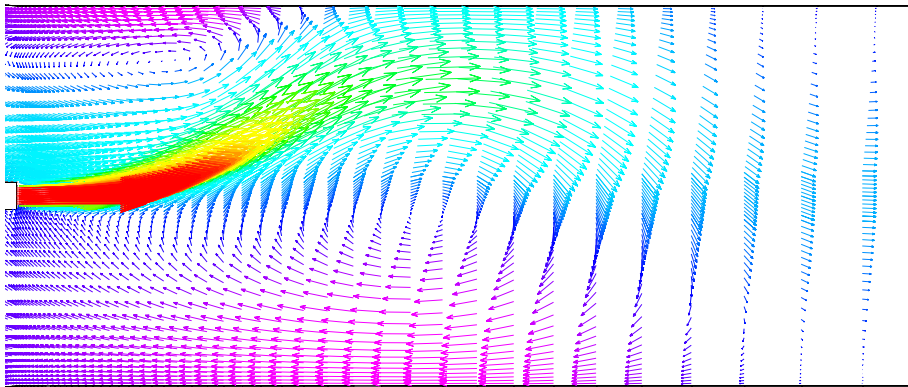
Figure 6.11: Velocity vector flow field in time step 14, incompressible fluid, colored with v_x velocity.
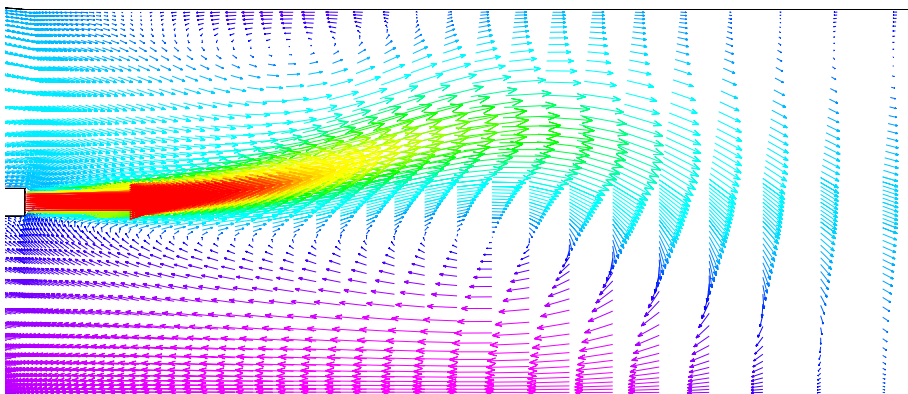
Figure 6.12: Velocity vector flow field in time step 16, incompressible fluid, colored with v_x velocity.
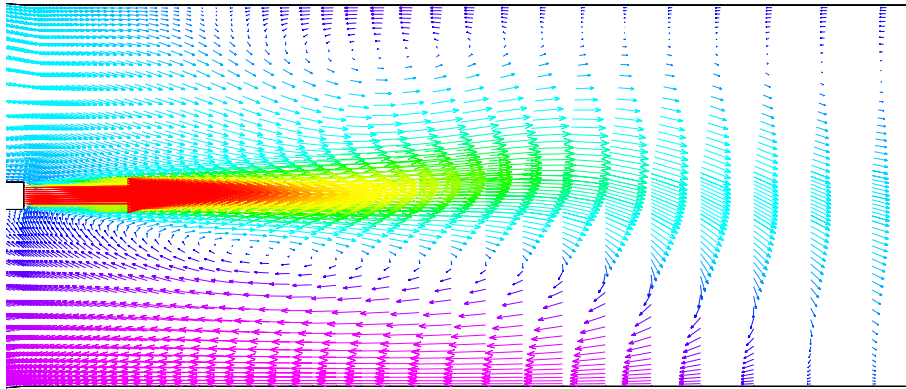
Figure 6.13: Velocity vector flow field in time step 17, incompressible fluid, colored with v_x velocity.
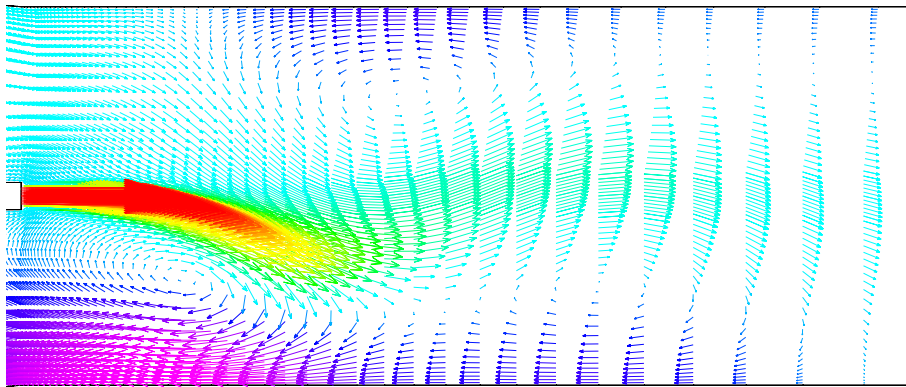
Figure 6.14: Velocity vector flow field in time step 18, incompressible fluid, colored with v_x velocity.

As can bee seen two vortices are present, one on the upper side and one on the lower side of the jet. The vortices change their size and position with time. In figure 6.14 even three vortices can be seen. The third vortex is formed when the jet divides the lower vortex into two parts.

$$
\begin{array}{rl}
\blacksquare & \text{2.0000E+02} \\
& \text{1.5436E+02} \\
& \text{1.0873E+02} \\
& \text{6.3093E+01} \\
& \text{1.7458E+01} \\
& \text{-2.8178E+01} \\
\blacksquare & \text{-7.3814E+01}
\end{array}
$$
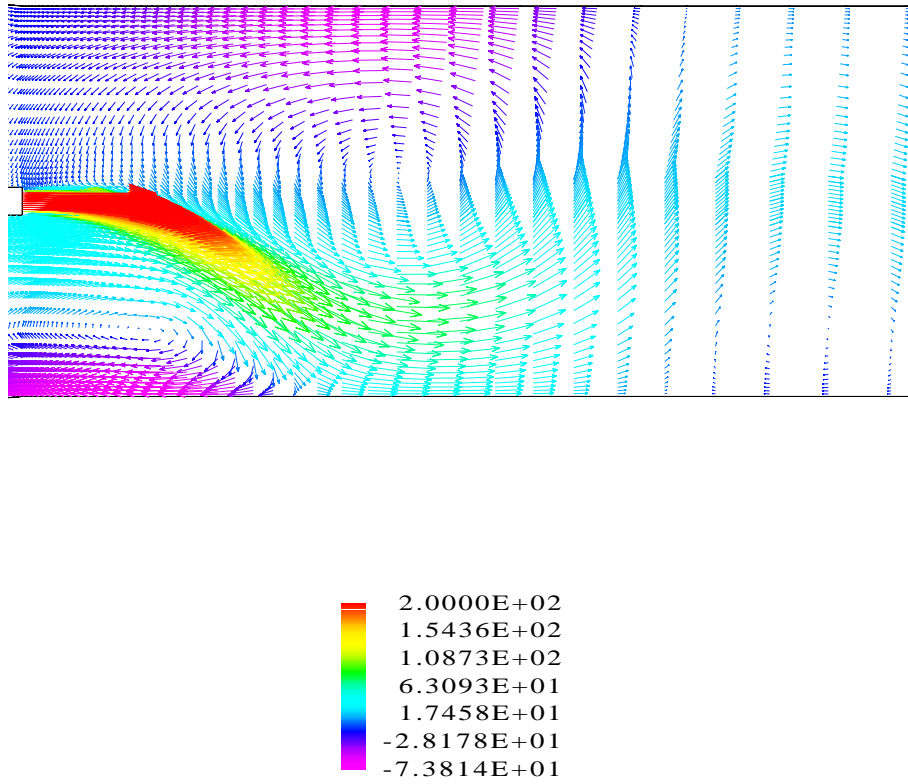
Figure 6.15: Velocity vector flow field in time step 21, incompressible fluid, colored with v_x velocity.

It is also of interest to see how the pressure rises along the injector axis. The pressure increases in order to obtain the desired pressure rise at the end of the diffuser. Figure 6.16 presents the change of the pressure along the symmetry axis for the design point both for the half geometry and for the whole geometry.
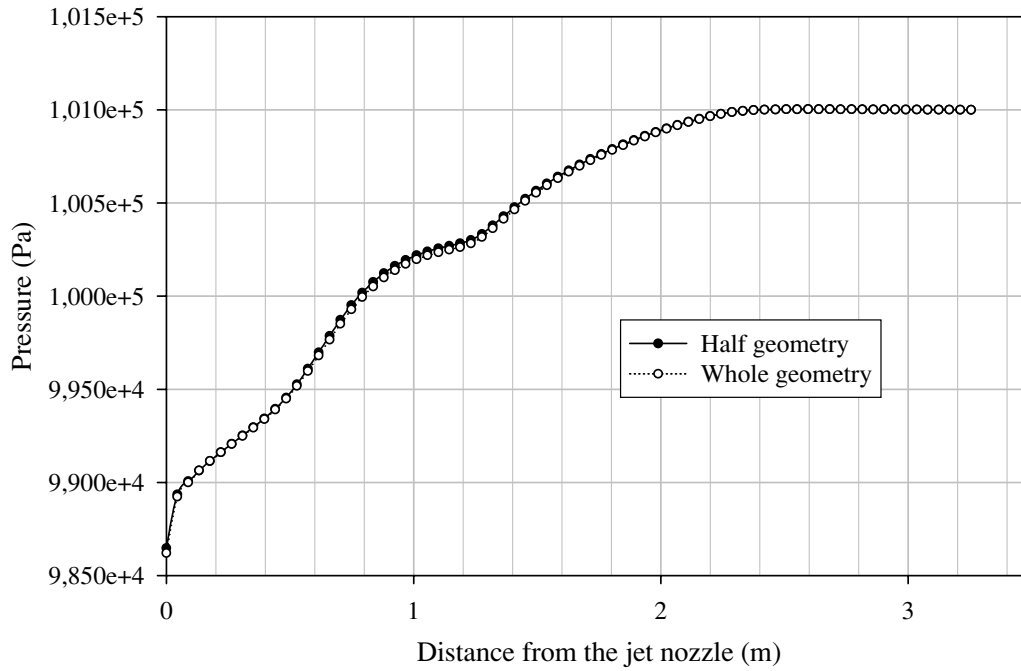
Figure 6.16: Pressure along the injector axis for incompressible fluid and straight lines geometry.

Both models seem to have the same pressure distribution along the injector axis. This is true from the point of view that for the design point there should not be any asymmetry in the flow field.

Some regions of the injector can be distinguished in figure 6.16. Figure 6.17 shows the velocity distribution for several planes along the injector axis. The minimum of the pressure is located at $x = 0\,m$. This minimum is coincident with the beginning of the jet where the maximum of kinetic energy exists. The pressure increases very fast in a short distance, caused by the sudden decceleration of the jet when entering the mixing duct, approximately at $x = 0,1\,m$. The increasing shear stress layer erases the potential core of the jet and the pressure increases at a constant rate, $x = 0,5\,m$. Once the potential core has disappeared, $x = 1\,m$, the pressure keeps rising while the shear stress region extends from the center to the walls. And finally, at the ending part of the mixing duct this shear stress region has been almost extended completely. Along the diffuser the rest of the remaining kinetic energy of the gases is used to rise the pressure. Furthermore, there is no pressure rise along the tail duct, which agrees with our requirements for the boundary conditions.
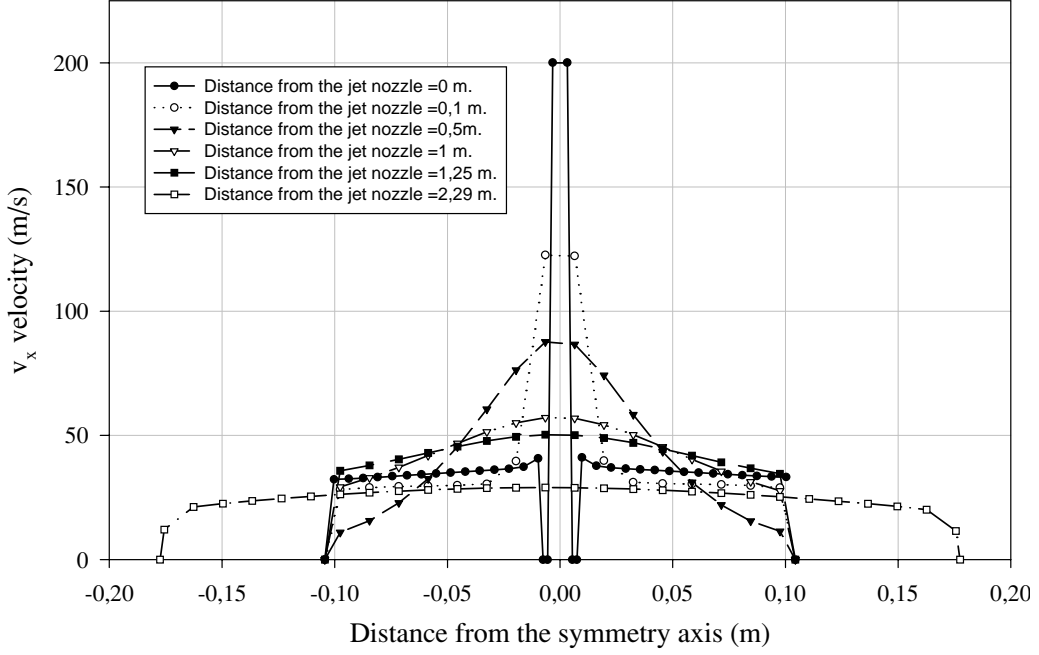
Figure 6.17: Velocity distribution at different distances from the jet nozzle for incompressible fluid and straight lines geometry.

As a consequence of the mixing out of the jet and the suction gases losses are created. To have an idea how big they are or how much work is extracted from the injector, the efficiency is calculated. The efficiency gives a ratio between the obtained exergy and the applied exergy.

The exergy is a measurement of the useful energy in the process, and is defined by *Fratzscher et al.* [6] as

$$\Delta e = \Delta h - T_u \, \Delta s. \tag{6.2}$$

Developing each member of equation 6.2

$$\Delta e = c_p \left(T - T_u \right) - T_u \, c_p \, ln \frac{T}{T_u} + R \, T_u \, ln \frac{p}{p_u} \tag{6.3}$$

is obtained, where c_p is the specific heat capacity at constant pressure. The subindex u indicates a measurement in the magnitudes in calm conditions which have been taken as $T_u = 15°C$ and $P_u = 100000 \, Pa$. P and T are the total pressure and total temperature, respectively.

To obtain the efficiency η following calculation is made,

$$\eta = \frac{e_{C_o} \left(\dot{m}_G + \dot{m}_J \right)}{\dot{m}_J \, e_{A_o} + \dot{m}_G \, e_{B_o}} = \frac{e_{C_o}}{e_{C_{o \, rev}}}, \tag{6.4}$$

where A_o indicates the total magnitude at the exit of the jet nozzle, B_o the total magnitude of the secondary flow at the entrance of the mixing duct, and C_o means the total magnitude of the mixture when the values are taken at the end of the diffuser.

The necessary magnitudes to obtain the exergy have been calculated by averaging the values of the pressure, velocity, density, temperature, velocity^2 and $\frac{p}{\rho}$ at the beginning of mixing duct for the jet and for the secondary flow, and at end of the diffuser for the mixture.

Applying equation 6.4 the efficiency achieved by the injector for the design case is equal to $\eta = 36,6\,\%$.

6.1.2.2   Injector with Curve Lines as Wall Shape

Starting the calculations with the half geometry model, it appears a symmetric problem with symmetric results. But it is already known this is not always true, especially in the case of low load coefficients.

Running a calculation for the design case, the obtained load coefficient is $\mu = 3,31$. This value is lower than the expected by the model of *Schlag*, although larger than the one for the injector with straight lines. With this μ and by figure 3.5 no eddies or asymmetries are expected. Checking the v_x velocity in figure 6.19 there are no negative values for it and the flow field is as supposed. Figure 6.18 and 6.19 show the high gradients in the velocity at the beginning of the mixing duct where the jet starts mixing with the gases from the environment.
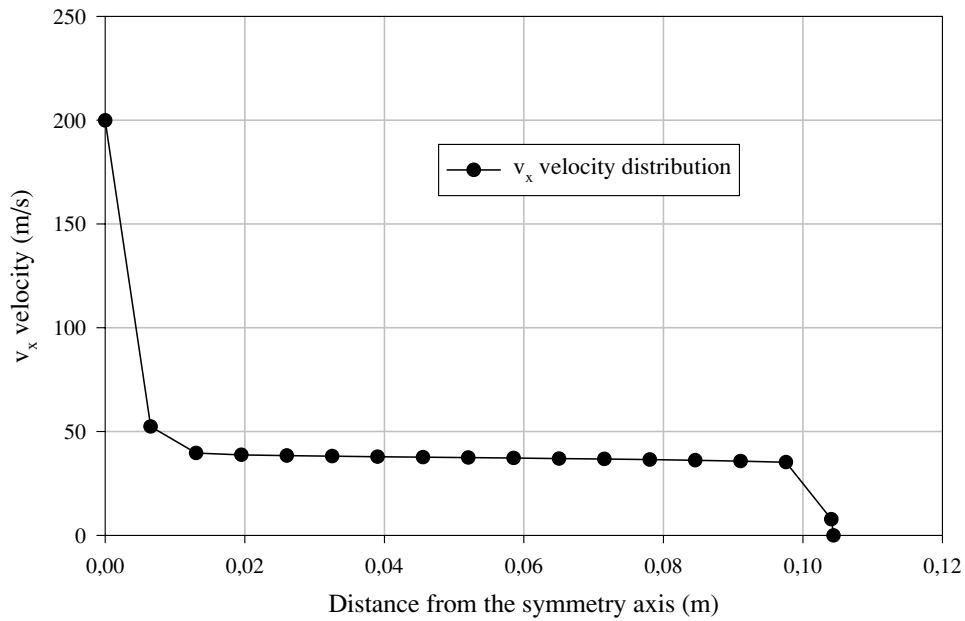
Figure 6.18: Interpolation of the values of v_x velocity at the beginning of the mixing duct.
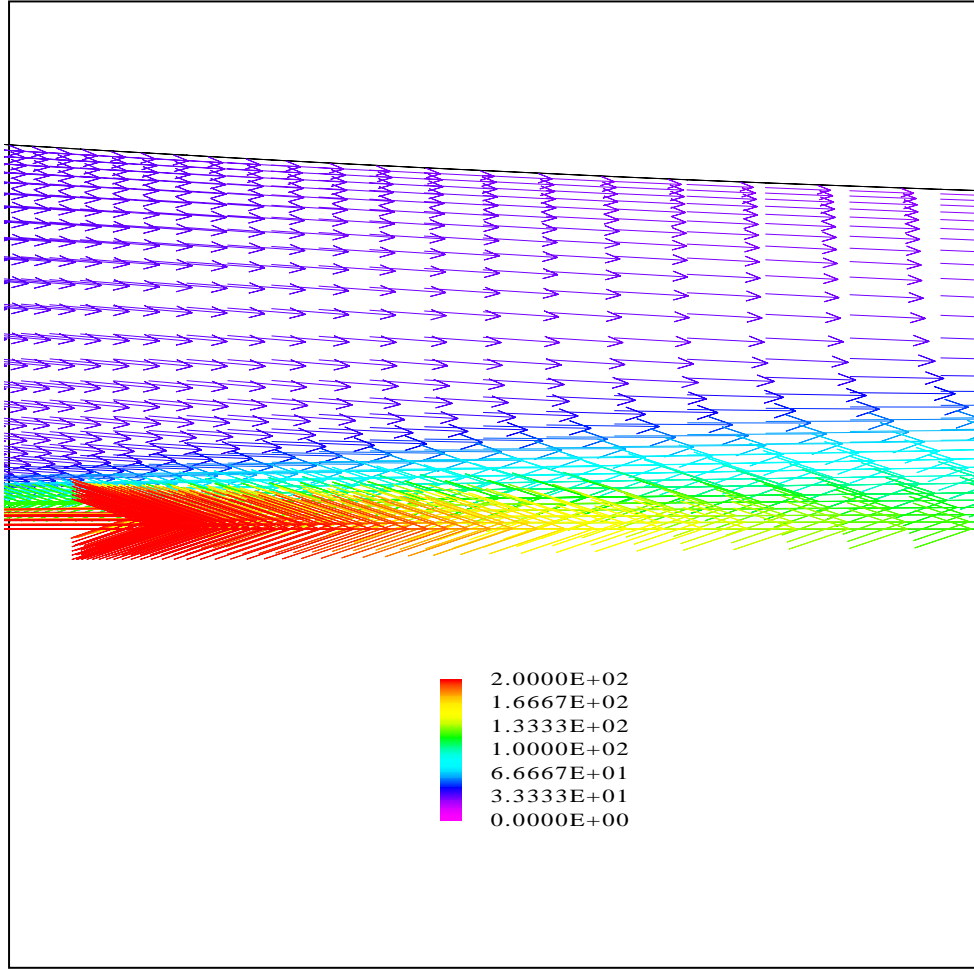
Figure 6.19: Velocity vector field at the beginning of the mixing duct, colored with v_x velocity.

The interpolation of the values of the v_x velocity at the end of the mixing duct and at the end of the diffuser are shown in figure 6.20.

The axial component of the velocity, v_x, can be considered as constant at the end the diffuser, but not at the end of the mixing duct. In fact, it is larger than in the case with the straight lines, but also the load coefficient is larger. A constant velocity profile over a wide range would be desiderable to obtain the maximum performance in the mixing duct.
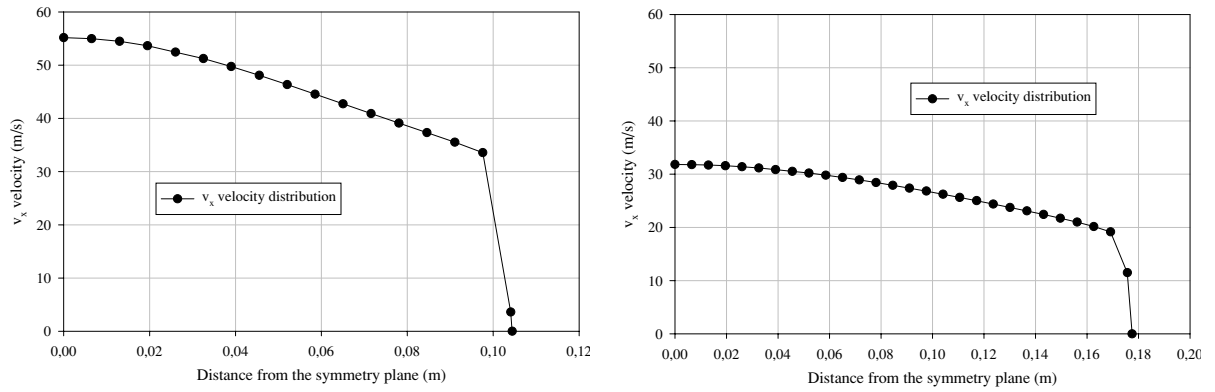
Interpolation of the v_x velocity at the end of the mixing duct.

Interpolation of the v_x velocity at the end of the diffuser.

Figure 6.20: Interpolation of the v_x velocity in the injector at the end of the mixing duct and at the end of the diffuser at the design point for half geometry.

Calculations have been done in order to analyze the off-design behaviour of the injector. The pressure rises are $\Delta p = 0$, 550, 1500, 2000, 2500 und $3000\,Pa$. With them, the load coefficients of table 6.4 have been obtained.

Table 6.4: Load coefficients for the curved line geometry cutted by the symmetry plane and incompressible fluid.

$\Delta p = 0\,Pa$	$\mu = 4,276$
$\Delta p = 550\,Pa$	$\mu = 3,765$
$\Delta p = 1000\,Pa$	$\mu = 3,310$
$\Delta p = 1500\,Pa$	$\mu = 2,664$
$\Delta p = 2000\,Pa$	$\mu = 1,969$
$\Delta p = 2500\,Pa$	$\mu = 1,162$
$\Delta p = 3000\,Pa$	$\mu = 0,185$

Load coefficients in the regions of eddy formation and swinging jet are obtained, but possible asymetries that could exist cannot be shown in this model. For instance for a pressure rise of $3000\,Pa$ the half geometry model only shows a big vortex without any asymmetries or movement of the jet as seen in figure 6.21. Then, these results are not valid for the whole range of pressure rises.

```
2.0089E+02
1.6029E+02
1.1968E+02
7.9076E+01
3.8471E+01
-2.1341E+00
-4.2739E+01
```
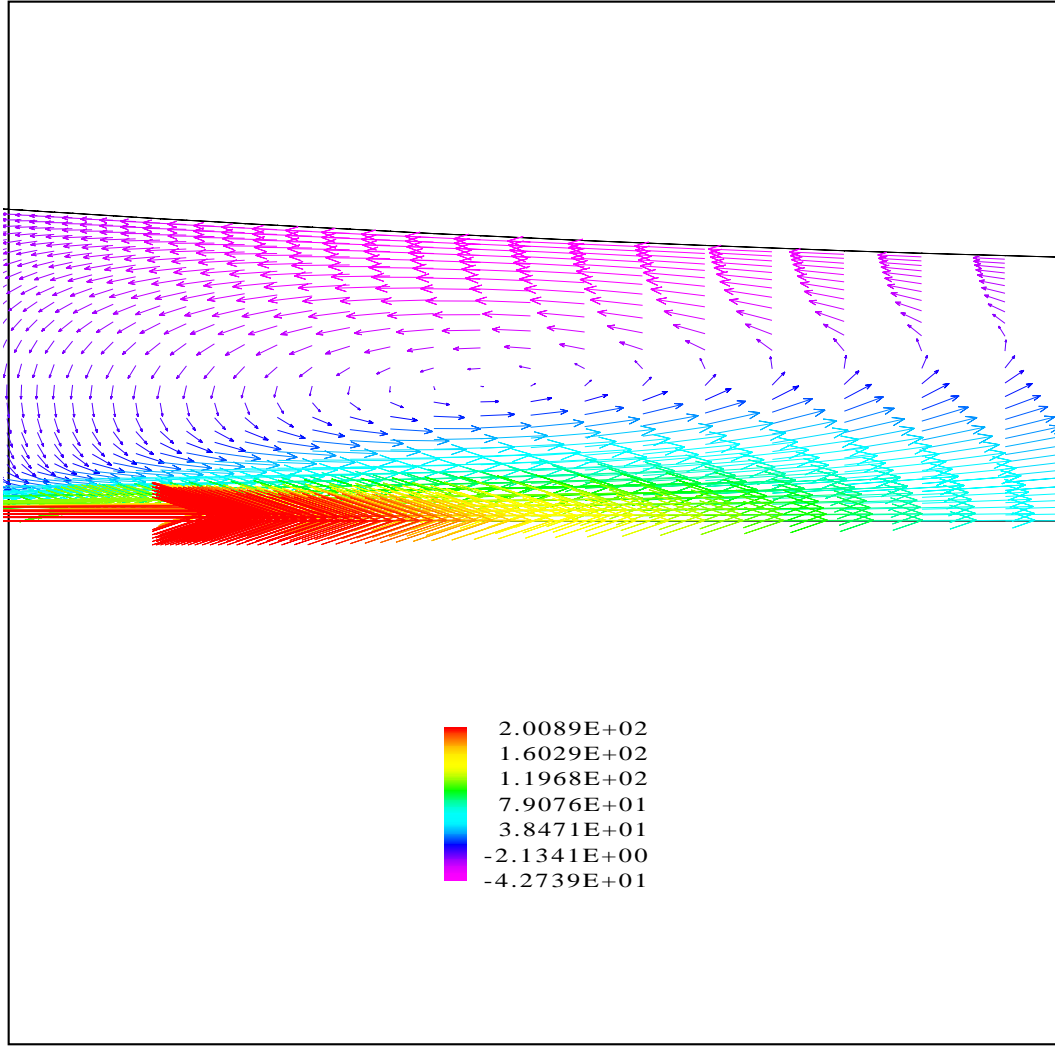
Figure 6.21: Eddy formation for half geometry curved line with $\mu = 0,185$, colored with v_x velocity.

As the results for the half geometry cannot be accepted in any operating point as valid, the whole geometry model was used to obtain the load coefficients for the pressure rises from $\Delta p = 0\,Pa$ to $3000\,Pa$. These coefficients are shown in table 6.5.

Table 6.5: Load coefficients for the curved line geometry and incompressible case.

$\Delta p = 0\,Pa$	$\mu = 4,306$
$\Delta p = 550\,Pa$	$\mu = 3,808$
$\Delta p = 1000\,Pa$	$\mu = 3,411$
$\Delta p = 1500\,Pa$	$\mu = 2,684$
$\Delta p = 2000\,Pa$	$\mu = 2,017$
$\Delta p = 2500\,Pa$	$\mu = 1,181$
$\Delta p = 3000\,Pa$	$\mu = -0,0296$

Again there are load coefficients for the cases of high pressure rises which are in the region of a swinging jet. Doing a graph with the results of the load coefficients for the half and for the whole geometry figure 6.22 is obtained.
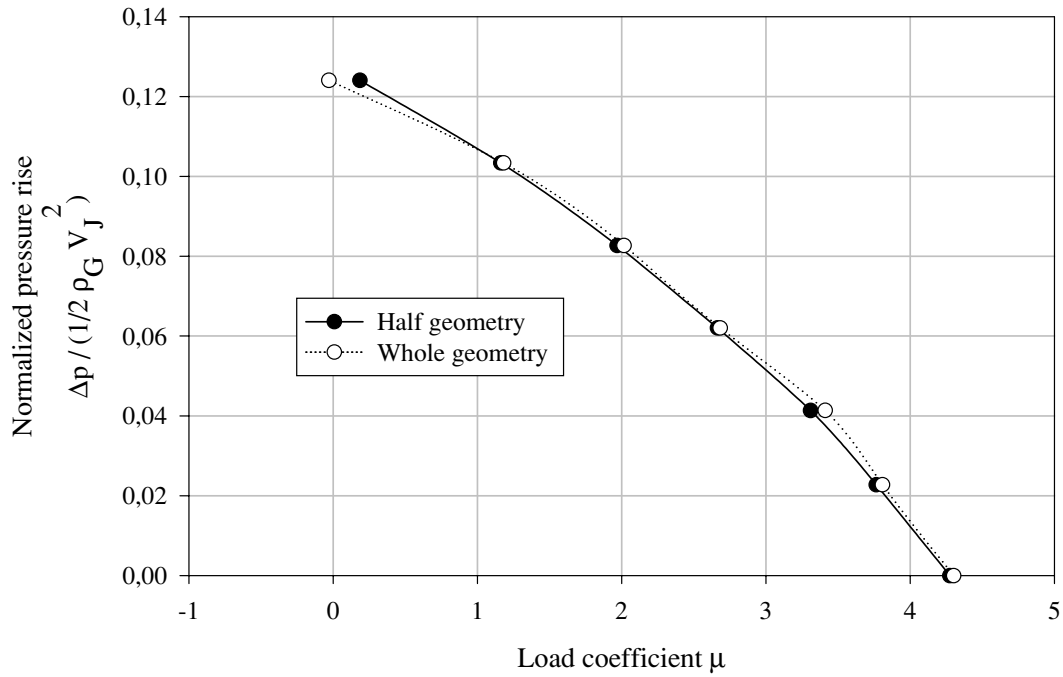
Figure 6.22: Comparison of load coefficients between half and whole geometry, curved lines, incompressible fluid.

Here the results are not the same for the half geometry model and for the whole geometry model at high pressure rises. For the half geometry a load coefficient of $\mu = 0,185$ was obtained for the case of $\Delta p = 3000\,Pa$. In the whole geometry the load coefficient takes a value of $\mu = -0,0296$ for the same pressure rise. Both of them are not reliable because they lie in the swinging jet area, so that, a transient calculation is required.

Furthermore, the negative load coefficient means that the pressure at the end of the injector is higher than the one the injector can come over and there is a reversible flow. When a transient calculation was tried, the results were incongruent due to the reversible flow. To make a transient calculation a lower pressure rise $\Delta p = 2750\,Pa$ was chosen. This pressure rise gives a low value for the load coefficient in the steady state calculation: $\mu = 0,5489$. The transient calculation with the oscillation of the load coefficient is reflected in figure 6.23.

The average value for the load coefficient is $\mu = 0,5547$.

It is again of interest to check how the pressure changes along the injector axis, for both geometries and for the design case. Figure 6.24 shows both cases.
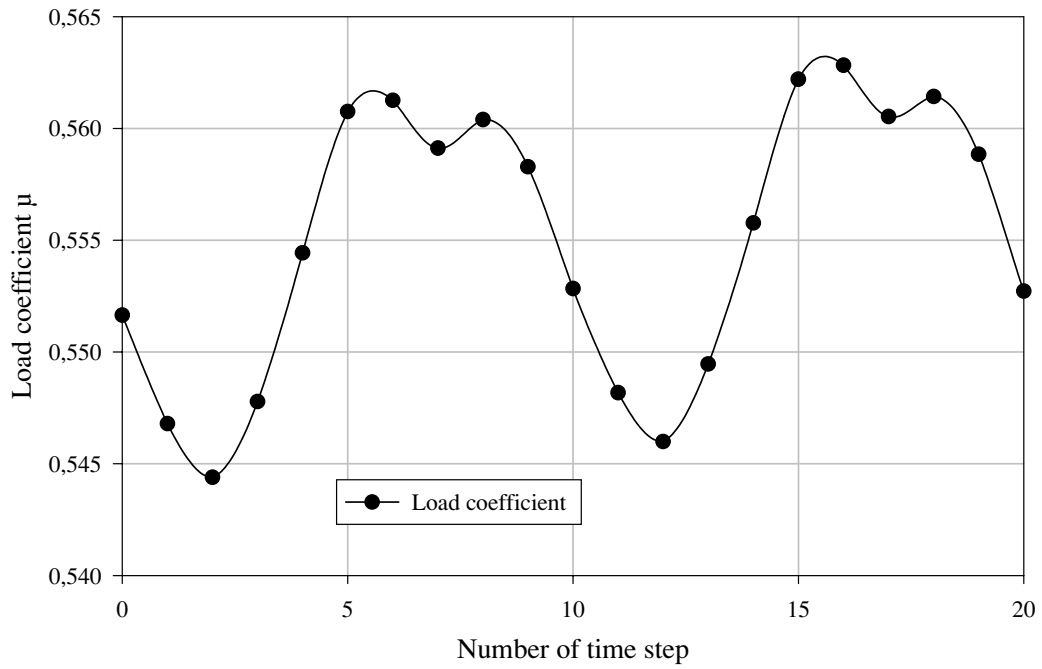
Figure 6.23: Instantaneous load coefficient for $\Delta p = 2750\,Pa$, incompressible fluid and curved lines geometry.
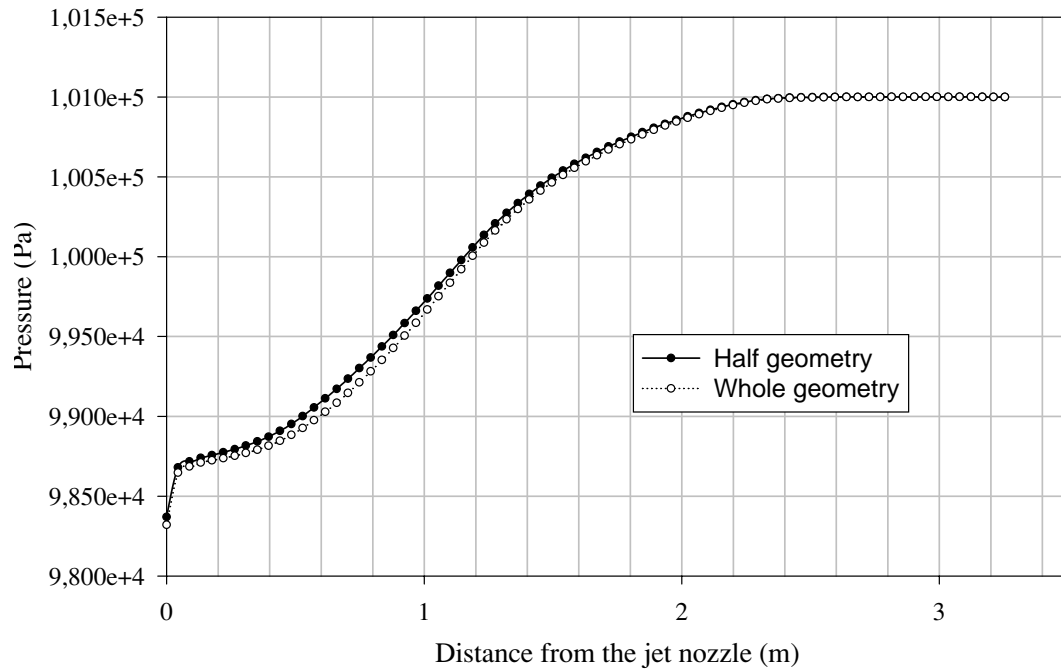
Figure 6.24: Pressure along the injector axis for incompressible fluid and curved lines geometry.

Again the absence of asymmetries in the design point makes both profiles almost identical.

At the beginning of the mixing duct, very close to the jet nozzle, the pressure increases very fast as the jet looses kinetic energy mixing with the gases from the environment. Afterwards the pressure keeps almost constant until nearly the half of the mixing duct, $x = 0,5\,m$. This occurs because of the shape of the mixing duct. The cross-section decreases and the gases are accelerated until the half of its length. While the gases are being accelerated, there is no conversion of kinetic energy into static pressure.

The pressure profile is lower and smoother in general than in the constant width mixing duct. However, the pressure that could be overcome is higher due to the larger velocity of the mixture at the end of the diffuser.

The velocity distribution at the same distances from the jet nozzle as in the straight lines geometry is shown in figure 6.25. In general, the velocities are higher than in the case of constant width mixing duct as it was expected, especially for the planes which distance from the jet nozzle is $0,5\,m$ and $1\,m$. These planes have the largest differences in pressure rise because they are situated in the region of the converging duct.
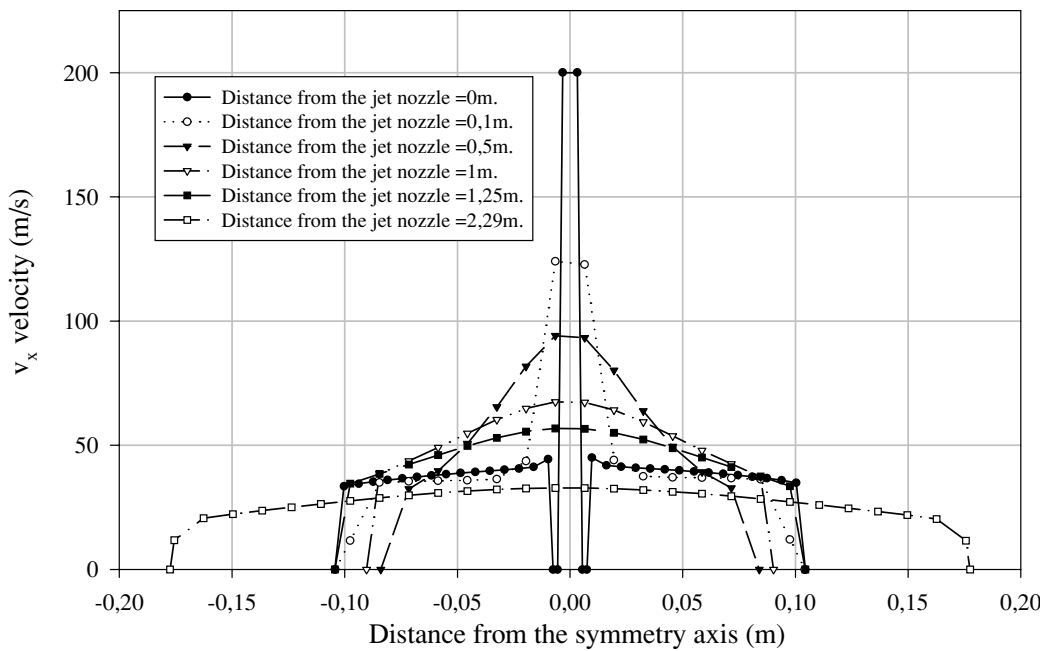
Figure 6.25: Velocity distribution at different distances from the jet nozzle for incompressible fluid and curved lines geometry.

The efficiencies for the curved lines case are expected to be higher than in the straight lines case. This phenomenon can be understood looking at the shape of the mixing duct. The energy lost in the mixing process is the work done by the turbulent stresses. Decreasing the velocity differential between the primary and secondary flows can reduce this work. A positive pressure gradient, as in the constant width mixing duct, decreases the velocity of the secondary flow more in proportion to the velocity of the jet, causing an adverse effect on the velocity difference. Conversely, a negative pressure gradient as in the curved lines geometry,

supports an equalizing effect on the mixing process and so reduces the work done by the turbulent shear stresses.

The efficiency for the design case is in this geometry equal to $42,3\,\%$. Comparing with the case of straight lines this is $16,6\,\%$ bigger.

6.2 Compressible Fluid

The cases before are treated with the supposition of incompressible fluid, due to the fact that *Schlag* considers this hypotheses to build up his model. But in the problem considered here, the jet comes out with a velocity of $v_J = 200^{m}/_{s}$. If the Mach number is calculated according to equation 2.81, the result is $Ma = 0,6$. For $Ma \geq 0,4$, it is said in [14] that the effects of the compressibility must be taken into account.

6.2.1 CFD Model for Compressible Fluid

The calculations are done for the same environmental conditions and for the same pressures at the outlet as in the cases before, but with the consideration of compressible fluid.

Both for the case with the constant width mixing duct and for the case with the circle as wall shape the same dimensions in the geometry are used. If it is desired to calculate a new geometry for a compressible fluid, not only the equations of motion but also thermodynamical equations must be applied. The application of thermodynamical equations makes the model more complicated than the one given by *Schlag*.

6.2.1.1 Injector with Straight Lines

Having run calculations for the pressure range from $\Delta p = 0\,Pa$ to $2500\,Pa$ the load coefficients of table 6.6 were obtained for the half geometry and the ones of table 6.7 for the whole geometry.

Table 6.6: Load coefficients for the straight lines geometry cutted by the symmetry plane and compressible fluid.

$\Delta p = 0\,Pa$	$\mu = 3,4282$
$\Delta p = 550\,Pa$	$\mu = 3,0152$
$\Delta p = 1000\,Pa$	$\mu = 2,5403$
$\Delta p = 1500\,Pa$	$\mu = 1,9093$
$\Delta p = 2000\,Pa$	$\mu = 1,1110$
$\Delta p = 2500\,Pa$	$\mu = 0,0316$

Table 6.7: Load coefficients for the straight lines geometry and compressible fluid.

$\Delta p = 0$ Pa	$\mu = 3,5399$
$\Delta p = 550$ Pa	$\mu = 3,0266$
$\Delta p = 1000$ Pa	$\mu = 2,5951$
$\Delta p = 1500$ Pa	$\mu = 1,9192$
$\Delta p = 2000$ Pa	$\mu = 1,1675$
$\Delta p = 2500$ Pa	$\mu = 0,4266$
$\Delta p = 3000$ Pa	$\mu = -0,33$

The data of both tables are graphed in figure 6.26. When the pressure at the outlet is high the load coefficients are much different. It can be affirmed without seeing the figures of the flow field that the flow is not equal in both cases for the same pressure conditions. This means that asymmetries appear.
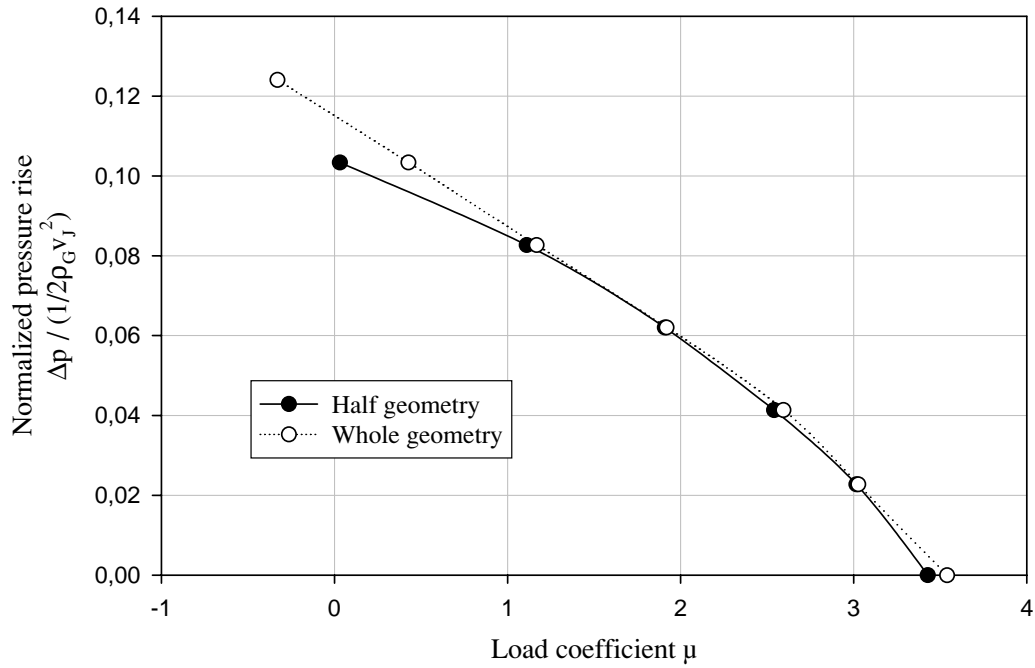
Figure 6.26: Comparison of load coefficients for the compressible case with straight lines geometry.
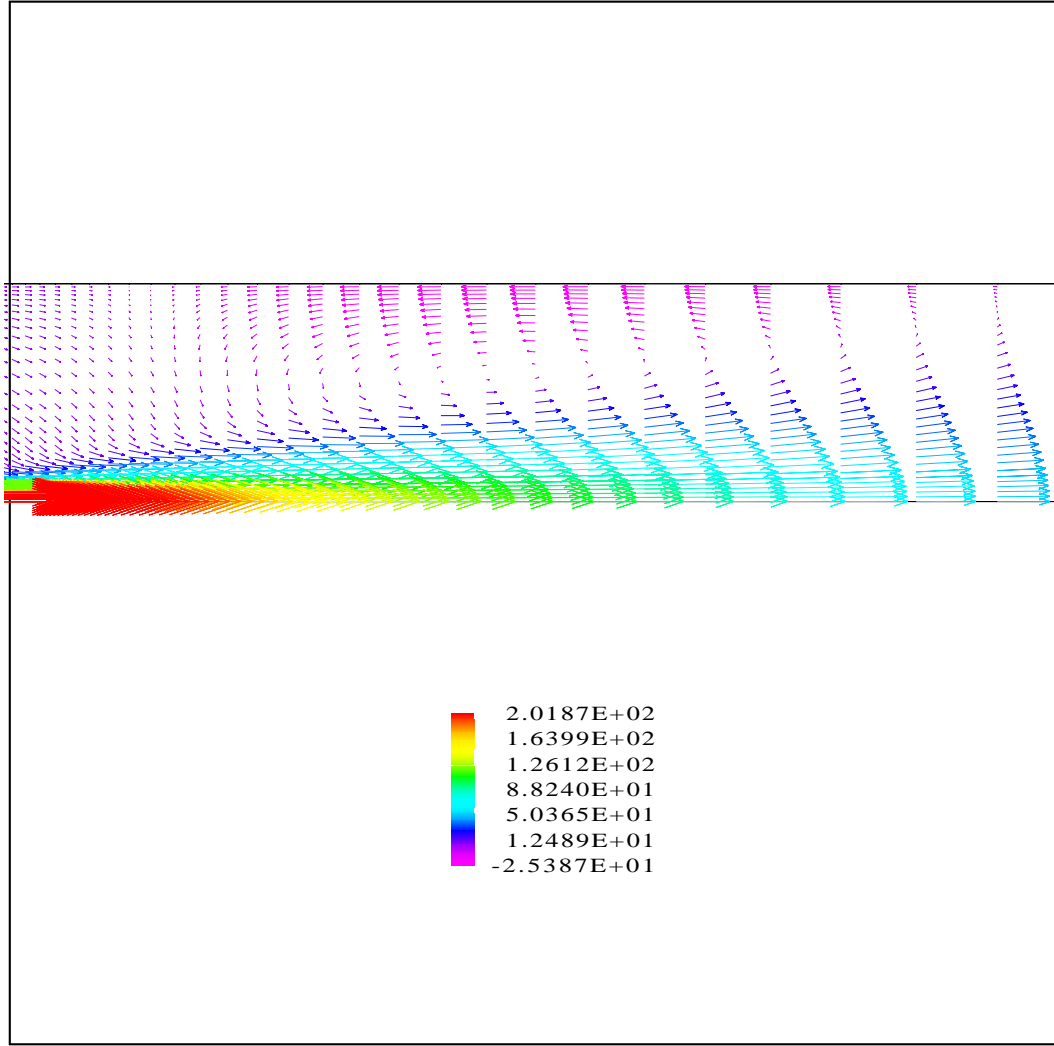
Figure 6.27: Velocity vector field for the half geometry model with $\Delta p = 2000\,Pa$, colored with v_x velocity.

Figures 6.27 and 6.28 show the flow field of the half geometry model and the whole geometry model for the pressure rise $\Delta p = 2000\,Pa$, respectively. In the figure representing the half geometry model, there are no asymmetries in the flow field. On the contrary, the figure representing the whole geometry shows an asymmetry of the flow field.

The difference between load coefficients can also be justified by the fact of having done only a steady state calculation. For the case of $\Delta p = 2500\,Pa$, the load coefficient is in the region of a swinging jet. Applying the condition of transient flow to this pressure rise the load coefficients change with time as shown in figure 6.29.
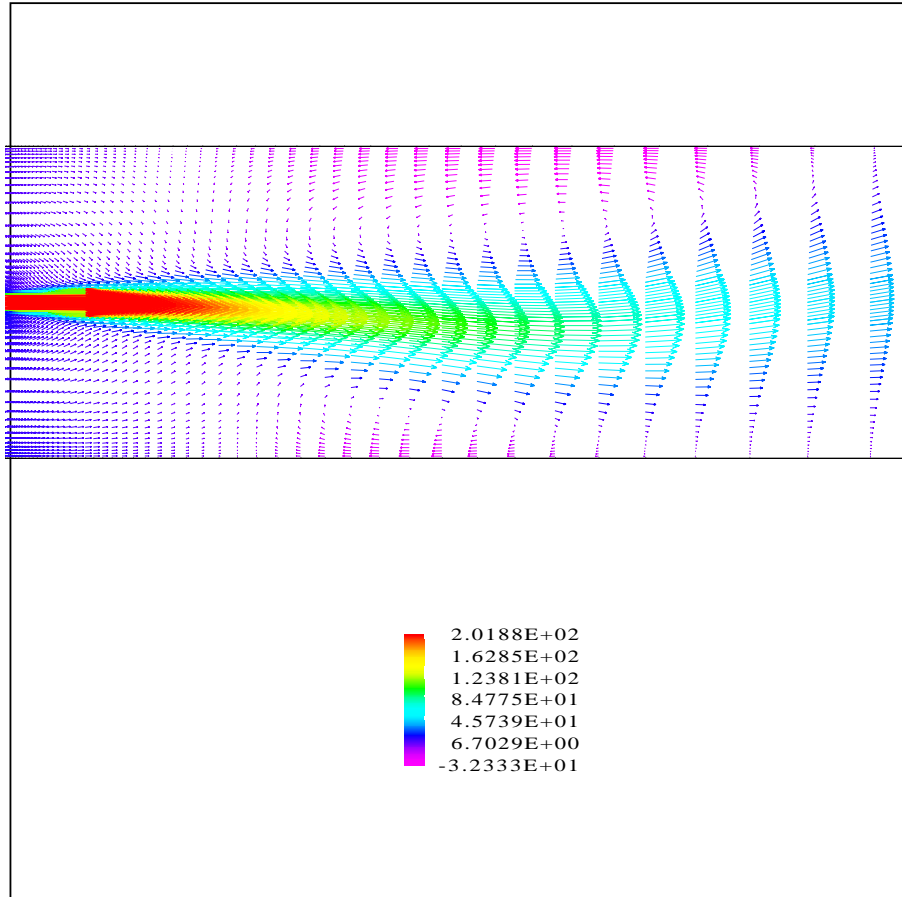
Figure 6.28: Velocity vector field for the whole geometry model with $\Delta p = 2000\,Pa$, colored with v_x velocity.
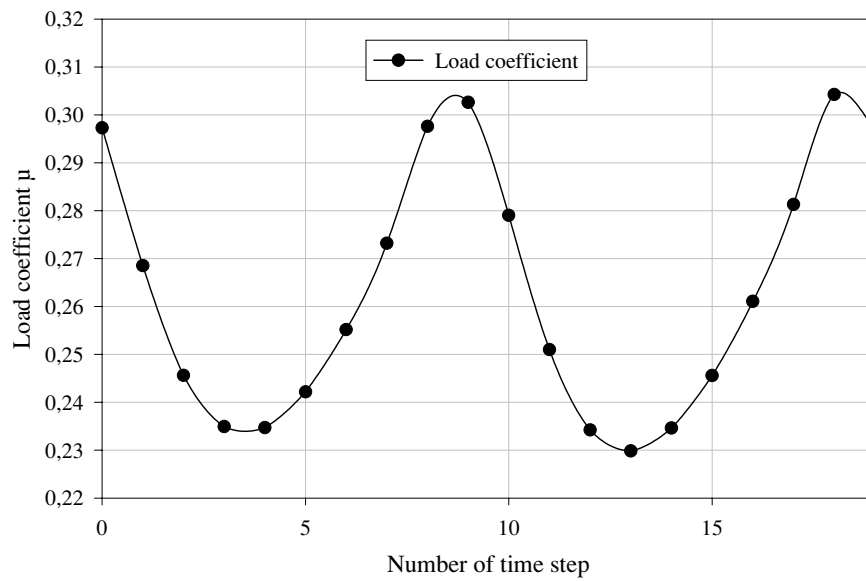
Figure 6.29: Instantaneous load coefficients for $\Delta p = 2500\,Pa$, compressible fluid and straight lines geometry.

The average value for the load coefficient is equal to $\mu = 0,2635$, lower than the one reflected in the steady state calculation.

Figure 6.30 depicts a comparison between the load coefficients of the incompressible case and those of the compressible case. The characteristic curve of the compressible case is much steeper than the one of the incompressible case.

For the incompressible case the jet and the secondary flow densities are taken as constant all along the injector. However, these densities change in the compressible case. Taking arbitrarily the design case, $\Delta p = 1000\,Pa$, the values obtained for the density and for the velocity in the jet and in the secondary flow show why the load coefficients are lower for a compressible fluid.
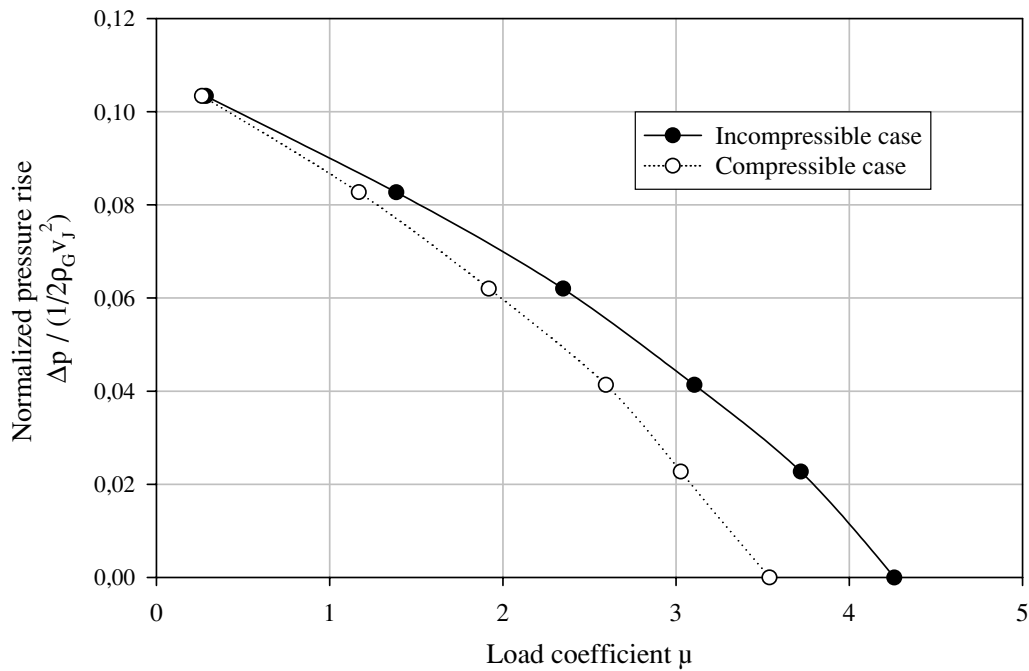
Figure 6.30: Comparison between the load coefficients for the incompressible and for the compressible case for the straight lines geometry.

Table 6.8 is obtained by interpolating the values of the density and the velocity in a plane at the entrance of the mixing duct.

Table 6.8: Comparison between the incompressible and compressible case, straight lines geometry.

Incompressible	Compressible
$\rho_J = 1,210\,{}^{kg}/{}_{m^3}$	$\rho_J = 1,223\,{}^{kg}/{}_{m^3}$
$v_J = 181,6121\,{}^{m}/{}_{s}$	$v_J = 181,6121\,{}^{m}/{}_{s}$
$\rho_G = 1,21\,{}^{kg}/{}_{m^3}$	$\rho_G = 1,187\,{}^{kg}/{}_{m^3}$
$v_G = 34,38\,{}^{m}/{}_{s}$	$v_G = 30,07\,{}^{m}/{}_{s}$

With the values of table 6.8, the mass flow $\dot{m}_i$ through the inlets can be calculated with

$$\dot{m}_i = \rho_i \, v_i \, A_i. \tag{6.5}$$

Applying this equation, the values obtained for the mass flow are shown in table 6.9.

Table 6.9: Comparison between the mass flow in the incompressible and compressible case, straight lines geometry.

Incompressible	Compressible
$\dot{m}_J = 2,42^{kg}/_s$	$\dot{m}_J = 2,44^{kg}/_s$
$\dot{m}_G = 8,07^{kg}/_s$	$\dot{m}_G = 6,92^{kg}/_s$

Applying the definition of load coefficient, equation 4.5, the load coefficient for the compressible case is lower.

Furthermore, being the density of the secondary flow smaller, it is easier for the jet to penetrate into this stream. Due to the decrease of the density, the mass flow suctioned is also smaller as it was reflected in table 6.9. With these two reasons it can be said that the mixing process is sooner completed. So that, the velocity profile at the end of the mixing duct is more uniform and closer to a constant profile than in the incompresible case. At the end of the diffuser both profiles are very close and considering that the discharge is smaller now, it can be said they are almost identical. Both cases are shown in figure 6.31.
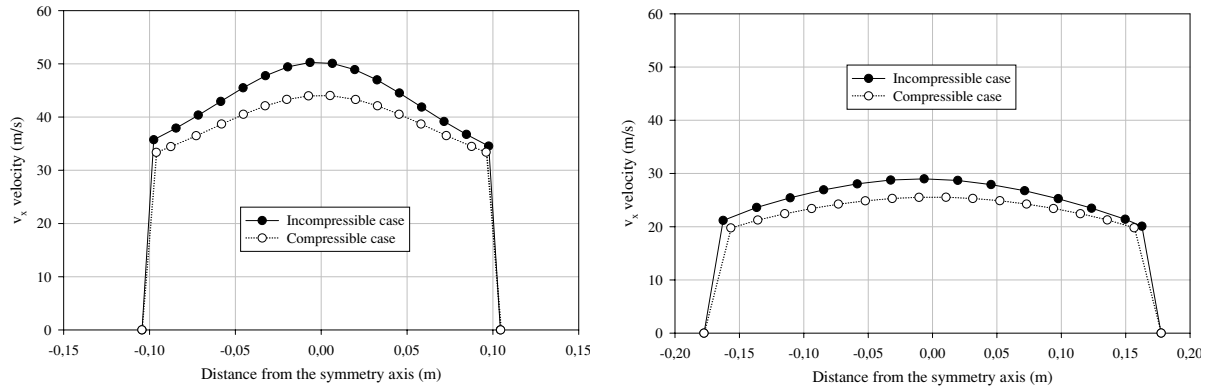
Interpolation of the v_x velocities at the end of the mixing duct.

Interpolation of the v_x velocities at the end of the diffuser.

Figure 6.31: Comparison between the v_x velocities both for incompressible and compressible fluid.

The pressure distribution along the injector axis will also differ due to compressibility. Figure 6.32 shows how a more uniform and lower velocity at the end of the mixing duct results in a higher pressure at the end of the mixing duct.
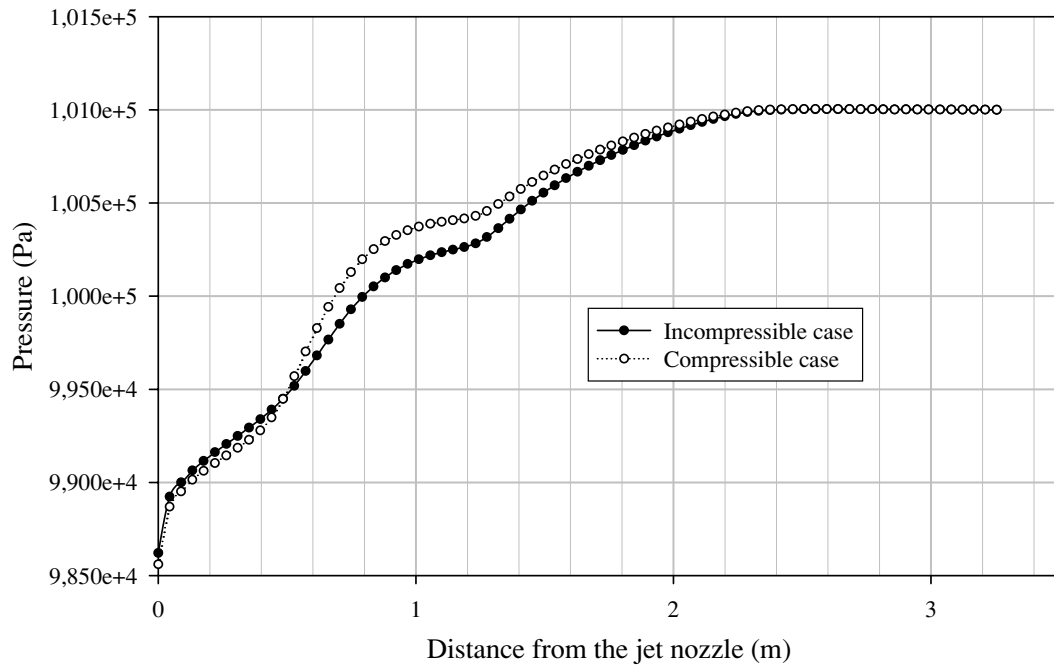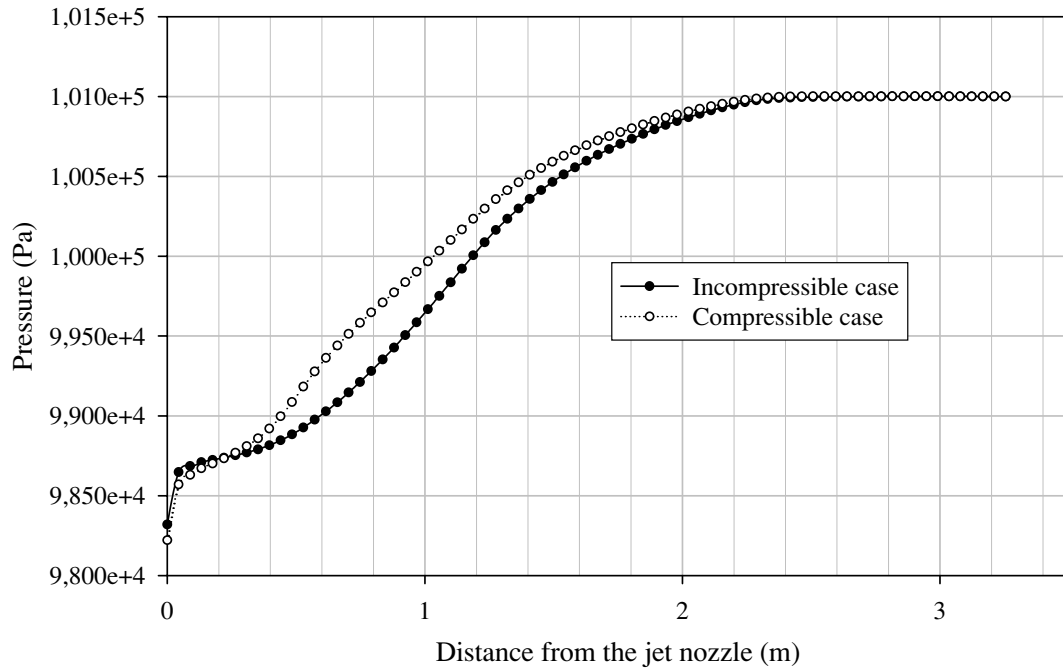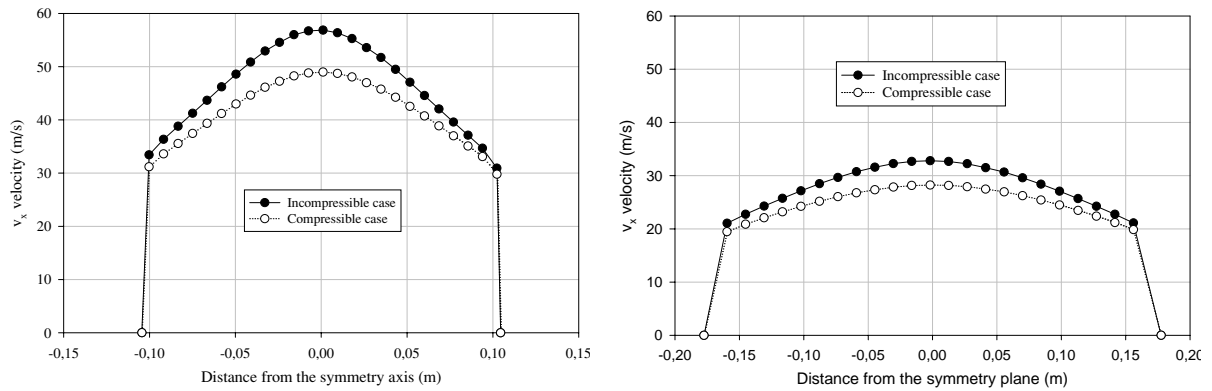
Figure 6.32: Comparison between the pressure distribution along the injector axis for compressible and incompressible fluid for the straight lines geometry.

The efficiencies have been calculated for the whole pressure range and are shown in figure 6.33.
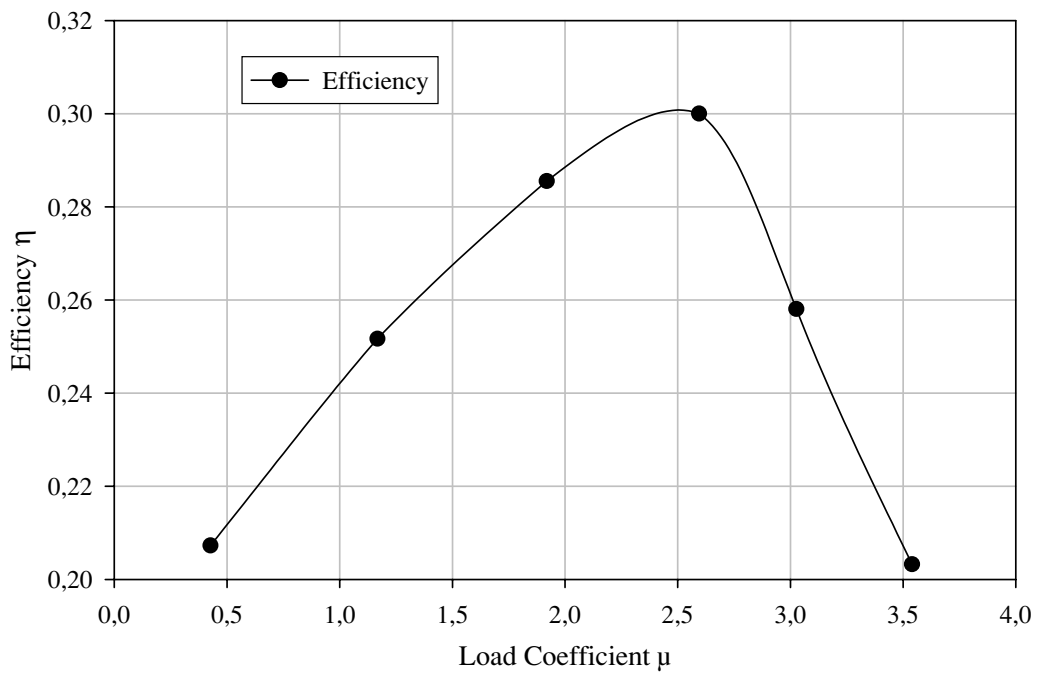
Figure 6.33: Efficiencies of the straight lines geometry, compressible fluid.

For the design case the efficiency is $17,4\,\%$ lower than that of the incompressible case, $\eta_{comp} = 30,0\,\% < \eta_{incomp} = 36,3\,\%$. The mass flow of the secondary flow is smaller in the compressible case and so the injector efficiency is also lower.

The maximum efficiency lies in the region where the vortices begin to appear, near to a $\mu = 2,5$. At this point, the presence of vortices generates gains in the injector due to the suppression of adverse static gradients to complete the mixing process [9]. This gain offsets the additional energy required to form the vortices. Larger vortices requires more energy and give rise to a fall in the efficiency. For load coefficients larger than the one of the design case, the increase of the total energy is smaller than the energy required to maintain the vortices. Therefore the efficiency for these cases will decrease.

6.2.1.2   Injector with a Circle as a Wall Shape

Doing the same experience for the curve line profile, the results are similar to the comparisons made for the incompressible case. Table 6.10 shows the load coefficients for the half geometry and table 6.11 shows them for the whole geometry.

Table 6.10: Load coefficients for the curved line geometry cutted by the symmetry plane and compressible fluid.

$\Delta p = 0$ Pa	$\mu = 3,6256$
$\Delta p = 550$ Pa	$\mu = 3,2074$
$\Delta p = 1000$ Pa	$\mu = 2,8384$
$\Delta p = 1500$ Pa	$\mu = 2,3025$
$\Delta p = 2000$ Pa	$\mu = 1,7450$
$\Delta p = 2500$ Pa	$\mu = 1,0546$

Table 6.11: Load coefficients for the curved line geometry and compressible fluid.

$\Delta p = 0$ Pa	$\mu = 3,8369$
$\Delta p = 550$ Pa	$\mu = 3,3610$
$\Delta p = 1000$ Pa	$\mu = 2,8193$
$\Delta p = 1500$ Pa	$\mu = 2,4005$
$\Delta p = 2000$ Pa	$\mu = 1,7737$
$\Delta p = 2500$ Pa	$\mu = 1,0048$
$\Delta p = 3000$ Pa	$\mu = $ -0,0167

Figure 6.34 displays both data.
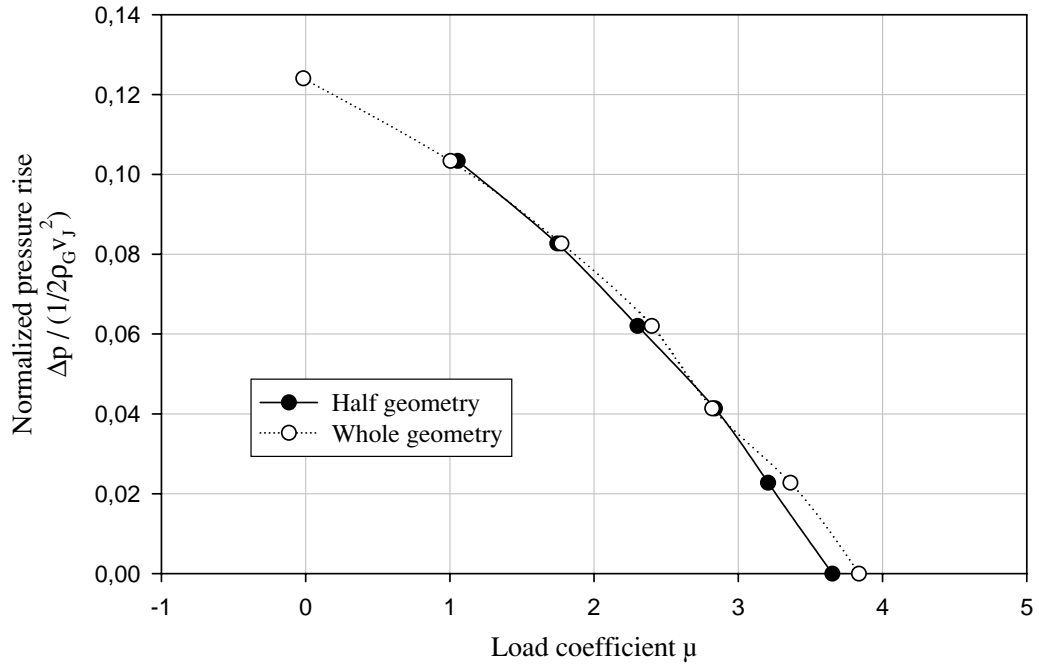
Figure 6.34: Comparison of the load coefficients of the curved lines geometry, compressible fluid.

The appearance of asymmetries at high pressures cannot bee seen so clearly as in the straight lines geometry, but it was previously demonstrated that at low load coefficients there are unequal extended vortices at both sides of the symmetry plane.

Figure 6.35 is obtained by doing a transient calculation with a pressure rise $\Delta p = 2500\,Pa$. This figure exhibits the instantaneous load coefficient versus time step number. The mean value of the load coefficient is $\mu = 1,1113$.
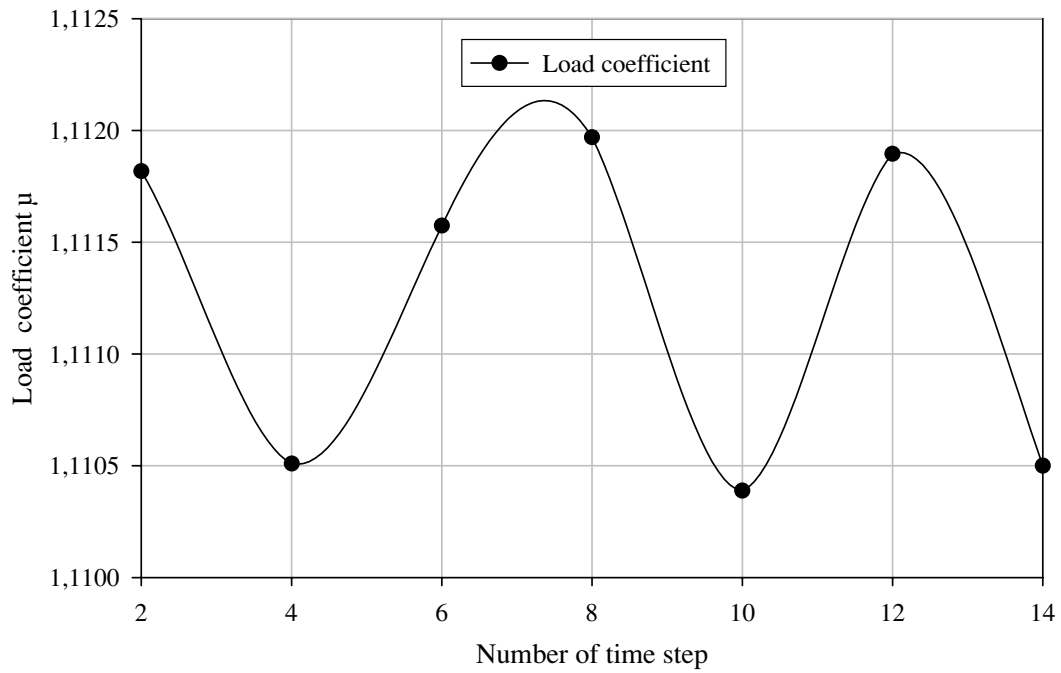
Figure 6.35: Instantaneous load coefficients for $\Delta p = 2500\,Pa$, curved lines geometry, compressible fluid.
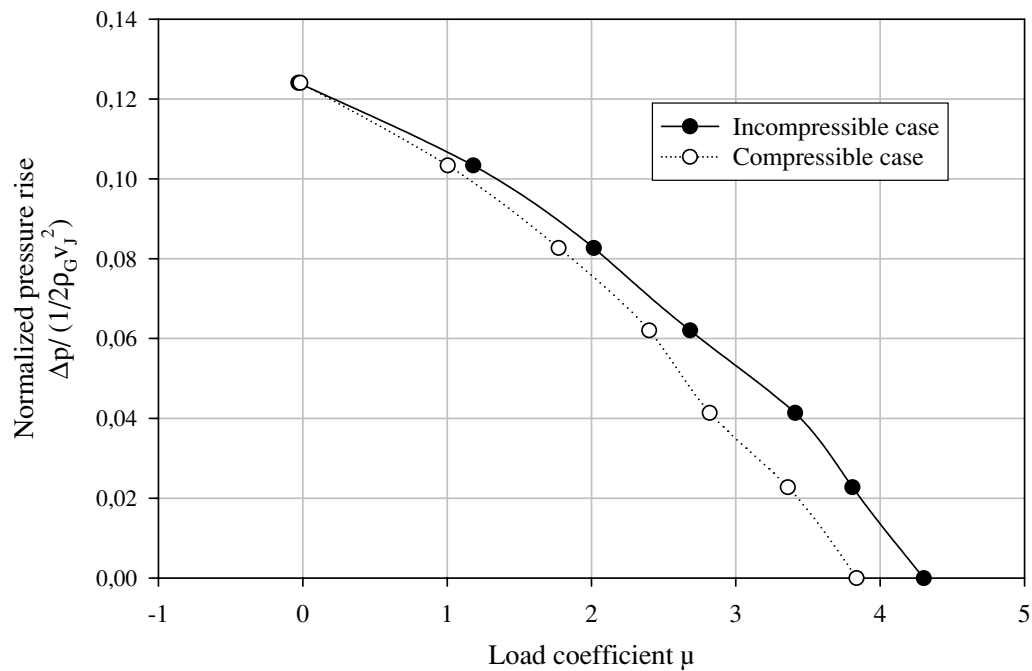
Figure 6.36: Comparison of load coefficients of the incompressible and compressible calculations for the curved lines geometry.

Comparing the load coefficients with those of the incompressible case, the load coefficients of the compressible calculations are lower than those of the incompressible calculations as shown in figure 6.36.

Taking the design case as representative, table 6.12 is obtained with the interpolated values of density and velocity at the entrance of the mixing duct both for the jet and for the secondary flow.

Table 6.12: Comparison between the values of the density and the velocity in the incompressible and compressible case, curved line geometry.

Incompressible	Compressible
$\rho_J = 1,21^{kg}/_{m^3}$	$\rho_J = 1,22^{kg}/_{m^3}$
$v_J = 181,6121^{m}/_{s}$	$v_J = 181,6121^{m}/_{s}$
$\rho_G = 1,21^{kg}/_{m^3}$	$\rho_G = 1,1838^{kg}/_{m^3}$
$v_G = 38,02^{m}/_{s}$	$v_G = 32,51^{m}/_{s}$

The mass flows of table 6.13 were calculated with equation 6.5.

Table 6.13: Comparison between the values of mass flow in the incompressible and compressible case, curved line geometry.

Incompressible	Compressible
$\dot{m}_J = 2,42^{kg}/_{s}$	$\dot{m}_J = 2,44^{kg}/_{s}$
$\dot{m}_G = 8,92^{kg}/_{s}$	$\dot{m}_G = 7,46^{kg}/_{s}$

These values show again that the amount of gases from the secondary flow taken into the injector is lower for the compressible case. Then, the load coefficient will be also lower for the same conditions.

The pressure distribution along the injector axis also appears to be different from the incompressible case. The pressure distribution of the design case is shown in figure 6.37. The same reasons mentioned for the straight lines can be utilized here to explain the differences between both distributions.

Doing an interpolation of the velocity values at the end of the mixing duct and at the end of the diffuser, the profiles are as expected. The velocities are higher for the incompressible case.

Figure 6.37: Comparison of the pressure distribution along the injector axis for compressible and incompressible fluid for the curved lines geometry.

Figure 6.38 displays the velocities at the end of the mixing duct and at the end of the diffuser both for compressible and incompressible fluid. Comparing figure 6.38 to figure 6.31, the conclusion is the same as in the incompressible case. The velocities are higher for the curved line geometry than for the straight lines geometry.

Interpolation of the v_x velocities at the end of the mixing duct.

Interpolation of the v_x velocities at the end of the diffuser.

Figure 6.38: Comparison between the v_x velocities both for incompressible and compressible fluid in the curved lines geometry.

Figure 6.39 is obtained by calculating the efficiencies in the tested pressure range.
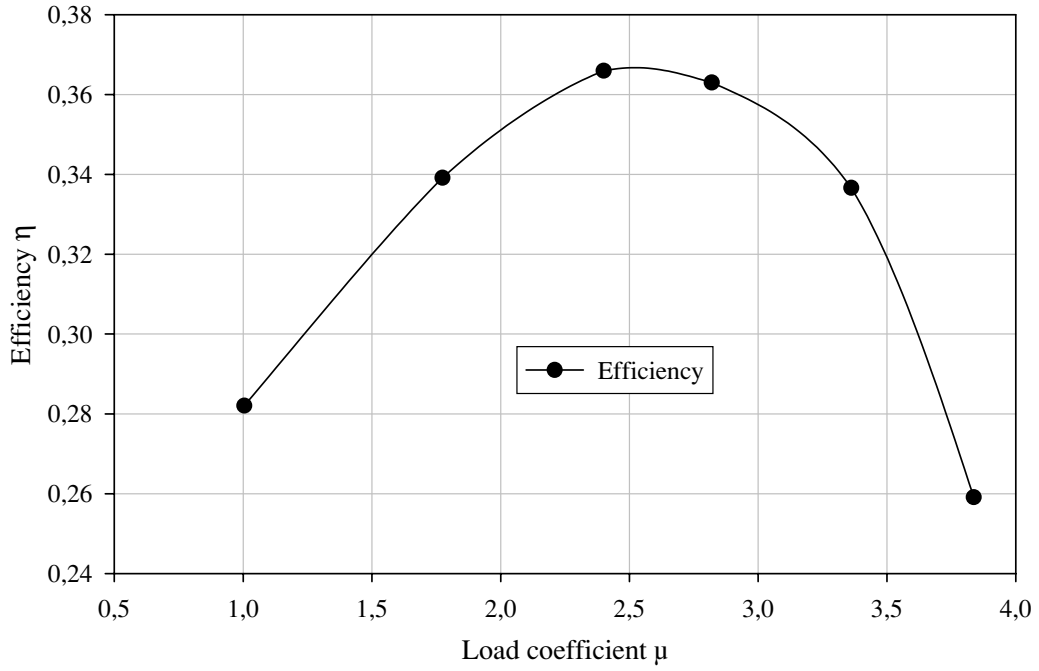
Figure 6.39: Efficiencies for the curved lines geometry compressible case.

The maximum efficiency lies in the region between $\mu = 2$ and $\mu = 3$, where the eddies appear. The explanation is the same as in the straight lines geometry.

The efficiency in the design case, $\Delta p = 1000\,Pa$, is equal to $\eta = 35,88\,\%$, smaller than the efficiency achieved with incompressible fluid $\eta = 42,3\,\%$. For the design case of the curved line geometry the efficiency η_{comp} is $15,2\,\%$ lower than η_{incomp}.

6.2.2 Comparison of Straight Lines Geometry and Curve Lines Geometry

If the results of the straight lines geometry are fitted together with the curved lines geometry, the load coefficients and the efficiencies can be clearly compared.
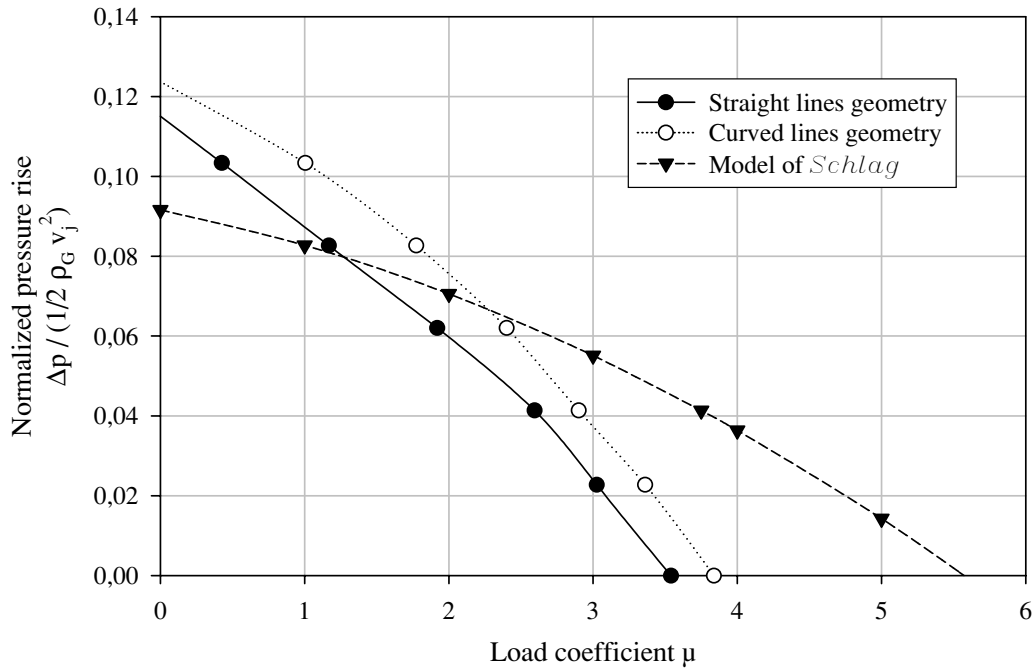
Figure 6.40: Comparison of the straight lines geometry, the curved lines geometry and the results proposed by the model of *Schlag*.

Comparing the curves in figure 6.40, it is found that for low load coefficients the pressure rise that the injector can overcome is larger than the one expected by the model of *Schlag*. For higher load coefficients this difference decreases until the model of *Schlag* has larger load coefficients for the same pressure rises. This phenomenon occurs in the straight lines geometry at lower load coefficients than in the curved lines geometry because the load coefficients are smaller in general and the mixing process is worse for constant width mixing ducts.

The pressure rises at low load coefficients are higher than the ones obtained by the model of *Schlag*. This can be attributed to the average in the discharge when the jet is swinging. *Schlag* did not consider this circumstance when building up his model. The swinging jet gives rise to some maximums that increase the suctioned mass gas flow for the same pressure at the outlet.

For larger load coefficients, between $1,5 \leq \mu \leq 3$, there is a maximum in the efficiencies because of the improvement of the mixing process with the appearance of eddies. Despite this improvement the load coefficients within this range are lower for the straight lines case than for the model of *Schlag*.

Furthermore, for high load coefficients, the losses in the diffuser increase. These losses decrease the efficiency and make the curves move towards lower load coefficients. So that, if lower values for the efficiency had been applied in the diffuser for these cases, the characteristics of the model of *Schlag* would have been nearer to the ones obtained by the CFD calculations.

Figure 6.41 depicts the different charactersitics of the model of *Schlag* changing the efficiency of the diffuser. The high influence of the diffuser efficiency for high load coefficient can be seen clearly.

71
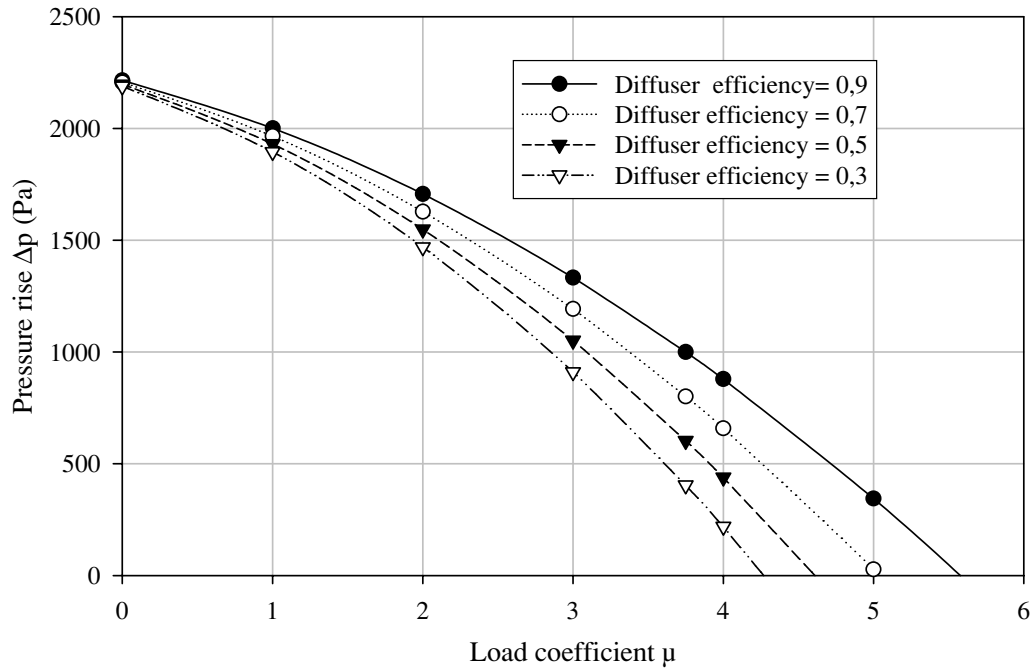
Figure 6.41: Characteristics of the model of *Schlag* for different diffuser efficiencies.

Making a comparison of the efficiencies of the straight lines geometry and the curved lines geometry, the injector with the variable width mixing duct has got a better performance for the whole range of pressures rises. The percentage of improvement is shown in table 6.14.

Table 6.14: Improvement in the efficiency of the curved line injector.

Pressure rise	Improvement in %
$\Delta p = 0\,Pa$	27,5
$\Delta p = 550\,Pa$	30,4
$\Delta p = 1000\,Pa$	19,6
$\Delta p = 1500\,Pa$	28,2
$\Delta p = 2000\,Pa$	34,7
$\Delta p = 2500\,Pa$	36,1

The efficiencies for both geometries can be shown together in one graph. Figure 6.42 shows the efficiency versus pressure rises, figure 6.43 the efficiency versus the load coefficients.

In figure 6.42, the maximum efficency is reached at different pressure rises. For the straight lines geometry it is reached at the design point and for the circled lines geometry it is reached at $\Delta p = 1500\,Pa$. This difference in pressure rise has it explanation when looking at figure 6.43. Both maximums occur approximately for the same load coefficient. As it was previously explained, these maximums happen for a load coefficient in the range $2 \le \mu \le 3$ where the vortices are formed the first time and improve the mixing process.
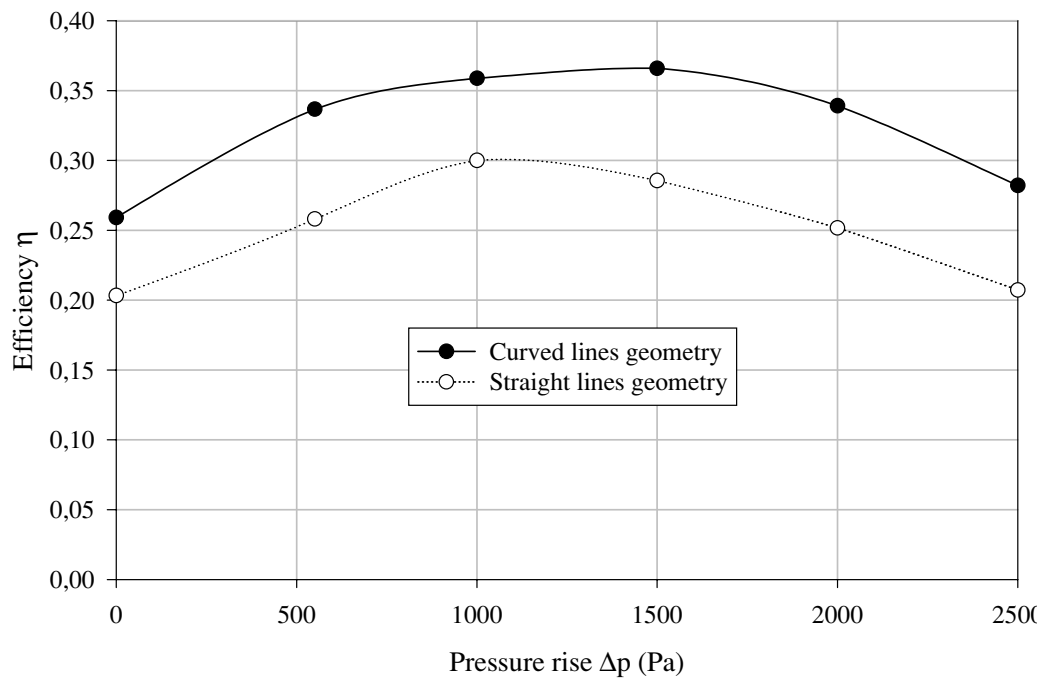
Figure 6.42: Efficiency versus pressure rise.
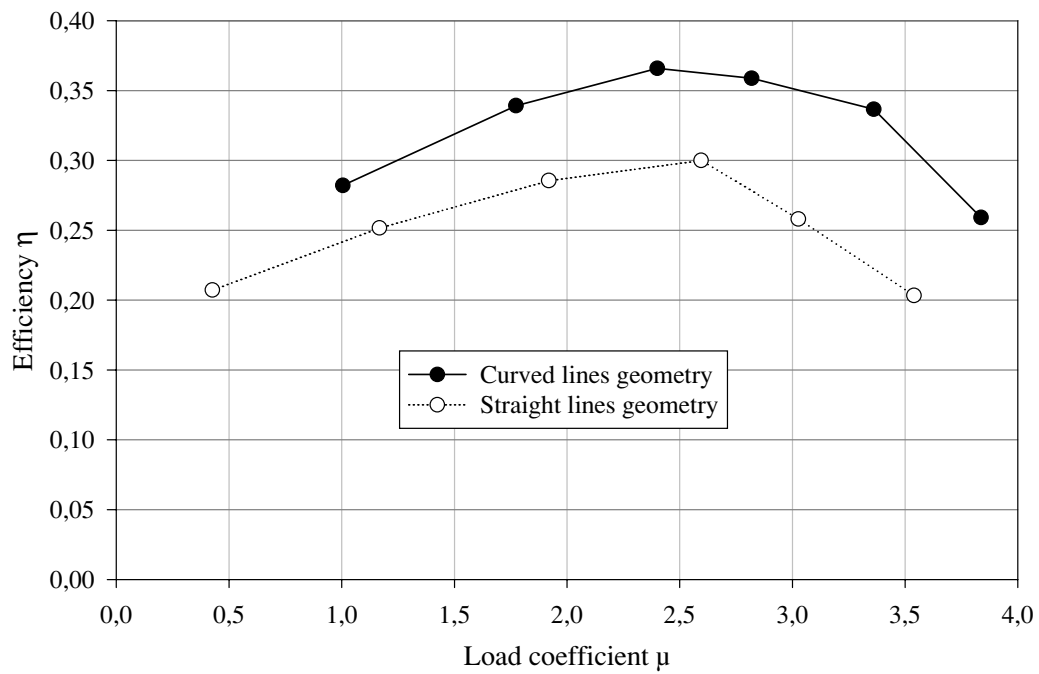
Figure 6.43: Efficiency versus load coefficient.

73
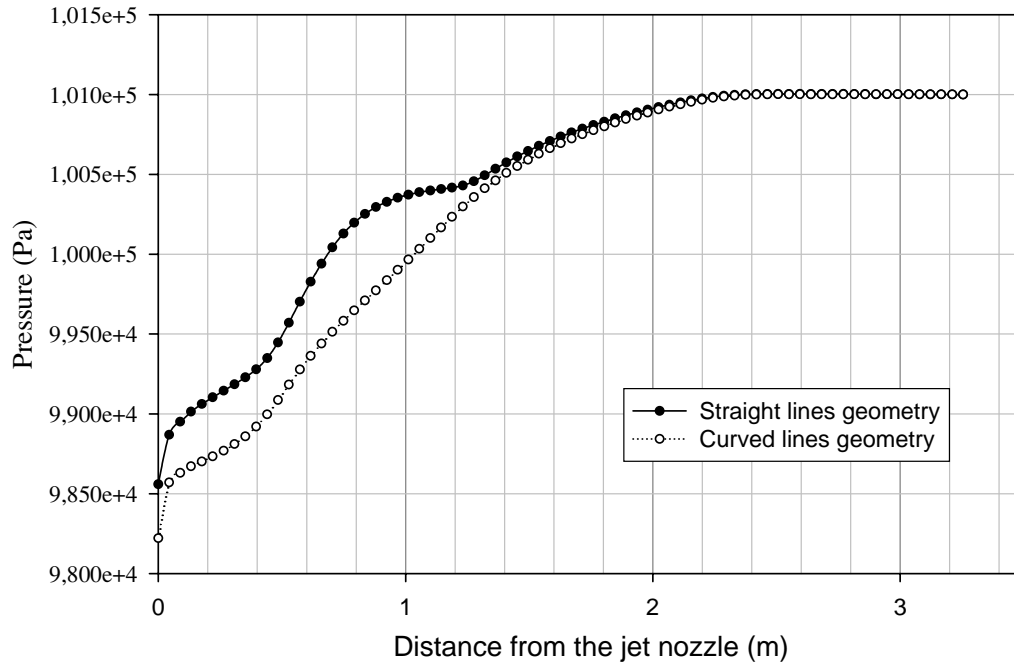
Figure 6.44: Comparison of the pressure distributions for the straight lines geometry and curved lines geometry, compressible fluid.

The pressure distribution along the injector axis for both geometries is shown in figure 6.44.

The pressure is lower for the curved lines geometry until the end of the diffuser. However, the velocity of the mixture is higher in the curved lines geometry, as can be seen in figure 6.31 and 6.38. For this reason, the pressure at the end of the injector can be higher for the curved line geometry when using the same jet properties and discharge velocity.

Chapter 7

What Else Can Be Done

Once the results of the compressible case have been obtained, the geometry can be recalculated using the mean value of the density obtained by the compressible calculations. With $\rho_G = 1,1861^{kg}/_{m^3}$ only one ratio $\frac{W_M}{W_J} = 21,5$ is obtained to overcome the design pressure rise. With this ratio, the calculation process can be started again.

Also for both geometries and same operating conditions, calculations for an axisymmetric model can be done. In the axisymmetric geometry the area at the entrance of the mixing duct and the area of the jet nozzle are proportional to the squared diameter, D^2. The obtained ratios are $\frac{D_M}{D_J} = 3,352$ and $\frac{D_M}{D_J} = 5,795$, as shown in figure 7.1. These ratios are smaller than in the plane case and also the characteristic curves of the injector are different, as shown in figure 7.2. The part load conditions of the injector will become more important.

In both cases, it can be tried to model a real constant pressure injector. In a real constant pressure injector the different heights or diameters must be calculated along the injector axis by the application of thermodynamic equations.

Also a real three dimensional injector can be modelled. In this injector the jet is not uniform at the end of the jet nozzle. The flow has a momentum of momentum which produces two additional vortices. This phenomenon has influence on the mixing process.

The influence of the jet properties on the behaviour of the injector can also be tested, for instance, how the velocity of the jet affects the flow when it is increased to values of $Ma \geq 1$.

Furthermore, it has been mentioned in the introduction that the injector can work with different nature fluids and even with fluidized particles. The path of this particles in the injector and their influence on the behaviour of the injector could be investigated.
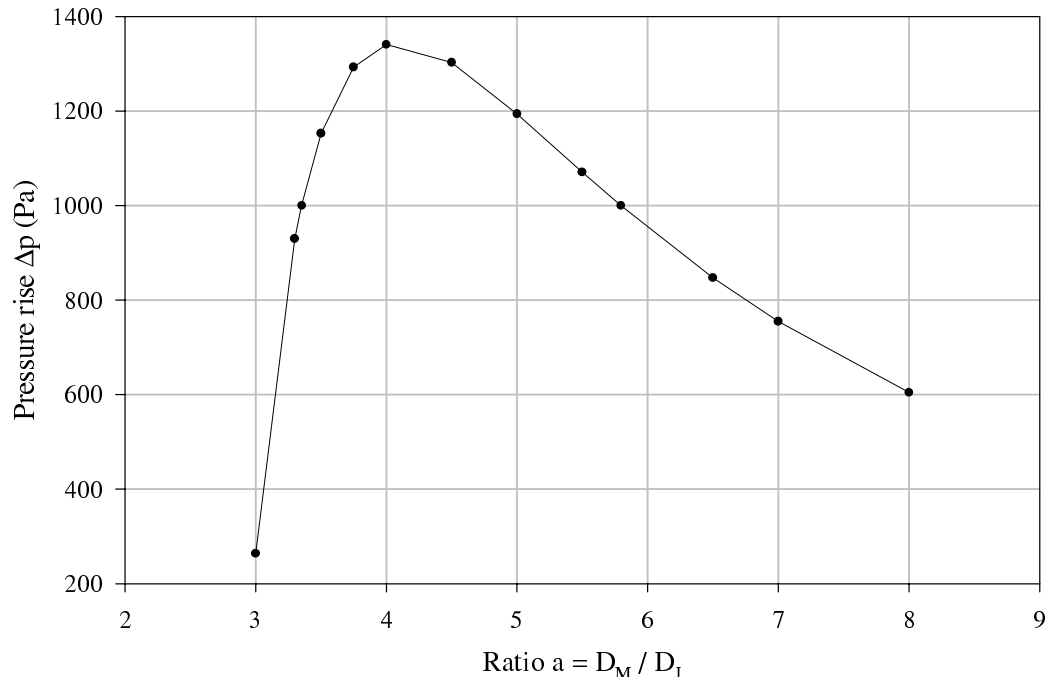
Figure 7.1: Net pressure rise for different values of the parameter a in the axisymmetric case.
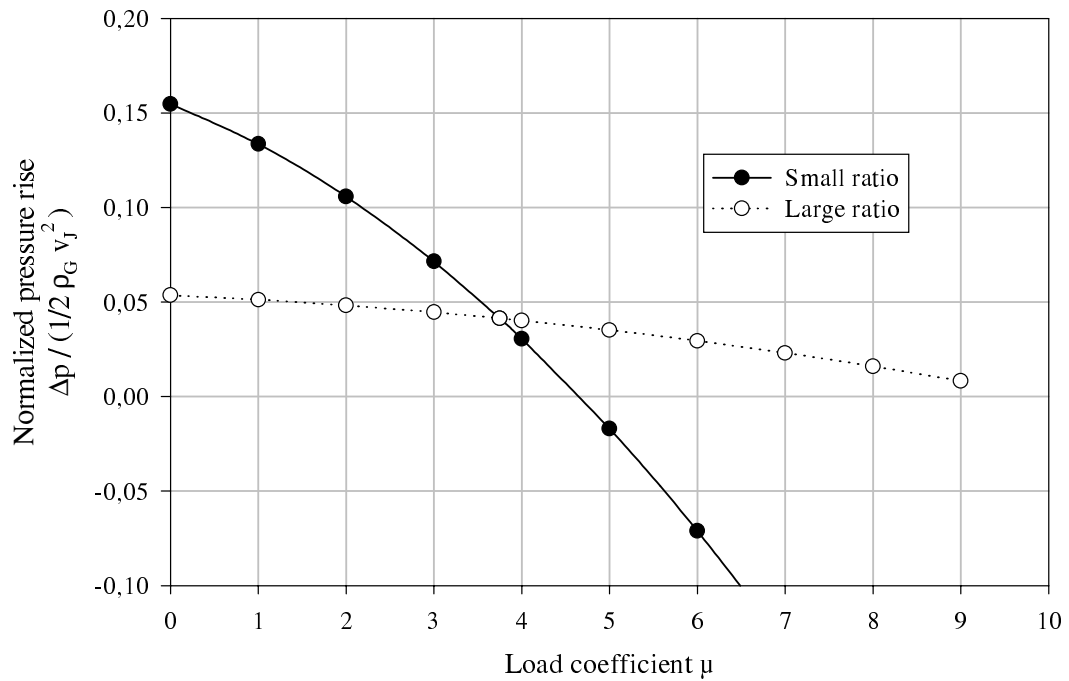
Figure 7.2: Characteristic curves by the model of *Schlag* for both injector geometries in the axisymmetric case.

Bibliography

[1] *CFX International*: CFX-4.2. AEA Technology, Oxfordshire, December 1997.

[2] *Schlag H.P.*: Experimentelle und theoretische Untersuchen zur Berechnung der Kennlinien von gastriebenen Einphaseninjektoren und Gutaufgabeinjektoren. Fortschritt-Beichte VDI, Stuttgart, 1993.

[3] *Rajaratnam N.*: Turbulent Jets. Elsevier Scientific Publishing Company, Amsterdam-Oxford-New York, 1976.

[4] *Traupel W.*: VDI-Handbuch Energietechnik, Teil 2, Wärmetechnische Arbeitsmappe.

[5] *Libby P.A.*: Introduction to Turbulence.Taylor and Francis, Washington, D.C.,1996.

[6] *Fratzscher, Brodjanskij, Michalek*: Exergie, Theorie und Anwendun. VEB Deutscher Verlag für Grundtoff- industrie. Distributed by Springer-Verlag. Wien - New York. Leipzig, 1986.

[7] *Evett J.B. Cheng Liu*: 2500 Solved Problems in Fluid Mechanics and Hydraulics. McGraw-Hill Book Company, 1989.

[8] *Curtet R.* : Confined Jets and Recirculation Phenomena with Cold Air. Combustion Flame 2, 1958.

[9] *Hembold H.B., Luessen G., Heinrich A.M.*: An Experimental Comparison of Constant-Pressure and Constant-Diameter Jet Pumps. University of Wichita, Wichita, July 1954.

[10] VDI-Wärmeatlas: Berechnungs blä für den Wärme übergang, 8. Auflage. VDI-Verlag, Düsseldorf, 1997.

[11] *Brauer H.*: Grundlagen er Einphasen-und Mehrphasenströmungen, 1971.

[12] *Schlichting H., Gestern K.*: Grenzschicht-Theorie. Springer-Verlag, Berlin, Heidelberg 1997.

[13] *Young C.B.*: Boundary Layers. IAATA Educational.

[14] *Schetz J.A., Fush A.E.*: Handbook of Fluid Dynamics and Fluid Machinery, Volume One: Fundamentals of Fluid Dynamics. Wiley-Interscience.

[15] *Reneau L.R., Johnston J.P., Kline S.J.*: Perfomance and Design of Straight, Two-Dimensional Diffusers. Journal of Basic Engineering, March 1967.

[16] *Kelnhofer W.J., Derick C.T.*: Tailpipe Effects on Gas Turbine Diffuser Perfomance with Fully Developed Inlet Conditions. Journal of Engineering Power, January 1971.

List of Figures

List of Tables